To the Graduate Council:

I am submitting herewith a thesis written by Gregory G. Rice entitled "Small-Angle X-ray Scattering Characteristics of Voids in Kevlar® 49 and Graphite Fibers." I have examined the final copy of this thesis for form and content and recommend that it be accepted in partial fulfillment of the requirements for the degree of Master of Science, with a major in Polymer Engineering.

John F. Fellers

John F. Fellers, Major Professor

We have read this thesis
and recommend its acceptance:

Walter F. Jones

Jae-Hyung Lee

Accepted for the Council:

Lou Minkel

Vice Provost
and Dean of The Graduate School

SMALL-ANGLE X-RAY SCATTERING CHARACTERIZATION OF VOIDS IN KEVLAR® 49 AND GRAPHITE FIBERS

A Thesis

Presented for the

Master of Science

Degree

The University of Tennessee, Knoxville

Gregory G. Rice

December 1984

DEDICATION

This thesis is dedicated to my wife, Judy, and to my parents. Without their support and encouragement, this accomplishment would not have been realized.

ACKNOWLEDGMENTS

The author wishes to express his deepest appreciation to Dr. J. F. Fellers, his advisor during the course of this work, and to Dr. J. S. Lin for his help concerning the operation of the small-angle x-ray scattering equipment at the National Center for Small-Angle Scattering Research.

The author also wishes to thank the Material Science and Engineering faculty members, office staff, and his fellow students for their instruction and assistance.

The author appreciates the financial support given him by the Lawrence Livermore Laboratory.

ABSTRACT

The characterization of voids in fiber reinforcements commonly used in high performance composites was studied using small x-ray scattering (SAXS) at the National Center for Small Angle Scattering Research. The void dimensions and void volume fraction was determined from the SAXS data for Kevlar® 49, for a pitch-based graphite fiber, and for two PAN-based graphite fibers. The accessibility of the voids in the fibers to a diffusing liquid was studied using SAXS with glycerin as the diffusing liquid.

Scanning electron microscope (SEM) micrographs were used to determine the ability of plasma etching to remove the skin from the core of Kevlar® 49 fibers. SAXS analysis was performed on the etched fibers to determine the effect of etching on the scattering pattern at the long and short geometry of the SAXS equipment. This led to the conclusion that the smallest voids are located in the core and the largest voids in the skin of the fiber.

Mechanical properties of epoxy resins cured with varying amine concentrations and Kevlar® 49 reinforced composites were determined using an Instron Mechanical Tester. The SAXS patterns of the epoxies and composites were obtained before and after fracture to determine if there was an increase in the scattering pattern due to the creation of voids in the material during the failure process. SEM micrographs of the fracture surface of the composites show fibers pulled out

from the epoxy matrix, fiber splits along with skin damage and fiber skin-core separation.

TABLE OF CONTENTS

CHAPTER PAGE

LIST OF FIGURES

FIGURE PAGE

FIGURE PAGE

FIGURE PAGE

INTRODUCTION

The use of high performance composite materials is growing rapidly due to their weight savings advantage over the structural metals. Two of the most popular types of reinforcements used in high performance composites are Kevlar® 49 and graphite fibers. These fibers are known to contain a microvoid pore system, which is detrimental to the strength of the fibers. More knowledge of the relation of macroscopic material strength to the microscopic material structure is needed.

The purpose of this research is to characterize the microvoid system in these fibers using the high resolution small angle x-ray scattering (SAXS) facilities at the National Center for Small Angle Scattering Research. The size, shape, and volume fraction of these voids are to be determined from the SAXS data. In addition, a model of the void structure in relation to the skin-core morphology of the Kevlar® 49 fiber is presented.

If the microvoids in the fibers were capable of being filled, an increase in the strength of the fiber as well as superior adhesion between the fiber and the matrix in a composite due to penetration and healing would be expected. This is studied using SAXS and SEM micrographs of the fractured composite surface.

CHAPTER 1

SMALL-ANGLE X-RAY SCATTERING

1.1 Introduction

When x-rays of a given wavelength impinge on a material, the electrons in the material become secondary scatterers of x-rays. Thus, the atoms are said to "scatter" the incident x-rays. Two types of scattering occur: 1) coherent scattering, which occurs without change of wavelength and without loss of phase relationship between the incident and scattered rays, and 2) incoherent scattering, which is also called Compton scattering after A. H. Compton, who first explained the shift in wavelength as resulting from the encounter of an x-ray photon with a loosely bound or free electron (1). At small angles, incoherent scattering is very weak and can be neglected (2, 3).

Diffraction is produced by the interference of x-ray waves scattered by the electrons that surround the various atomic centers. In general, x-ray interference effects result from variations in electron density from one point to another in the material. If the atoms in the material are regularly arranged according to a space lattice, then the scattering angle 2θ is related to the x-ray wavelength λ and the interplanar spacing d by the Bragg equation (4)

$$n\lambda = 2d \sin\theta \qquad (1\text{-}1)$$

where n is an integer referring to the order of reflection from the given planes. This equation suggests the existence of an inverse relationship between the interplanar spacing d and sin θ. If λ and d are of the same order of size, diffraction effects appear over a wide range of angles (wide angle diffraction).

Small angle x-ray scattering (SAXS) analysis is also a technique for studying structural features of a material. It was introduced when it became desirable to detect large lattice spacings of the order of tens or hundreds of interatomic distances (2). When monochromatic x-rays are passed through very small particles, normally of the order of 10 to 2000Å, or through a body containing zones of non-uniform electron density of about this size, a diffraction pattern generally results within a very small range of angles around the incident beam since any scattering process is characterized by a reciprocity law, which gives an inverse relationship between particle size and scattering angle. With CuKα radiation, wavelength 1.542Å, x-ray scattering and interference effects typically occur in the angular range below 5°.

From the small-angle scattering viewpoint, electron concentrations at the atomic sites might be thought of as a continuous distribution of electrons within the unit cells. Only the fluctuations in electron density over much larger distances determine the nature of the small-angle scattering. This scattering differs in principle from wide-angle diffraction because it has no dependence on the inhomogeneities of atomic dimensions. Therefore, pure phases in general,

and other homogeneous substances only weakly scatter x-rays at very small angles (5).

The two kinds of inhomogeneity that are most likely to be responsible for small-angle x-ray scattering from solid polymers are 1) alternation of crystalline and amorphous regions, which in general will possess different electronic densities and 2) the presence of microvoids dispersed throughout the solid polymer matrix. The intensity of small-angle scattering increases with the degree of contrast between the electron densities of the two or more kinds of regions that produce the heterogeneity. Thus it is relatively large for a dispersion of micropores in a solid medium, but relatively small for a heterogeneous system of crystalline and amorphous regions that differ but slightly in density (5).

Small-angle x-ray scattering from an inhomogeneous system may consist of either diffuse or discrete effects. Guinier (8-10) first showed that a single particle of colloidal dimensions can produce a characteristic diffuse small-angle scattering pattern and that many identical particles at sufficiently large and irregular distances from each other will produce a total scattering that is simply the sum of the scattering of the individual particles. This is the concept of a dilute system, which produces pure particulate scattering. If discrete interferences appear in the small-angle scattering patterns of oriented polymers, they are usually observed in only one direction, most commonly on the meridian. Meridional

reflections denote some degree of large scale periodic character in the structure parallel to the fiber axis.

Small-angle scattering is produced by substances containing small zones of non-uniform density which may be linear, planar, or particulate. This phenomenon has a remarkably wide application to the measurement of small particles. Since scattering is dependent upon the geometrical structure of the minute inhomogeneous zones, it is possible to establish the size, shape, and state of aggregation of the small particles by analysis of the scattering pattern. The angular limit within which the scattering occurs is inversely proportional to the size of the inhomogeneities in the electron-density distribution within the specimen. Thus the diffuse scattering from a loose aggregation of oriented particles will have its smallest extension in the direction of the larger dimension, which is to say that the shape of the diffuse scattering depicts the particle shape in reverse.

X-ray small-angle scattering has the very important advantage, in comparison with other physical methods, in that the sample may be a gas, liquid, solid, crystalline, amorphous, or a mixture of these, and may take the form of minute inclusions or voids. It also requires no special preparation of a polymer sample. Small-angle x-ray scattering is a useful non-destructive technique for testing fiber composites. It is a direct observation technique and is particularly useful for studying the fiber alignment and also for locating cracks and studying their propagation.

1.2 Small-Angle X-Ray Experimental Requirements

The experimental requirements for useful small-angle scattering experiments are very exacting in comparison with the requirements for wide-angle measurements. A well-designed and engineered apparatus capable of producing a very sharp collimation of the incident x-rays is needed for measuring the scattered radiation at angles that are very close to the undeviated beam. The alignment of the components is critical, and long periods of time are required for recording the weakly scattered x-rays. It is usually necessary to evacuate the apparatus in order to eliminate air scattered x-rays, which at small angles are of sufficient intensity to distort or mask features of the small-angle scattering by the specimen. For the analysis of diffuse small-angle scattering it is mandatory that wavelengths other than the desired characteristic radiation be removed by means of a crystal monochromator.

For the preparation of an undistorted small-angle scattering pattern it is necessary to collimate the beam with a pair of fine pinholes when the nature of the internal inhomogeneity and texture of the specimen are not known in advance. This method has the disadvantage of requiring very long exposures to compensate for the weakness of the beam that is incident on the specimen. In most experimental work, a slit-defined primary beam is used rather than a pinhole beam. This is known as the Kratky method. When pinholes are replaced by the slit collimators the intensity of scattering is greatly

increased and the exposure times can be correspondingly reduced. However, the substitution of slits causes a substantial distortion of the theoretical distribution of scattered intensity, which may be dealt with in either of two ways: 1) by mathematical corrections or 2) by using slits of sufficient length to permit the application of the special treatment of the theory of scattering by infinitely long slits. Due to certain approximations involved with the unsmearing formulas, the second method is generally preferred to interpret the slit-distorted intensities. However, it still has one important disadvantage in that the theory does not yield the complete scattering curves for particles of various specific shapes and for different size distributions. Thus when information about particle shape or polydispersity is sought, it is still necessary to resort to intensities obtained with pinhole collimators or by correction of data obtained with slit collimators in order to make the necessary comparisons of the experimental and theoretical scattering curves. Slit collimation may be applied to an isotropic specimen, but for highly oriented materials it gives useful information only when the slits are either precisely parallel or perpendicular to the orientation axis of the specimen.

1.3 Some Considerations in the Interpretation of Diffuse Small-Angle Scattering

A diffuse small-angle scattering pattern cannot by itself yield an absolute interpretation of the structure of the specimen. However, specimens that yield identical scattering curves may be

designated scattering-equivalent systems (11). The following types of ambiguity must be considered when interpretating diffuse small-angle scattering patterns:

1. Due to the Babinet principle of reciprocity in optics, it is not possible to distinguish the scattering by a system of particles in space from the scattering by a complementary system of micropores in a solid medium. Usually, this choice can be made on the basis of independent evidence concerning the type of system involved.
2. The scattering effects due to particle shape and those due from polydispersity are undifferentiable without some degree of uncertainty. In other words, scattering equivalence may result from a special particle shape and a certain distribution of particle sizes.
3. Sometimes diffraction due to normal Bragg reflection and characteristic long repeat distances which can occur at very small angles accompanies the diffuse scattering (6). In general, solid polymeric systems exhibit this type of behavior. It is frequently difficult to determine what portion of the scattering curve is due to diffuse scattering and what portion is due to discrete interferences. Therefore, in interpreting diffuse scattering at small angles from dense systems, the interparticle interference effects cannot be neglected.

1.4 General Theory of Diffraction Principles

Diffuse small-angle scattering is usually associated with scattering from particles or other entities that exhibits interference effects due to a lack of periodicity. Because the electrons occupy an appreciable volume about the atomic nucleus, the x-rays scattered coherently by the various electrons within one atom are slightly out of phase with each other. The phase is $2\pi/\lambda$ times the difference between the optical path and some arbitrary reference point.

Figure 1-1 shows the scattering by two point centers in a single particle. s_o represents the unit vector defining the direction of the incident radiation, s represents the unit vector defining the direction of the scattered wave, the scattering angle between the incident and scattered wave is designated as 2θ, and o represents an arbitrary origin serving to describe the direction of the incident radiation. The scattered waves are coherent, which means that the amplitudes of waves are added in directions for which the phases are the same. The degree to which the waves are out of phase depends on the size of the scattering angle 2θ. The shape of the coherent-scattering intensity versus 2θ of angle is called the scattering function.

The classical formula in the theory of x-ray diffraction gives the amplitude of radiation scattered from the atom at point M in Figure 1-1 in the direction defined by the unit vector s as

$$A_m = A_e f_m \exp\left[-i \frac{2\pi}{\lambda} (s-s_o) \cdot r_m\right] \qquad (1\text{-}2)$$

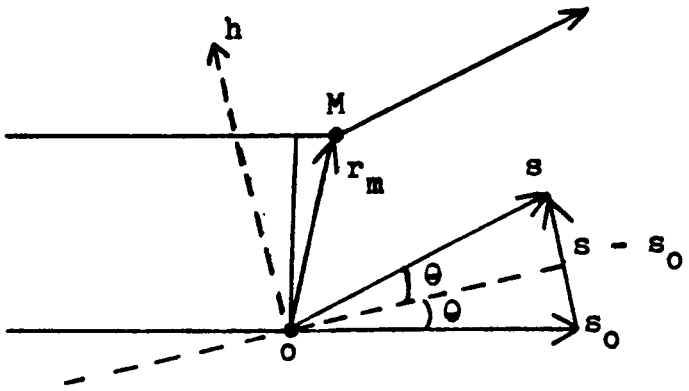

Figure 1-1. Scattering by Two Point Centers.

where A_e designates the amplitude scattered by one free electron for the same conditions, f_m is the atomic scattering factor, and r_m is the vector from the origin to point M. Let h be defined as the vector $(2\pi/\lambda)(s-s_o)$. It is seen from Figure 1-1 that $(s-s_o)$ lies symmetrically with respect to the incident and scattered beam, and that its magnitude is $2\sin\theta$. Therefore the magnitude of h is $h = (4\pi \sin\theta)/\lambda$.

The total amplitude scattered from the entire particle is

$$A(h) = A_e(h)\sum_m f_m \exp[-ih\cdot r_m] \qquad (1\text{-}3)$$

The intensity is given by the absolute square of the amplitude and complex conjugate A*

$$I(h) = A(h)A^*(h) = A_e^2(h)\sum_{mn}\sum f_m f_n \exp[-ih\cdot(r_m - r_n)] \qquad (1\text{-}4)$$

Expanding Eq. (1-4) gives

$$I(h) = I_e\sum_m \sum_n f_m f_n \cos[h\cdot(r_m - r_n)] \qquad (1\text{-}5)$$

where $I_e = A_e^2$.

By summing up all secondary waves, the resulting amplitude can be obtained. However, due to the large number of electrons and due to the inability to determine the exact location of the electron, the concept of electron density is introduced. The electron density of a diffracting body at a point defined by the vector r, $\rho(r)$, may be defined as the number of electrons per unit volume. A volume element dV at position r will contain $\rho(r)dV$ electrons.

In the theory of x-ray diffraction, the diffraction pattern of a sample can be represented in terms of a reciprocal, or Fourier,

space. The amplitude of radiation scattered by a particle, A(h), is the transform of $\rho(r)$ at the point defined by the vector h in reciprocal space and is given by the equation

$$A(h) = \int \rho(r) \exp[-ih \cdot r] dV \tag{1-6}$$

The intensity can now be written as

$$I(h) = \int_o^\infty \int_o^\infty \rho(r_1)\rho(r_2)\exp[-ih \cdot (r_1 - r_2)] dV_1 dV_2 \tag{1-7}$$

Eq. (1-7) can be simplified by use of the mathematical operation of convolution of the electron densities, $\overset{2}{\rho}$, defined by the equation

$$\overset{2}{\rho}(r) = \int_o^\infty \rho(r_1)\rho(r_2) dV_1 \tag{1-8}$$

with $r = (r_1 - r_2)$ = constant. This function takes into account the electron density of every electron pair with relative distance r and averages their product over the volume of the system. Now the intensity equation can be rewritten as

$$I(h) = \int \overset{2}{\rho}(r) \exp[-ih \cdot r] dV \tag{1-9}$$

This Fourier transform indicates that the intensity distribution in reciprocal space is uniquely determined by the structure of the object, as expressed by $\overset{2}{\rho}(r)$.

Debye (12) showed that the intensity of an x-ray scattered by a spherically symmetrical system of atoms as a function of h is given by

$$I(h) = \sum_{mn}\sum f_m f_n \frac{\sin hr}{hr} \qquad (1\text{-}10)$$

Now Eq. (1-9) can be expressed as

$$I(h) = \int 4\pi r^2 \rho(r) \frac{\sin hr}{hr}\, dr \qquad (1\text{-}11)$$

If there is no long range order, no correlation exists between two points separated widely enough. Then at large r the respective electron densities should become independent and then be replaced by the mean electron density, $\bar{\rho}$. This makes Eq. (1-8) approach a constant value $\bar{\rho}^2 V$. Since a constant value for the electron density throughout the total volume cannot make any contribution to the diffraction pattern in the experimental accessible angles, it is possible to disregard it and to use the electron density fluctuation, $\rho - \bar{\rho}$, instead.

Of particular importance in the study of dense two-phase systems is the concept of the correlation function (13,14) or characteristic function (15,16) defined by

$$\gamma(r) = \frac{\overline{(\Delta\rho)_1 (\Delta\rho)_2}}{(\Delta\rho)^2} \qquad (1\text{-}12)$$

where $(\Delta\rho)_1$ and $(\Delta\rho)_2$ are the local deviations of the electron density from the average value $\bar{\rho}$ at points 1 and 2 separated by a distance r. The correlation function has the physical meaning of an average distribution of scattering matter in the vicinity of an origin which assumes all locations within the system with equal probability (5).

It is therefore a model with continuously varying electron density that is scattering equivalent to the particular inhomogeneous system under consideration (17).

Now using the electron density fluctuation, $\rho - \bar{\rho}$, instead of the density ρ, Eq. (1-8) can be redefined as

$$(\rho - \bar{\rho})^2 = \overline{\rho^2} - V\bar{\rho}^2 = V \cdot \gamma(r) \tag{1-13}$$

Eq. (1-11) now takes the form

$$I(h) = V\int_0^\infty 4\pi r^2 \gamma(r) \frac{\sin hr}{hr} dr \tag{1-14}$$

The correlation function is related to the scattering curve by the inverse Fourier transform

$$V\gamma(r) = \frac{1}{2\pi^2} \int_0^\infty h^2 I(h) dh \frac{\sin hr}{hr} \tag{1-15}$$

For the simple case where $r = 0$ Eq. (1-15) takes the form

$$V\gamma(0) = \frac{1}{2\pi^2} \int_0^\infty h^2 I(h) dh = V(\rho - \bar{\rho})^2 \tag{1-16}$$

The problem of small angle analysis consists of deducing size, shape, mass, and possibly even the electron density distribution from the scattering curve. For homodisperse, dilute particulate systems, the scattered intensities of the individual particles simply add up. For anisotropic particles, the scattering for every orientation has to be calculated and the results averaged. A model particle must be found whose scattering curve agrees within experimental error

with the experimental curve. It is possible to compute the expected scattering curve for any particle shape by using the distance distribution function of the electrons p(r), which is obtained by geometrical considerations (3). The scattering curve I is obtained from p(r) by Fourier inversion

$$I(h) = 4\pi \int_0^\infty p(r) \frac{\sin hr}{hr} dr \qquad (1\text{-}17)$$

Much work has been done in determining the scattering curves for numerous three-axial bodies, such as ellipsoids, parallelpipeds, ellyptic cylinders, hollow spheres, etc.

Instead of comparing experimental and theoretical scattering curves, it is possible to compare theoretical and experimental p(r) functions using the equation obtained by Fourier inversion of the scattering curve

$$p(r) = \frac{1}{2\pi^2} \int_0^\infty I(h) hr \sin hr \, dh \qquad (1\text{-}18)$$

This has the advantage of allowing the calculation of the r value at which p(r) drops to zero indicating the largest particle dimension.

1.4.1 Law of Guinier. A parameter obtained directly from the scattering curve without the problem of finding a model equivalent in scattering is the radius of gyration, R, which is an analog to the radius of inertia in mechanics. The electronic radius of gyration is the root mean square of the distances of all the

electrons from the electronic center of gravity of the representative particle (2)

$$R = \left(\frac{\sum_k f_k r_k^2}{\sum_k f_k} \right)^{\frac{1}{2}} \tag{1-19}$$

where f_k is the scattering factor of the kth electron, which is a distance r_k from the electronic center of gravity.

Guinier (8-10) showed that for a dilute, monodisperse system in which the particles assume all orientations with equal probability the scattered intensity can be described by a power series

$$I(h) = I(0)\{1 - \tfrac{1}{3} h^2 R^2 + \ldots\} \tag{1-20}$$

The function I(0) is the intensity scattered at zero angle, which is proportional to the square of the total number of electrons in the system irradiated. To a good approximation Eq. (1-20) may be written as

$$I(h) = I(0) \exp[- \tfrac{1}{3} h^2 R^2] \tag{1-21}$$

which is the familiar law of Guinier. In logarithmic form Eq. (1-21) becomes

$$\log_e I(h) = \log_e I(0) - \tfrac{1}{3} h^2 R^2 \tag{1-22}$$

When the law of Guinier is closely obeyed by an actual system, a plot of the intensity curve I(h) versus h will be Gaussian, and a plot of $\log_e I(h)$ versus h^2 will be linear over a large angular

range with an ordinate intercept of $\log_e I(0)$ and a slope of $-\frac{1}{3}R^2$. The law of Guinier is obeyed most closely over a large angular range by monodisperse systems of approximately spherical particles. However, when the logarithmic plot becomes nonlinear with increasing angle as a result of departures from spherical shape or monodispersity, the limiting slope as h approaches zero is still related to the mean radius of gyration of the particles by this fundamental law (5).

1.4.2 The invariant Q. Integral scattering intensities of the form $\int_o^\infty h^2 I(h)dh$ have been termed the invariant Q by Porod (15). With intensities measured in absolute units, the invariant permits the determination, for any system, of the mean-square fluctuation of the electron density, $\overline{(\rho - \bar{\rho})^2}$, which may be called the scattering power of the system (5). Eq. (1-16) shows that the integral of the intensity over the reciprocal space is directly related to the mean-square fluctuation of electron density, regardless of special structural features (3). For example, if parts of the system were shifted or deformed, the diffraction pattern might change considerably, but the integral in Eq. (1-16) would remain invariant.

1.4.3 The scattering power. The scattering power in terms of mole electrons per cubic centimeter can be expressed as

$$\overline{(\rho - \bar{\rho})^2} = \frac{4\pi}{i_e N^2} \frac{1}{da\,\lambda^3} \int_o^\infty m^2 I_n(m)dm \qquad (1\text{-}23)$$

where i_e is the Thompson scattering constant of a free electron, N is Avogadro's number, d is the specimen thickness in centimeters, a is the specimen-to-receiver distance in centimeters, λ is the wavelength of x-rays in centimeters, m is the distance between the incident and scattered rays in the plane of registration in centimeters, and I_n is the intensity measured in absolute units (5). For a two phase system each of a uniform electron density separated by a sharp boundary, the expression for the scattering power is

$$\overline{(\rho - \bar{\rho})^2} = (\rho_1 - \rho_0)^2 w_1 w_0 = (\Delta\rho)^2 w_1 w_0 \qquad (1\text{-}24)$$

where w_1 and w_0 represent the volume fraction of each phase with $w_1 + w_0 = 1$. Then from a knowledge of $\Delta\rho$ and the scattering power, $\overline{(\rho - \bar{\rho})^2}$, the volume fraction of each phase can be calculated.

1.4.4 Porod's law. The experimental evaluation of the invariant is difficult because the scattered intensities at both very small and very large angles must be accurately determined. In the absence of particulate clustering or a large degree of polydispersity it is normally possible to determine the very low angle portion of the curve by extrapolating a plot of $h^2I(h)$ versus h to zero angle. The high angle portion of the intensity curve can be improved by making use of a theoretical finding of Porod (15) that in theory the tail-end of the scattering curve should conform to the asymptotic course h^{-4} for pinhole collimation. This is equivalent to saying

that $h^4I(h)$ should assume constant values

$$K = h^4I(h) \tag{1-25}$$

1.4.5 Specific inner surface. When it can be experimentally verified that the intensity in the tail of the scattering curve follows the theoretical course, the specific inner surface O_s can be obtained. It is defined as the ratio of the area of the phase interface O to the volume occupied by the disperse phase V and is expressed by the equation

$$O_s = \frac{O}{V} = \frac{2\pi^2}{a\lambda} w_1 w_o \frac{K}{Q} \tag{1-26}$$

where a is the sample to detector distance, λ is the wavelength of radiation, w_1 and w_o are the volume fractions of the two phases, Q is the invariant defined in Section 1.4.2 and K is the constant from Porod's law defined in Section 1.4.4.

CHAPTER 2

EPOXY RESINS

2.1 Introduction

Today's epoxy resin technology was begun in the 1930s by Schlack of I. G. Farben (18). Later, Castan in Switzerland described the production of diglycidyl ethers and esters and the polymerization of these resins with acid anhydrides and organic and inorganic bases (19,20). At the same time in the United States, Greenlee worked on the development of epoxy resins suitable for the surface coatings industry (21). Epoxy resins became commercially available about 1949 and have assumed a major role in the fields of reinforced plastics, surfacings, and adhesives. They have excellent resistance to attack by moisture and corrosive chemicals, and provide extraordinarily high strength to laminates and molded parts. The aerospace industry has used epoxies to great advantage in areas where other materials have provided unacceptable properties.

2.2 Epoxy Resin Chemistry

Epoxy resins contain the epoxide group, also called the oxirane or ethoxyline group, which is a three membered oxide ring. Epoxy resins can be regarded as compounds which contain two or more epoxide groups per molecule.

The parent epoxy resins can be broadly classified into the following five chemical groups: 1) glycidyl ethers, 2) glycidyl

esters, 3) glycidyl amines, 4) linear aliphatic, and 5) cycloaliphatic. The most important group of resins commercially available are the glycidyl ethers of dihydroxy compounds. The vast majority of all epoxy resins are made by the interaction of one molecule of bisphenol A, a diphenol derived from acetone and phenol which contains two reactive phenolic hydroxyl groups, with two molecules of epichlorohydrin (22,23). The original epoxide groups in the epichlorohydrin first react with the phenol to give an ether-alcohol. Then hydrochloric acid is lost and a new epoxide is generated.

Before they can be used for most of their applications, epoxy resins need to be converted by means of cross-linking reactions into a three-dimensional infusible network held together by covalent bonds. In epoxy resin technology, this conversion from a liquid into a tough cross-linked polymer is called curing or hardening. The resins cure into thermoset compounds by three reactions: 1) direct linkage between epoxy groups, 2) linkage of epoxy groups with aromatic or aliphatic hydroxyls, and 3) polymerization through the epoxide or hydroxyl groups using a cross-linking agent called a curing agent or hardener (24).

When the epoxide ring is opened, whether by polymerization with other epoxides or by reaction with a hardener, a large amount of heat is given off. As the temperature rises, the curing takes place at a faster rate. If the temperature is allowed to climb too high, the strength of the cured product will be impaired. The best

results seem to come from a two-stage cure. In the first stage, the small molecules are for the most part combined into larger units having only occasional interconnections. Then the temperature is raised, and in the second stage these clusters are jointed together at many points to form one big molecule (23).

2.3 Epoxy Resin Curing Agents

The curing agents fall broadly into two types, catalytic and polyfunctional (22). The catalytic curing agents serve as initiators for resin homopolymerization, whereas the polyfunctional curing agents function as reactants or comonomers in the polymerization leading mainly to the formation of a three-dimensional network composed of resin molecules cross-linked via the curing agents. In most of these curing reactions the actual mechanism is ionic in nature, both anionic and cationic polymerizations can occur, depending upon the curing agent concerned. When the curing agent is of the catalytic type, the percentage required for forming a three-dimensional network must be arrived at emperically for each epoxy system. When the curing agent is of the cross-linking type, there is a calculated optimum or stoichiometric ratio which theoretically provides exactly the amount of curing agent necessary for complete consumption of the reactive groups in the resin.

To obtain a three-dimensional network on curing, the functionality of the resin and curing agent combination must accord with Kienle's principle that one component must have a functionality greater

than two, and the other a functionality not less than two, their sum therefore being not less than five. Epoxide equivalent represents the accepted method of expressing epoxy resin functionality, and is the weight in grams of the amount of resin which contains one gram-mole chemical equivalent of epoxy. Epoxy value is another expression of epoxy resin functionality, and is defined as the number of epoxy groups contained in 100 grams of resin. Epoxy value is equal to the epoxide equivalent divided into 100. In order to determine the required resin and curing agent combining quantities, the amine equivalent is first determined by:

$$\frac{\text{Molecular weight of the amine curing agent}}{\text{Number of reactive hydrogen atoms in the amine molecule}}$$

The required amount of curing agent (X phr) is then determined by the equation:

$$X \text{ phr} = \left(\frac{100}{\text{Epoxide equivalent}}\right) \text{Amine equivalent} \qquad (2\text{-}1)$$

When the resin and curing agent are combined in optimum proportions, the cured material will have the highest softening temperature and the best combination of strength properties possible from the starting materials. An excessive amount of curing agent will tend to stop chain building at low molecular weights, thereby embrittling the resin. Too little curing agent will fail to provide for adequate cure.

A vast number of compounds have been screened for their suitability as curing agents. In general, epoxy resins will react with

compounds containing active hydrogen atoms, such as phenols, alcohols, thiols, primary and secondary amines, and carboxylic acids. The reactivity of the epoxide group towards any of these reagents will be different for each of the five resin types, depending as it does upon the electronic environment of the group and steric factors (22).

The choice of curing agent to be used with an epoxy resin will depend upon several factors: 1) the handling characteristics required or tolerable in the uncured system, such as viscosity at working temperature, pot life, exotherm, and toxicity, 2) the cure and post cure time and temperature requirements, and 3) the physical, mechanical, electrical, and chemical properties required of the cured system. The correct choice of curing agent can therefore be as important as the choice of the resin itself, both playing a part in determining the extent and nature of the intermolecular cross-linking. Curing agents have been classified into five broad categories.

2.3.1 Primary and secondary aliphatic amines. The amines were among the first materials to gain general acceptance as curing agents for epoxy resins. They are a group of unmodified room-temperature curing agents which can be regarded as having low viscosity and low cost, and being convenient to use. Diethylenetriamine (DETA) and triethylenetetramine (TETA) are the most widely used members of this group. Polyamides are also included in this group. These curing agents are aminopolyamides, produced from the reaction of dimerized and trimerized vegetable oil fatty acids with polyamines.

They offer, in addition to room-temperature curing, the absence of unpleasant vapors and the formation of tough, flexible, cured products.

2.3.2 Modified primary and secondary amines. These amines are room-temperature curing systems, developed to improve certain characteristics such as longer pot life, faster cures, and easier handling. The most commonly used modifications are those based on adducts of the polyamine with ethylene oxide, acrylonitrile, diglycidyl ethers and other compounds containing groups reactive towards the amino group, such as ketones. The physical properties of epoxy resins cured with these modified polyamines are similar to those of the unmodified amines (22).

2.3.3 Aromatic amines. Aromatic amines require high temperatures to bring about cure. Some are solids at room temperature, which can be difficult to mix with the epoxy resin. The aromatic amines offer the advantages of improved heat and chemical resistance and better strength retention properties at elevated temperatures. Another advantage is the ability to form dry brittle soluble solids when partially cured (B stage). These solids flow when heated, before finally forming a cured infusible network, and can therefore be used in the preparation of dry lay-up laminates. The most important aromatic curing agents are m-phenylenediamine (MPD), 4,4'-diaminodiphenylmethane (DDM), and 4-4'-diaminodiphenylsulphone (DDS).

2.3.4 Acid anhydrides. These compounds are one of the most important groups of curing agents and were among the first to be used to cure epoxy resins. Large numbers of anhydrides have been identified as curing agents, but most of the important ones are based on a cycloaliphatic structure. The acid anhydrides are a family of long pot life, low viscosity, and low reactivity, in the absence of a catalyst, which provides cured systems equal in performance to the aromatic amines. Since the anhydrides are characterized by low peak exothermic values, they must be cured for long periods at elevated temperatures to obtain optimum properties. However, the use of amine catalysts to reduce cure times and the introduction of easy mixing liquid anhydrides has offset many of the former disadvantages of the acid anhydride curing agents. The commercially available anhydrides may be considered to fall into three classes: 1) room-temperature solids, 2) room-temperature liquids, and 3) chlorinated derivatives. Phthalic anhydride (PA), maleic anhydride (MA), hexahydrophthalic anhydride (HHPA), and pyromellitic dianhydride (PMDA) may be considered representative of the first class; a methylated maleic adduct of phthalic anhydride, nadic methyl anhydride (NMA) and dodecenyl succinic anhydride (DDSA) may be considered representative of the second; and chlorendic anhydride of the third (24). NMA is the most versatile of all the anhydrides, since the balance of properties of the final casting can be varied over a wide range by changing the type and concentration of the catalyst, altering the resin-to-curing agent ratio, and modifying the cure schedule (22).

2.3.5 Catalytic curing agents. Catalytic curing agents achieve cross-linking by initially opening the epoxide ring and causing homopolymerization of the resin. The resin molecules react directly with each other and the cured polymer has essentially a polyether structure. Catalytic curing agents can be used in any of three ways: 1) as a sole curing agent, 2) as a co-curing agent in conjunction with a polyamine or polyamide, or 3) as an accelerator for anhydride systems. Catalytic curing agents usually offer special properties, and frequently have long pot lives at room temperature. The catalysts may be strong Lewis bases such as tertiary amines or strong Lewis acid materials such as boron trifluoride.

2.4 Characterization of Cured Epoxy Resin

The structure of a cured epoxy resin can be varied by changes in the resin type and the curing agent type. The large variety of molecular compositions possible leads to an unusually large range of cured properties for a polymer system. The characteristics of the cured resin are therefore based on the molecular structure of the polymerized resin. Some of the important factors at the molecular level in determining these properties are: the extent of cross-linking, the cross-link density, the nature of the resin molecule between cross-links, and the nature of the curing agent molecule.

To obtain the most favorable properties in any cured resin system, it is important to achieve maximum cross-linking efficiency. With epoxies, the initial cure is accompanied by exotherm, low

viscosity, and then gelation. Reactive molecules in the polymer network that are trapped at the gel stage, and are thus prevented from reacting, may prevent maximum cross-linking from being achieved. To establish optimum physical properties, this condition can often be improved by a post-cure at a temperature above the original cure temperature and above the glass transition temperature for the system. Such post-cures are usually made in temperature steps with the temperature held until the heat has permeated through the full thickness of the part. The increased molecular mobility brought about by heating gives the immobilized molecules a further opportunity to undergo collision and bond formation.

Experimental results obtained by Kong, Hoffman, and Morgan (25) on polyether triamine cured bisphenol A-diglycidyl ether epoxies have shown that the highest cross-link density occurs at the amine content associated with complete cure for networks formed exclusively from epoxide-amine addition reactions. The mass density, on the contrary, exhibits a minimum value at this amine content, which implies that the fully cross-linked network inhibits intermolecular packing and enhances the free volume of the cured epoxy.

The cross-link density in different systems depends upon the functionality of the reacting species and the distance between their reactive groups. The nature of the resin or curing agent molecule between reactive groups, whether it is rigid or flexible, also has a direct influence on physical characteristics. Resin systems with

high cross-link densities normally exhibit higher heat-distortion temperatures and glass transition temperatures than those with more widely spaced cross-links, and it was the need for increasingly temperature-resistant systems that led to the development of resins and curing agents with increased functionality. Cross-link density is increased not only by increasing the functionality of the reacting species, but also by decreasing the distance between the functional groups. This leads to improvements in short-term thermal stability, chemical resistance, and tensile and compressive strengths.

2.5 Morphology of Cured Epoxy Resins

The original simple model of network structure (26) predicted that a polymer network would be homogeneous with crosslinks distributed throughout the material at random. More recent theoretical studies of network structure have shown that the formation of inhomogeneities should be a frequent occurrence in the synthesis of networks. In epoxy systems, regions differing in cross-link density can be formed in the polymer, the extent depending on the chemistry of the system and the polymerization conditions.

There are two possibilities in the way in which the cross-linked and non-cross-linked molecules are distributed throughout the polymer. First, the cross-linked network is like one giant molecule with the uncured material occupying holes in the network. The second possibility is that the cross-linked molecules may be aggregated together in well defined regions, surrounded by or embedded in the

unpolymerized molecules. Erath and his coworkers (27,28) have obtained evidence that the second possibility is the correct one. An electron microscopic study of cured epoxy resins showed globular formations or micelles existed in the cured polymer having diameters of 400-900 Å. Koutsky and his coworkers (29,30) used replica electron microscopy and observed nodular structures on free surfaces, fracture surfaces and etched surfaces of epoxy resins of widely different cures and chemistries. The sizes of the heterogeneities seen in these studies were generally in the range of 100-300Å. Morgan and O'Neal (31-33) used both replica and direct-transmission electron microscopy as well as scanning electron microscopy to characterize the structural features of epoxy resins. They reported heterogeneities on a number of scales, with particles 60-90 Å in diameter suggested as intramolecularly cross-linked molecular domains which could interconnect to form larger network arrays. Small-angle x-ray scattering results obtained by Matyi et al. (34) are inconsistent with the presence of nodular structures visible in direct transmission electron microscopy of thin specimens, and set constraints on the characteristics of heterogeneities seen using replica electron microscopy.

The cured resin system is best characterized by its physical, chemical, and electrical properties. The cured resin system will not have optimum values in all of its properties, but will represent a compromise designed to accommodate a specific service environment. There are many standard ASTM test procedures employed to determine the values for each property.

CHAPTER 3

FIBER REINFORCEMENTS

3.1 Kevlar® 49 Fibers

Kevlar® is a high modulus aramid fiber produced by E.I. du Pont de Nemours and Co. Aramid fibers represent a new class of materials which are of great interest because of their exceptional mechanical properties. The fibers have been shown to be comprised of poly (p-phenylene terephthalamide) (PPTA) (35). Kevlar® 49 fibers are being utilized in high performance fiber reinforced epoxy composites.

3.1.1 Kevlar® 49 fiber production. PPTA polymers, such as Kevlar®, can be made by a condensation polymerization of the stoichiometric ratio of the acid chloride of terephthalic acid with p-phenylenediamine in a suitable solvent such as hexamethylphosphoramide or N-methylpyrrolidone. The polymer is washed with dilute NaOH to neutralize HCl formed during polymerization.

Kevlar® fibers are dry-jet wet spun from liquid crystalline PPTA-H_2SO_4 dopes. The fibers are washed with water, neutralized with NaOH, and washed again with water to remove the Na_2SO_4. The fibers are dried on rollers under tension. For Kevlar® 49 type fibers, the fibers are drawn 0.5% further at 550°C for one to six seconds. The detailed description of the polymerization and fiber fabrication of PPTA is described by Blades (36).

3.1.2 Morphology of Kevlar® 49 fibers. The unit cell of PPTA was evaluated by Northolt (37), and determined to be monoclinic (pseudo-orthorhombic) with a = 0.719 nm, b = 0.518 nm, c (fiber axis) = 1.29 nm, and γ = 90°. Each unit cell contains two molecular chains. Figure 3-1 shows the repeat unit and the crystal structure of Kevlar® 49.

Wide-angle x-ray diffractometer scans of PPTA fibers show no evidence of an amorphous fraction. The fibers are considered to be fully crystalline within the limit of detection. Quantitive analysis of the equatorial x-ray diffraction scan indicates an average crystallite width of 7 nm normal to the fiber axis (39). Ballou reported that the lateral order of the crystallites relative to the phenyl group plane can vary from radial to tangential to completely random packing in any given fiber (40).

In polymeric materials, an alternation of crystalline and amorphous regions gives rise to meridional x-ray scattering at small angles which is identified as the long period. In PPTA fibers, discrete maxima associated with the defect period have not been observed using CuKα radiation. The high crystallinity of the fibers suggests that the absence is consistent with a limited amount of material in the defect layer (38). Low-energy aluminum Kα radiation has detected a meridional peak corresponding to a period of about 30 nm (45). A 30-40 nm periodicity can be quantitatively observed from surface replicas of plasma-etched fibers (38). This periodicity represents a potential weak link in the axial structure.

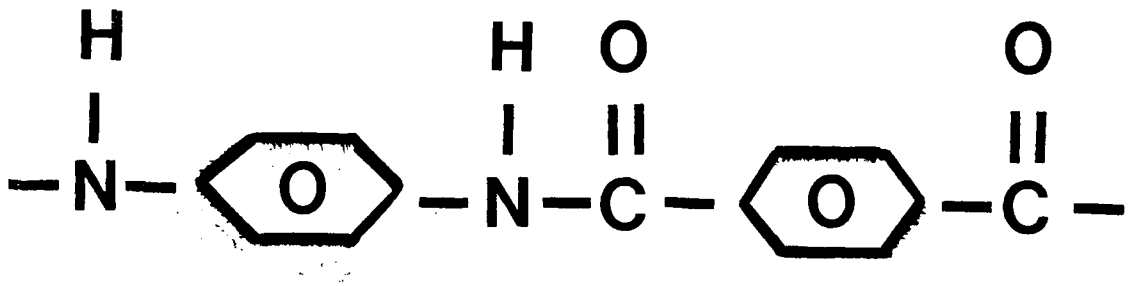

(a)

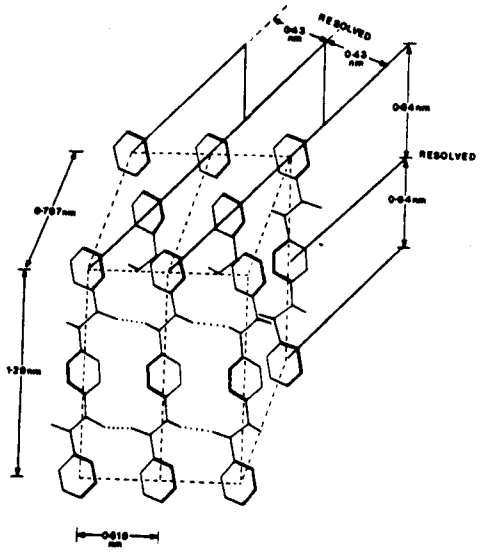

(b)

Figure 3-1. (a) Chemical Repeat Unit of Kevlar® 49; (b) the Crystal Structure of Kevlar® 49 (43).

It has been reported that high-modulus PPTA fibers have a fibrillar morphology. These fibrils appear to be about 600 nm in cross section, are extremely flexible, and appear to be joined together by tie bundles (38). The individual fibrils consist of extended-chain, rod-like macromolecules that are aligned in the fiber direction and have a high proportion passing through the periodic defect layers. The high level of extended chains passing through the defect layer is an important factor distinguishing high-modulus fibers from normal fibers. Dobb et al. (42) have shown by using electron diffraction studies that Kevlar® 49 fibers consist of a system of H-bond sheets of these macromolecules pleated regularly along the fiber axis and arranged radially. This pleated structure is shown in Figure 3.2.

Dobb et al. (42) noted that a number of dark-field images indicate the possibility of a skin-core heterogeneity. From fracture topography studies of Kevlar® 49 fibers failed in tension, Morgan et al. (44) showed that the fibers contain a skin that can tear off the fiber in the longitudinal fiber direction to form a continuous ribbon. They have proposed a chain-end model for PPTA fibers. In this model, the PPTA macromolecules are assumed to be aligned parallel to the fiber axis. The fiber skin is assumed to be less crystalline than the core with the chain ends arranged essentially randomly relative to one another. In the fiber core, the chain ends become progressively more clustered, resulting in periodic transverse weak planes about every 200 nm along the fiber axis. This corresponds to the

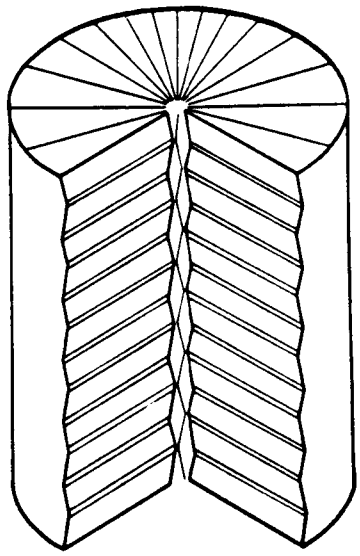

Figure 3-2. Schematic Diagram of Radially Arranged Pleated Sheets in Kevlar® 49 Fibers (42).

average length of the PPTA macromolecule. The fiber core consists of cylindrical crystallites about 60 nm in diameter which have some degree of structural continuity in the fiber direction. The chain end model is illustrated in Figure 3-3.

Kevlar® 49 fibers have been shown to have a diffuse equatorial small-angle scattering pattern which has been attributed to scattering by elongated voids with their long axes approximately parallel to the fiber axis (41). The origin of the voids has been attributed to the removal of sulfuric acid during the solidification process of the extruded polymer in the coagulating bath. The distribution of voids would reflect differences in rates of solidification between different parts of the fiber. Subsequent heat treatment may also produce further void formation since some localized shrinkage would be expected from the improvement in molecular packing associated with the observed increase in crystallite size (46). Dobb et al. (46) have identified microvoids in stained Kevlar® 29 and Kevlar® 49 fibers. The electron microscope evidence indicates that the microvoids are rod-shaped with their long axes almost parallel to the fiber axis and often appear to be isolated from each other. Due to the microvoid accessibility towards reagent molecules, they have suggested that the microvoids are located mainly around the periphery of the fibers and are connected by a fine capillary network to the fiber surface. Another possibility is a system of voids having two components, one where the voids are completely isolated and another

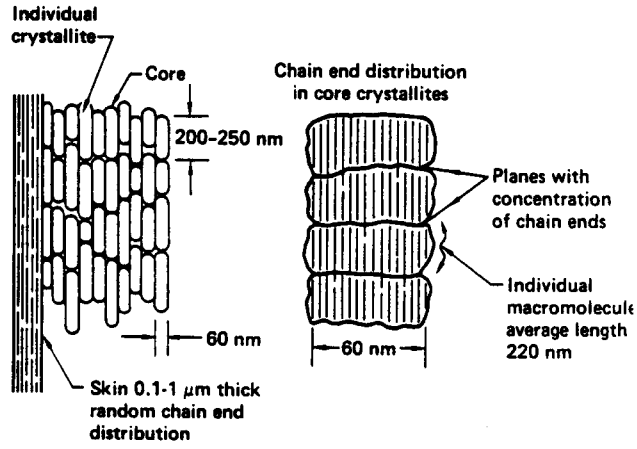

Figure 3-3. Chain End Model in Kevlar® 49 Fibers (44).

where the voids are connected directly to the fiber surface. Panar et al. (38) have suggested a model where the majority of voids are located in the fiber core. Using plasma etching, they showed that when Kevlar® fiber ends are exposed to the plasma, the fiber core is preferentially degraded. This would indicate that a large number of voids allowed increased accessibility of plasma to the fiber core. Also, optical micrographs have shown that dye goes selectively to the core of the fibers either from the fiber ends or through cracks in the skin in damaged fibers.

The presence of voids will adversely affect the mechanical properties of the fibers. Voids will tend to reduce both the potential lateral and tensile strengths of a fiber. If the voids have a length to width ratio greater than one then the effect will be greater on the lateral than on the tensile properties, thus contributing to a low compressive strength (46).

3.2 Graphite Fibers

Commercial carbon and graphite fibers are derived either from fibrous organic precursors or by the extrusion of pitch. Graphite fibers consist essentially of carbon atoms, which by high temperature heat treatment, have obtained a crystalline state with a high degree of three-dimensional order as determined by x-ray diffraction patterns. Carbon fibers show a lower degree of three-dimensional order or may be almost amorphous. Graphite fibers have higher modulus and strength, and are better electrical and thermal conductors.

3.2.1 The graphitization process. Graphitization involves a displacement and rearrangement of layer planes and small groups of planes to achieve three-dimensional ordering. The growth of such planes may be supplemented by movement of individual atoms or single carbon rings to fill vacancies or improve perfection in existing crystallites. Franklin (47) established an explanation for the inability of some carbons to form a fully graphite structure, regardless of heat treatment, based on the structure of the raw materials. Maximum temperature and residence time at temperature are important factors in the graphitization process in addition to the structure of the precursor. Mechanical properties differ with respect to the top graphitizing temperature. All graphite physical properties do not achieve optimum values at any one temperature (48).

Slow carbonization has the advantage of increasing the carbon yield. Variations in the carbonization process result in carbon fibers having widely different properties. The preparation of graphite fibers requires an additional thermal treatment in the 2500° to 3000°C range. Graphitization proceeds from the outside of the fiber inward. During graphitization there may be shrinkage of 3 to 6%; a typical weight loss of 5 to 15% and an increase in the density of the fiber, although the amount of change depends on the precursor and process. By the time graphitization is completed, virtually all of the original oxygen and hydrogen have been eliminated, and the final carbon content is over 99.0% (49).

3.2.2 Morphology of graphite fibers. The crystal structure of graphite was detemrined by Bernal (50) in 1924. The results indicate that the unit cell is that of a simple hexagonal lattice with height 0.682 nm and length of side 0.245 nm. The unit cell contains four atoms of carbon. The atoms are arranged in the corners of hexagons in parallel planes whose vertical distances apart are half the height of the unit cell. Within each layer, the carbon-carbon bond distance is 0.1415 nm. The crystal structure of graphite is shown in Figure 3.4. The theoretical density for the ideal structure is 2.265 g/cc. The density of a single crystal of graphite has been measured and determined to be 2.25 g/cc.

The development of crystallites during graphitization can be followed by x-ray diffraction techniques in which carbon samples are heat treated to different temperatures. Development of the 002 and 004 peaks indicates crystallite growth. During graphitization, crystallite size increases from 5 nm to about 100 nm, while interlayer spacing decreases from the 0.344 nm typical of amorphous carbon to the 0.335 nm accepted for the graphite structure. The c-axis of the graphite crystallites has been found to be perpendicular to the fiber axis (51).

The distinction between carbon fibers and graphite fibers is primarily one of degree of crystalline order. Physical differences, such as density of fibers and elastic moduli, will also be apparent. The original fiber precursors will have an influence on the ordering

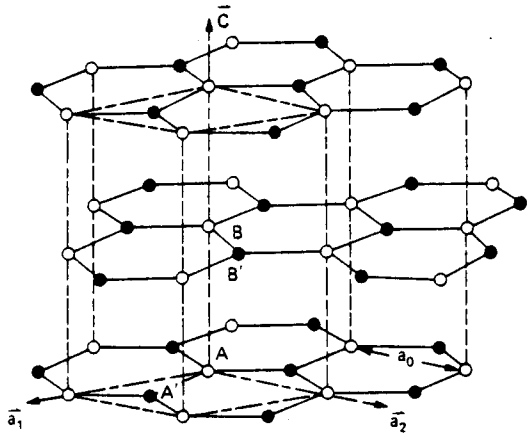

Figure 3-4. Hexagonal Structure of Crystalline Graphite (50).

of the carbons in the graphite fiber, as well as the tensile stresses on the fiber during graphitization. Graphite fibers do not comprise 100% pure graphite crystals and retain a certain amount of the amorphous form of carbon. The coexistence of crystalline graphite and turbostratic carbon phases was detected in graphite yarns prepared from aromatic polyamide and acrylonitrile homo- and co-polymer fibers by Ezekiel (52).

The growth of the graphite layers in carbon fibers has been studied by Ruland and Perret (53) by wide-angle scattering techniques. The layers grow to about 60 Å width and probably hundreds or thousands of Angstroms in length. At the same time, uniform parallel stacking of layers occurs so that layer packets, although still turbostratic are otherwise relatively crystalline.

Cross sections of some of the carbon fibers show an irregularly wavy circumference. This may reflect very rapid drying of their organic fiber precursor during the wet spinning process. Most of the commercial carbon/graphite fibers fall in the range of 6 to 11 microns in diameter (49).

3.2.2.1 Morphology of PAN based graphite fibers. The structure of commercial polyacrylonitrile (PAN) based graphite fibers are circumferentially oriented on the outside and radially oriented on the inside (49,54). Bennet and Johnson (55) present evidence for a thin surface layer (150-250 nm) with larger crystallites and a higher degree of orientation than the interior of the fiber. Since the

oxidation of the PAN fibers is diffusion controlled, the surface materials see a different oxidizing environment than the core material. Thus, the carbonization and graphitization results at the fiber surface and the core would be expected to be different (49).

The main elements of the graphite fiber structure are the graphitic lamellar ribbons. The variation in these structural elements depends on the graphitization temperature and processing of the particular fiber. The x-ray diffraction pattern of a bundle of PAN fibers heated to 200°C was of the fiber structure similar to that of the original PAN. The pattern of a fiber bundle heated to 300°C contained that of carbon, and a fiber bundle heated to 400-1000°C gave patterns indicating the presence of polynuclear aromatic fragments whose ring planes are oriented parallel to the fiber axis (51).

High modulus graphite fiber is processed at high temperatures (above 2500°C) causing a high degree of axial alignment. The graphitic lamellar ribbons are about 20 basal layers thick and are 7 nm wide with a majority of the graphitic basal planes oriented within 12° of the fiber axis. There is a small amount of ribbon intertangling and the graphitic basal planes are oriented radially parallel to the fiber surface (55). Johnson and Watt (56) and Badami et al. (57) have found evidence for a fibrillar structure unit 25-100 nm in diameter in high modulus carbon fibers made from PAN precursors.

When carbon yarn is graphitized, the internal structure becomes highly textured. A well-defined pore structure develops. The graphitization process results in a reduction in the number of small pores

present in carbon fibers and the development of larger pore sizes. As these larger pores are formed, they also become closed. This pore structure has been studied quantitatively and in detail by small angle x-ray scattering techniques by Perret and Ruland (58). When the carbon yarn is graphitized under stress to produce a high modulus fiber, the fiber structure becomes highly oriented. In this case, it is possible to identify individual pores extending several hundreds of Angstroms in length. A model of a PAN-based graphite fiber is shown in Figure 3-5.

3.2.2.2 Graphite fiber production from pitch. A method of manufacturing carbon fibers from pitch was developed by Singer (59). Commercial pitches are complex mixtures of aromatic compounds which, when heated to temperatures of 350°C or higher, undergo dehydrogenation condensation reactions to form planar aromatic molecules which aggregate into a liquid crystalline phase (mesophase). When the mesophase content reaches about 40%, a phase inversion occurs and this anisotropic material becomes the continuous phase. The degree of preferred orientation obtained in raw mesophase pitch fibers is high, as shown by the x-ray diffraction patterns of collimated bundles of as-spun pitch fibers (49). Improved techniques have been developed for converting the mesophase pitch to high modulus graphite fibers without sacrifice of tensile strength.

Fibers extruded from pitch at rates of 100 up to 1000 feet per minute will have diameters of 10 to 20 microns. The pitch must

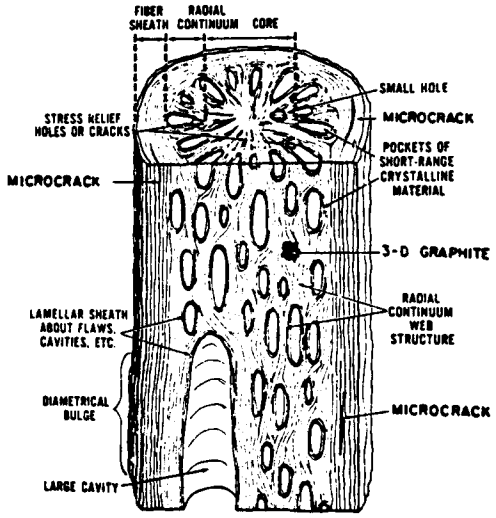

Figure 3-5. Schematic Diagram of a PAN-Based Graphite Fiber (62).

be non-thixotrophic and exhibit Newtonian or plastic flow during the spinning of the fibers. Fibers having a carbon content greater than 98% are obtained by carbonization in an inert atmosphere at temperatures in excess of 1000°C.

3.2.2.3 Morphology of pitch based graphite fibers. Carbon/graphite fibers from pitch have a more uniform cross section than those from other precursors, as the pitch products have had significant processing to remove volatile matter before the extrusion operation to yield fibers with higher density and carbon content. Carbon fibers produced at temperatures in excess of 1000°C have a highly oriented structure characterized by the presence of carbon crystallites aligned parallel to the fiber axis. Further grahpitization at temperatures above 2800°C develops the three dimensional order characteristic of polycrystalline graphite.

Tomizuka et al. (60) have studied the small-angle x-ray diffraction from pitch-based carbon fibers. There were almost no voids in the fibers carbonized at 1000°C, but voids developed as the heat-treatment temperature increased. Values for the radius of gyration of voids in the fiber heat treated at 2000°C were 1.3 nm along the equator and 1.2-1.8 nm along the meridian.

Electron microscope studies on these fibers were performed by Johnson et al. (61). Although there is no preferred orientation in the fibers carbonized at 1000°C, ill-defined lattice fringes were observed which revealed that in terms of stacking size and lattice

order this specimen is inferior to oriented PAN-based fibers heat treated at the same temperature. The lattice structure was also less well developed than that observed in pitch-based carbon fibers heat treated at 700°C. There was no evidence of identifiable voids in the micrographs of these fibers, an observation which confirmed the earlier small-angle x-ray diffraction analysis. In fibers carbonized at 2000°C, lattice fringes were observed and this specimen had considerably improved lattice order over the 1000°C material. The crystalline fibrils form entangled networks which necessarily enclose a large void content.

CHAPTER 4

COMPOSITES

4.1 Introduction

A composite is created by the assembly of two or more materials, namely, a reinforcing element and a compatible resin to obtain specific characteristics and properties. The unidirectional fibrous composite is the simpliest two-phase material constructed by embedding a system of parallel fibers in a matrix. In order to understand the mechanical properties of the composite, it is necessary to physically identify the components and the interface that exists between them. In general, polymers contribute the properties of toughness, low density, low strength, low stiffness, high thermal expansivity and low thermal stability in both a physical and chemical sense to the composite. On the other hand, fibers typically contribute high modulus, high strength, and often the disadvantage of brittleness. Together, the two components can be made to draw on each other's good properties, to compensate for the poor properties.

Mechanical performance of a fiber reinforced plastic composite is primarily dependent upon three factors: 1) strength and modulus of the fiber, 2) strength and chemical stability of the resin, and 3) effectiveness of the bond between resin and fiber in transferring stress across the interface. Several parameters contribute to the strength of the composite. Surface properties such as the area itself,

surface reactivity, and wettability are perhaps the most important. Other factors such as fiber variability, type of resin, and fabrication methods also affect load strength. Even when all these factors are considered, it must be determined if the failure occurred in the fiber, the resin matrix, or at the fiber-resin interface. Anything in the total system can be the weak link which is the limiting factor in a composite's mechanical properties.

4.2 Macromechanical Behavior of Fiber Composites

Many quantities of physical interest depend only upon the bulk or macroscopic behavior of the solid. For the calculation of such quantities for a composite material, the material is presumed homogeneous and the effects of the constituent materials are detected only as averaged apparent properties of the composite (68). The elastic constants of fiber composites are important in the characterization of the mechanical properties such as the strength and fracture properties, their stress analysis and their response to an external force. Chamis and Sendeckyj (69) and Rosen (70) have discussed the various methods of calculations of the elastic constants of fiber composites. The possibility of qualitative predictions of the composite properties from the fiber and matrix properties have been considered by Dimmock and Abrahams (71).

Several models have been developed for the calculation of elastic constants of composites. In order to model a fiber composite, several assumptions must be considered.

1. The fibers are straight, continuous and well-aligned. They extend throughout the length of the composite and are of uniform cross-section and strength.
2. The matrix is homogeneous and free from voids, cracks, and other material defects.
3. The bonding between the fibers and the matrix is perfect. The fiber-matrix interface does not make an independent contribution to the elastic constants of the composite.
4. The composite is macroscopically homogeneous. This implies that if a sample piece is cut out of the composite, it has the same physical properties as the whole composite.
5. The fibers as well as the matrix are elastic, so that the linear theory of elasticity is applicable. In this case, the stress and the strain are proportional to each other according to Hooke's law, which is valid if the strain is small.

4.2.1 Elastic constants. For a unidirectional fiber composite illustrated in Figure 4-1, the most readily available elastic constant is Young's modulus, E. It is defined by an equation of the type

$$E_i = \sigma_i/\varepsilon_i \tag{4-1}$$

where σ_i is the stress in the i-direction and ε_i is the strain in the i-direction. This value is measured in a uniaxial tensile test where all stresses except σ_i are zero.

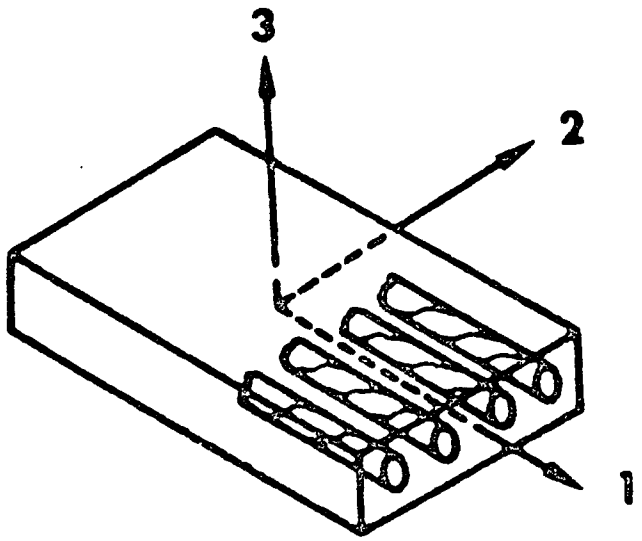

Figure 4-1. Unidirectionally Reinforced Lamina (68).

In a tensile test, it is found that contractions occur normal to the direction of the applied stress. These may be used to determine another elastic constant, Poisson's ratio, ν, by the equation

$$\nu_{ij} = -\varepsilon_j/\varepsilon_i \tag{4-2}$$

for transverse strain in the j-direction when stressed in the i-direction.

The third elastic constant to be considered is the shear modulus, G, defined by an expression of the type

$$G_{ij} = \tau_{ij}/\gamma_{ij} \tag{4-3}$$

where τ_{ij} is the shear stress and γ_{ij} is the shear strain in the i-j plane.

By micromechanical analysis, it is possible to relate the elastic constants of the fiber and the matrix and their fractional volumes in the material by an equation of the type

$$E_c = E_f V_f + E_m V_m \tag{4-4}$$

where E_c, E_f, and E_m are the moduli of the composite, fiber, and matrix and V_f and V_m are the volume fractions of fiber and matrix. This is an example of the rule of mixtures.

4.2.2 Stress-strain relations for anisotropic materials. The generalized Hooke's law relating stresses to strains can be written in contracted notation as

$$\sigma_i = C_{ij}\varepsilon_j \qquad i,j = 1, \ldots, 6 \tag{4-5}$$

where σ_i are the stress components, C_{ij} is the stiffness matrix, and ε_j are the strain components. If it is required to calculate strains, the compliance matrix, S_{ij}, defined by the inverse of the stress-strain relations, is used in the strain-stress equation

$$\varepsilon_i = S_{ij}\sigma_j \qquad i,j = 1, \ldots, 6 \tag{4-6}$$

As with isotropic materials, there are normally six independent stresses and six independent strains for anisotropic materials. This gives the stiffness and compliance matrices a total of thirty-six constants. However, both matrices are symmetric, i.e. $C_{ij} = C_{ji}$ and $S_{ij} = S_{ji}$, therefore each matrix has only twenty-one independent constants.

The strain-stress relations are

$$\begin{vmatrix} \varepsilon_1 \\ \varepsilon_2 \\ \varepsilon_3 \\ \gamma_{23} \\ \gamma_{31} \\ \gamma_{12} \end{vmatrix} = \begin{vmatrix} S_{11} & S_{12} & S_{13} & S_{14} & S_{15} & S_{16} \\ S_{12} & S_{22} & S_{23} & S_{24} & S_{25} & S_{26} \\ S_{13} & S_{23} & S_{33} & S_{34} & S_{35} & S_{36} \\ S_{14} & S_{24} & S_{34} & S_{44} & S_{45} & S_{46} \\ S_{15} & S_{25} & S_{35} & S_{45} & S_{55} & S_{56} \\ S_{16} & S_{26} & S_{36} & S_{46} & S_{56} & S_{66} \end{vmatrix} \cdot \begin{vmatrix} \sigma_1 \\ \sigma_2 \\ \sigma_3 \\ \tau_{23} \\ \tau_{31} \\ \tau_{12} \end{vmatrix} \tag{4-7}$$

Orthotropic materials have three mutually orthogonal planes of symmetry. There is no interaction between normal stresses, σ_1, σ_2, σ_3 and shearing strains γ_{23}, γ_{31}, γ_{12}. Conversely, there are

no interactions between shearing stresses and normal strains. A uniaxial fiber reinforced composite stressed in the fiber direction is an example of an orthotropic material. Now, the number of independent constants has been reduced to nine. Therefore, equation (4-6) becomes

$$\begin{vmatrix} \varepsilon_1 \\ \varepsilon_2 \\ \varepsilon_3 \\ \gamma_{23} \\ \gamma_{31} \\ \gamma_{12} \end{vmatrix} = \begin{vmatrix} S_{11} & S_{12} & S_{13} & 0 & 0 & 0 \\ S_{12} & S_{22} & S_{23} & 0 & 0 & 0 \\ S_{13} & S_{23} & S_{33} & 0 & 0 & 0 \\ 0 & 0 & 0 & S_{44} & 0 & 0 \\ 0 & 0 & 0 & 0 & S_{55} & 0 \\ 0 & 0 & 0 & 0 & 0 & S_{66} \end{vmatrix} \cdot \begin{vmatrix} \sigma_1 \\ \sigma_2 \\ \sigma_3 \\ \tau_{23} \\ \tau_{31} \\ \tau_{12} \end{vmatrix} \tag{4-8}$$

Plane stress conditions can be assumed for a lamina. The plane stress state is defined by

$$\sigma_3 = \tau_{23} = \tau_{31} = 0 \tag{4-9}$$

Strains are still present normal to the plane of the lamina:

$$\varepsilon_3 = S_{13}\sigma_1 + S_{23}\sigma_2 \tag{4-10}$$

The in-plane strain-stress relations become

$$\begin{vmatrix} \varepsilon_1 \\ \varepsilon_2 \\ \gamma_{12} \end{vmatrix} = \begin{vmatrix} S_{11} & S_{12} & 0 \\ S_{12} & S_{22} & 0 \\ 0 & 0 & S_{66} \end{vmatrix} \cdot \begin{vmatrix} \sigma_1 \\ \sigma_2 \\ \tau_{12} \end{vmatrix} \tag{4-11}$$

Engineering constants can be used in place of the compliances:

$$S_1 = 1/E_1 \tag{4-12}$$

$$S_{12} = -\nu_{12}/E_1 = -\nu_{21}/E_2 \tag{4-13}$$

$$S_{22} = 1/E_2 \tag{4-14}$$

$$S_{66} = 1/G_{12} \tag{4-15}$$

The strain-stress relations can be inverted using reduced stiffnesses, Q_{ij}, to obtain the stress-strain relations.

$$\begin{vmatrix} \sigma_1 \\ \sigma_2 \\ \tau_{12} \end{vmatrix} = \begin{vmatrix} Q_{11} & Q_{12} & 0 \\ Q_{12} & Q_{22} & 0 \\ 0 & 0 & Q_{66} \end{vmatrix} \cdot \begin{vmatrix} \varepsilon_1 \\ \varepsilon_2 \\ \gamma_{12} \end{vmatrix} \tag{4-16}$$

where

$$Q_{11} = \frac{S_{22}}{S_{11}S_{22} - S_{12}^2} = \frac{E_1}{1 - \nu_{12}\nu_{21}} \tag{4-17}$$

$$Q_{12} = \frac{S_{12}}{S_{11}S_{22} - S_{12}^2} = \frac{\nu_{12}E_2}{1 - \nu_{12}\nu_{21}} \tag{4-18}$$

$$Q_{22} = \frac{S_{11}}{S_{11}S_{22} - S_{12}^2} = \frac{E_2}{1 - \nu_{12}\nu_{21}} \tag{4-19}$$

$$Q_{66} = \frac{1}{S_{66}} = G_{12} \tag{4-20}$$

The preceding stress-strain and strain-stress relations are the basis for the stiffness and stress analysis of an individual lamina subjected to forces in its own plane. There are four independent material properties E_1, E_2, ν_{12}, and G_{12} in addition to the reciprocal relation

$$\frac{\nu_{12}}{E_1} = \frac{\nu_{21}}{E_2} \tag{4-21}$$

4.2.3 Fracture and failure processes. The elastic constants give the response of a material to an applied stress as long as the strain is small. When the applied stress in the material exceeds a certain value, called the yield stress, stress is no longer proportional to strain and the material enters the plastic region. When the stress is increased even further, ultimately the atomic bonds are broken and the material is cracked or fractured. Initially, the cracks are localized, then they increase in size as the stress is increased further.

The importance of the study of fracture and failure properties for engineering applications is to be able to predict the occurrence of failure at a certain value of the applied load and/or after a certain duration due to material fatigue. The characteristic problem in the case of a composite which makes it different from an ordinary solid arises from the fact that a composite has more than one component. The different components have, in general, different elastic

constants and different ranges pertaining to the three regions on the stress-strain diagram. Therefore the composite exhibits neither purely elastic nor plastic behavior at intermediate strains. For a two-phase composite, three distinct possibilities exist: 1) fibers and matrix both elastic, 2) fibers elastic, matrix plastic, and 3) fibers and matrix both plastic. An appropriate theory for the fracture properties of the composite must therefore account for the mixed response of its components. Most of the calculations on the stress-strain relations and the critical stress in a composite are based on the law of mixtures as originally given by Dietz (72) for plastics reinforced by glass. Although the law of mixtures has only limited validity, it is very useful for a rough estimate of the overall failure properties of a composite on account of its simplicity.

According to Cooper (73), the fracture of a composite under tension can be classified into two categories: single fracture and multiple fracture. A composite fails by a single fracture if both the components are fractured at the same point along their axes, and in this case the composite will immediately break into two pieces. When the component of a composite with the lower breaking-strain fails, complete fracture of the composite may not ensue. If the composite stress at that instant is less than the product of the strength of the higher failure strain component and its volume fraction, this component can bear the load without breaking. Multiple fracture of the other component then occurs.

A simple criteria can be derived for the occurrence of single and multiple fractures in a two-component composite. If a tensile load is applied in the direction parallel to the fiber axis so that a longitudinal stress, σ, produces a uniform elastic strain, ε, in the composite, then the law of mixtures gives the equation

$$\sigma = V_1 E_1 \varepsilon + V_2 E_2 \varepsilon \tag{4-22}$$

where V_1 and V_2 are the volume fractions of the composite and E_1 and E_2 are the Young's modulus of each component. If it is assumed that ε_1, the failure strain of component 1, is larger than ε_2, the strain at which component 2 fails and the region $0 \leq \varepsilon \leq \varepsilon_2$ is elastic, then the value of σ at $\varepsilon = \varepsilon_2$ is given by

$$\sigma_c^1 = V_1 E_1 \varepsilon_2 + V_2 \sigma_2 \tag{4-23}$$

where $\sigma_2 = E_2 \varepsilon_2$ and σ_c^1 is the stress at which component 2 will fail. Thus the conditions for single fracture can be written as

$$V_1 \sigma_1 < \sigma_c^1 \tag{4-24}$$

and for multiple fracture as

$$V_1 \sigma_1 > \sigma_c^1 \tag{4-25}$$

where $\sigma_1 = E_1 \varepsilon_1$ is the stress at which component 1 will fail.

In the case of a multiple fracture, the critical stress at which the whole composite will fail is given by

$$\sigma_c = V_1 \sigma_1 \tag{4-26}$$

In this case, the composite will behave like a ductile material even if both the components are brittle. The yield stress of the composite will be equal to σ_c^1 and it will exhibit a plastic-type behavior between σ_c^1 and σ_c. This apparent ductility is a useful feature of multiple fracture, which is not available with composites which fail by single fracture.

Theoretical and experimental aspects of single and multiple fracture in various composites have been given in the following papers: Kelly (74), Kelly and Tyson (75), Cooper and Sillwood (76), and Aveston and Kelly (77). Several books discussing the mechanics of composites as well as fracture include Jones (68), Piggott (63), Tewary (78), Sheldon (79) and Hashin and Herakovich (80).

4.3 Unidirectional Kevlar® 49/Epoxy Composites

Kevlar® is a synthetic aromatic polyamide fiber normally made with a diameter of 12 microns. Kevlar® fiber has a density of 1.45 g/cm^3. It has a tensile modulus of 130 GPa and strength of 3.6 GPa. It is very tough when compared to other high-performance fibers, but it has poor compressive properties. The compressive strength is about one-eighth the tensile strength and the compressive modulus is about one-half the tensile modulus (63). The tensile stress-strain curve for Kevlar® 49 is almost linear up to the breaking point. Kevlar® polymers are tough in tension because Kevlar® 49 fibers have a high work of fracture (a measure of the work required to propagate a crack through unit area of material).

One of the most attractive properties of advanced Kevlar® 49 fiber-epoxy composites is their high tensile strength. The simpliest model for the tensile failure of a unidirectional fiber composite loaded in the fiber direction is based upon the elasticity solution of uniform axial strain throughout the composite (64). Generally, the fibers have a lower strain to failure than the matrix, and composite fracture occurs at the failure strain of the fibers alone. This results in a rule of mixtures value for composite strength.

The problem with this approach is the variability of fiber strength which is characteristic of most high strength fibers. Under a tensile load, PPTA molecules in Kevlar® fibers may slip past one another or rupture at one of their longitudinal bonds causing neighboring molecules to become overloaded and fail. This gives rise to growing microcracks which eventually leads to broken fibers scattered throughout the composite. Therefore, the statistical variation in fiber failure results from a distribution of imperfections along the length of the fibers and by random molecular failure (64,65).

4.4 The Resin-Fiber Interface

The interface region in fiber reinforced composites is difficult to define and even more difficult to study. On a macroscale, it can be considered to consist of two surfaces and the region between these two surfaces. On a microscale, this region can be considered to consist of surface atoms and subsurface atoms. The number of

atomic layers below the surface atoms that influence the properties of the interface region is uncertain, as is the distance between atoms of the two surfaces. This distance may vary depending on chemical affinity between atoms, the steric requirements of the atoms or groups, and the mechanical restrictions placed on the interface due to cooldown of the composite after fabrication (66).

The establishment of an active fiber surface to achieve maximum adhesion between resin and fiber surface is a principle concern in the development of new reinforcing fibers for composites. A good adhesive must wet the adherent surface to obtain complete and intimite contact, must become viscous or solidify during the bonding stage, and must be able to deform during solidification to relieve internal stresses caused by thermal and cure shrinkage. The surface to be bonded must be easily wetted by the adhesive and be free of foreign particles. The condition required for wettability of the surface by the adhesive is that the surface energy must be greater than the adhesive surface energy. If is desirable to have a large interfacial area of contact whether the adhesive bond is due to van der Waals physical adsorption forces or to chemical bond formation (67).

The fiber-resin interface is the most sensitive region in a reinforced plastic. The physical and mechanical properties of the resin affect the properties of the interface. Epoxy resin near the interface has a tensile strength of 10,000 psi or higher. Theoretically, in a unidirectional reinforced resin composite, it should

be possible to obtain a transverse tensile strength as high as the resin strength. However, even if excellent interface bonding were present, the differences in the coefficient of expansion of the resin and fibers causes the interface to be in a state of stress. These stresses arise along the fiber axis in a composite because the higher coefficient of thermal expansion of the resin creates a tensile stress in the resin along the fiber axis and this induces a shear stress at the resin-fiber interface.

When the first fibers break in a unidirectional fiber composite subjected to a tensile load, perturbations of the stress field will result in the vicinity of the break, causing high fiber-matrix interface shear stresses. These shear stresses transfer the load around the break, and also introduce stress concentrations into adjacent unbroken fibers (64).

At each local fiber break, the stress in the vicinity of the broken fiber changes so that the axial stress in the fiber vanishes at the fiber break and gradually builds back up along the fiber length to its undisturbed stress value. The general form of the local stress pattern at a break is shown in Figure 4-2. The shear stress is a maximum close to the fiber break and decreases rapidly along the length of the fiber. As a result, the axial fiber stress builds up to its initial undisturbed value over a relatively short dimension.

This stress distribution may cause several possible failure events to occur. If the interface is weak, the shear stresses may

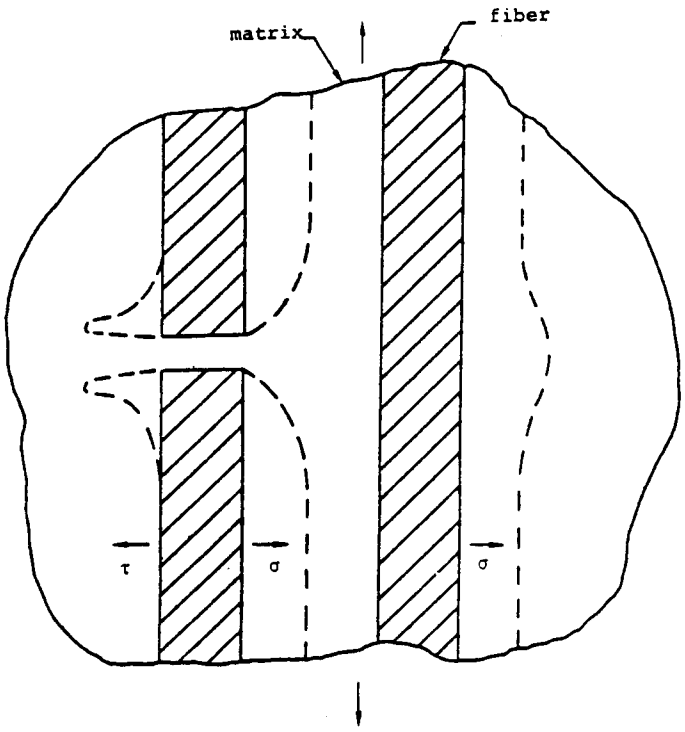

Figure 4-2. Perturbation of Stresses in the Vicinity of a Broken Fiber End (64).

cause an extensive crack propagation to progress along the interface. In this case, the strength of the composite material may differ only slightly from that for failure of a dry fiber bundle. This undesirable mode of failure can be prevented by a strong fiber-matrix interface or by use of a soft, ductile matrix which permits the redistribution of the high shear stresses. When the interface does not fail, the local stress concentrations may cause the fiber break to propagate through the matrix, to and through adjacent fibers. Alternately, the stress concentration in adjacent fibers may cause some of these fibers to break before the failure of the intermediate matrix. If a matrix crack or fiber breaks continue to propagate, the strength of the composite may be no greater than that of its weakest link. If the matrix and interface properties are of sufficient strength and toughness to prevent or stop these failure mechanisms, then continued load increases will produce new fiber failures at other locations in the material, resulting in an accumulation of dispersed internal damage as the loading continues. It can be expected that all of these effects will occur before material failure. In other words, the local fractures will propagate for some distance along and transverse to the fibers. These fractures will initiate and grow at various points within the composite. Increasing the load will produce a statistical accumulation of dispersed damage regions until a sufficient number of such regions interact to provide a weak surface, resulting in composite tensile failure (64).

For S-glass and graphite fibers, the shear carrying capacity of the fibers greatly exceeds that of the matrix or fiber-matrix interface. Thus failure in the fibers is primarily governed by the fiber tension and these fibers fail approximately perpendicular to the fiber axis. However, in Kevlar® 49 the shear strength of the fiber can be less than that of the matrix. Thus the fiber may fail by a combination of longitudinal splitting and transverse crack propagation (44). The ability of the fiber-matrix strand to support high tensile loads is strongly influenced not only by the shear carrying capability of the matrix but also by the ability of the individual Kevlar® 49 fibers to sustain high tensile loads in the presence of high shear tractions on the fiber surface generated by neighboring fiber breaks.

CHAPTER 5

EXPERIMENTAL PROCEDURES

5.1 Materials

Raw materials used in the experimental evaluations include an epoxy resin, curing agent, and four types of fiber reinforcements.

5.1.1 Epoxy resin. The epoxy resin chosen for this work was D.E.R. 332 from Dow Chemical Company. D.E.R 332 is a highly purified diglycidyl ether of bisphenol A. It is water-white in color, has an average molecular weight of 340-350, and an epoxide equivalent of 173-179 (24). The viscosity is in the range of 4000-6400 centipoises at 25°C (22). The pure diglycidyl ether of bisphenol A is a solid at room temperature (melting point 43°C). Due to the high purity of D.E.R. 332, the liquid resin tends to crystallize at room temperature. To keep the resin in liquid form and to reduce the viscosity to a workable range, the epoxy was heated to 70°C before the addition of a curing agent.

5.1.2 Curing agent. The curing agent chosen for this work was Jeffamine® T-403 from Texaco Chemical Company. Jeffamine® T-403 is an aliphatic polyether triamine (polyoxypropyleneamine).

5.1.3 Fiber reinforcements. Four types of fiber reinforcements were used in this research. They consisted of a pitch-based graphite fiber, a high modulus PAN-based graphite fiber, a low modulus PAN-based

graphite fiber, and a polyamide fiber (Kevlar® 49). All fibers were used in the as received condition.

Thornel® Type P-55 grade VSB-16 manufactured by Union Carbide Corporation was selected as the pitch-based graphite fiber to be studied. The strand consists of four thousand round filaments with a diameter of 11 microns. The fiber density is 2.0 g/cm^3. The fibers are treated to improve interlaminar shear strength and sized with an epoxy compatible sizing.

Magnamite® HMS graphite fiber manufactured by Hercules was chosen as the high modulus PAN-based graphite fiber. The carbon content of the fiber is 99.7%. The strand consists of twelve thousand round filaments with a diameter of 8 microns. The fiber density is 1.83 g/cm^3. The fiber has been treated to improve its interlaminar shear properties.

Magnamite® AS4 graphite fiber manufactured by Hercules was chosen as the low modulus PAN-based graphite fiber. The carbon content of the fiber is 94.0%. The strand consists of twelve thousand round filaments with a diameter of 8 microns. The fiber density is 1.80 g/cm^3. The fiber has been treated to improve its interlaminar shear properties.

The Kevlar® 49 fibers were manufactured by E.I. du Pont de Nemours and Co. The 380 denier fiber contained 267 filaments in the strand. The fiber diameter is about 12 microns and the fiber density is about 1.45 g/cm^3.

5.2 Preparation of Epoxy and Composite Samples

Kevlar® 49 fibers were uniaxially wound around the base of an aluminum mold, which had been sprayed with MS-122 release agent from Miller-Stephenson Chemical Co. An aluminum frame was secured by screws around the edge of the mold. The epoxy resin was heated to 70°C and mixed with the curing agent using a glass stirring rod until the curing agent was evenly distributed in the mixture. Three levels of amine content were used: 1) 47 pph amine content is the stoichiometric ratio, 2) 32.5 pph amine content gives a cured epoxy with a maximum macroscopic yield stress, and 3) 25 pph amine content gives a cured epoxy with a 70-80% ultimate strain. The epoxy resin was poured over the fibers to a depth of approximately 1 mm. The mold was placed in a vacuum chamber and allowed to degas for one hour. The epoxy composites were cured at room temperature for 24 hours and then placed in a compression molding machine for 16 hours at 85°C. After allowing the epoxy composites to slowly cool to room temperature, the sheet was demolded. Coupons of unreinforced epoxy and the Kevlar® 49/epoxy composites were cut from the sheet using a band saw. The edges were sanded smooth and then polished using 00 sandpaper.

5.3 Density Measurements

The densities of the epoxy and composite samples were measured following procedures described in ASTM D 792-66 and ASTM D 1505-68. For the density gradient technique, a water-sodium bromide system

with a density range of 1.145 g/cm^3 to 1.8 g/cm^3 was used. The samples were placed in the column for 24 hours. The position of the samples were compared to the positions of the standard beads of known specific gravity. The apparent volume fraction of fibers in the composite was calculated from the equation

$$V_f = \frac{d_c - d_m}{d_f - d_m} \tag{5-1}$$

where d_c is the density of the composite, d_m is the density of the matrix, and d_f is the density of the fibers.

5.4 Mechanical Property Testing

The stress-strain behavior of the unreinforced epoxy and the Kevlar® 49 fiber reinforced composite under a tensile load was measured using a floor model Instron Tensile Tester. The strain, ε, on the sample was determined from the equation

$$\varepsilon = \frac{\Delta L}{L_o} = \frac{\text{(cross head speed) X (chart distance)}}{\text{(chart speed) X } L_o} \tag{5-2}$$

where L_o is the original gauge length of the specimen. The ultimate tensile strength, σ, was calculated from the expression

$$\sigma = \frac{F}{A_o} \tag{5-3}$$

where F is the force at break and A_o is the original cross sectional area. Young's modulus, E, is given by the equation

$$E = \frac{\sigma}{\varepsilon} \tag{5-4}$$

and was calculated from the initial slope of the force-elongation curve.

The samples were tested with a gauge length of one inch, cross-head speed of 0.02 in./min., and chart speed of 1 in./min. Three samples were tested for each case.

5.5 Gas Plasma Techniques

Plasma etching depends upon the chemical combination of the solid surface to be etched, with an active gaseous species produced in a discharge. There are three types of discharges: 1) AC; 2) DC; and 3) RF. The Plasma Prep II Model 11005 manufactured by SPI Supplies uses a radio frequency (RF) discharge. The RF discharge has the ability to ion bombard the insulating surface on the electrode almost continuously, this makes the target positive for only a very short fraction of each cycle. This makes the RF discharge more efficient than the other discharges in promoting ionization and sustaining the discharge.

The technique of plasma etching was first applied in the 1960s for the removal of photoresist material which consists of essentially carbon and hydrogen (63). Solid carbon is converted to gaseous carbon monoxide and carbon dioxide by oxidation in an oxygen discharge. These gases, along with other products of the reaction, such as water vapor, are removed by the vacuum system. The purpose of the glow discharge is to convert molecular oxygen into active oxygen which reacts readily with organic materials at room temperature.

The Kevlar® 49 fibers were placed in the sample chamber of the Plasma Prep II. A vacuum was applied to the sample chamber. The radio frequency was tuned to the lowest point on the meter (13.56 MHz). Oxygen was fed into the sample chamber at a pressure of 5 psi. The Kevlar® 49 fibers were etched for 5, 10, 15, and 20 minute intervals.

5.6 Scanning Electron Microscopy (SEM)

An ARM model 900 high resolution scanning electron microscope was used to study the effect of plasma etching on Kevlar® 49 fibers and to study the fracture surfaces of the epoxy and composite samples. The plasma etched Kevlar® 49 fibers were mounted on aluminum sample holders with double stick tape. The fractured epoxies and composites were cut near the fracture surface and were mounted on the sample holder with the fractured surface on top using an epoxy glue. After the samples were mounted, they were then sputter-coated with gold-palladium in a vacuum chamber.

5.7 Wide Angle X-Ray Scattering

Qualitative wide angle x-ray diffraction patterns for the fibers used in this research were obtained using a Philips Norelco X-ray Generator and a Statton camera. The radiation used was copper $K\alpha$ (wavelength 1.542 $\mathring{A}$) and the x-ray generator was operated at 30 Kv and 20 mA. Pinhole collimation of the x-ray beam was used and the film cassette was placed in the 3 cm position. The film patterns

were obtained with the fibers perpendicular to the x-ray beam and with the x-ray beam directed into the fiber axis. The exposure times were varied from 4 to 6 hours among the different fiber samples.

5.8 Small Angle X-Ray Scattering (SAXS)

The 10 meter small angle x-ray scattering facility of the National Center for Small Angle Scattering Research at the Oak Ridge National Laboratory was used to quantitatively measure intensity profiles and integrated intensities which allowed the measurement of void shape and size distribution as well as void volume fraction. A schematic diagram of the SAXS equipment is shown in Figure 5-1.

5.8.1 The SAXS equipment. The x-ray generator is a 6.0 kilowatt Rigaku-Denki rotating anode type. The copper anode emits x-rays which are separated into the $K\alpha$ and $K\beta$ components by a pyrolytic graphite monochromator. The collimation of the x-ray beam is achieved by two pinholes with a one millimeter square opening and separated by a distance of 1.6 meters. By using pinhole collimation, the scattered intensity data does not have to be corrected for smearing. The angle of the x-ray generator with respect to the collimator is fixed so that copper $K\alpha$ radiation (λ = 1.54 Å) is used. When the generator is operated at 40 Kv and 40 mA in this arrangement, the intensity of the incident x-ray beam can be as high as 2.5×10^6 photons per square millimeter per second. In order to minimize the scattering from air, the entire path of the x-ray beam is maintained under vacuum.

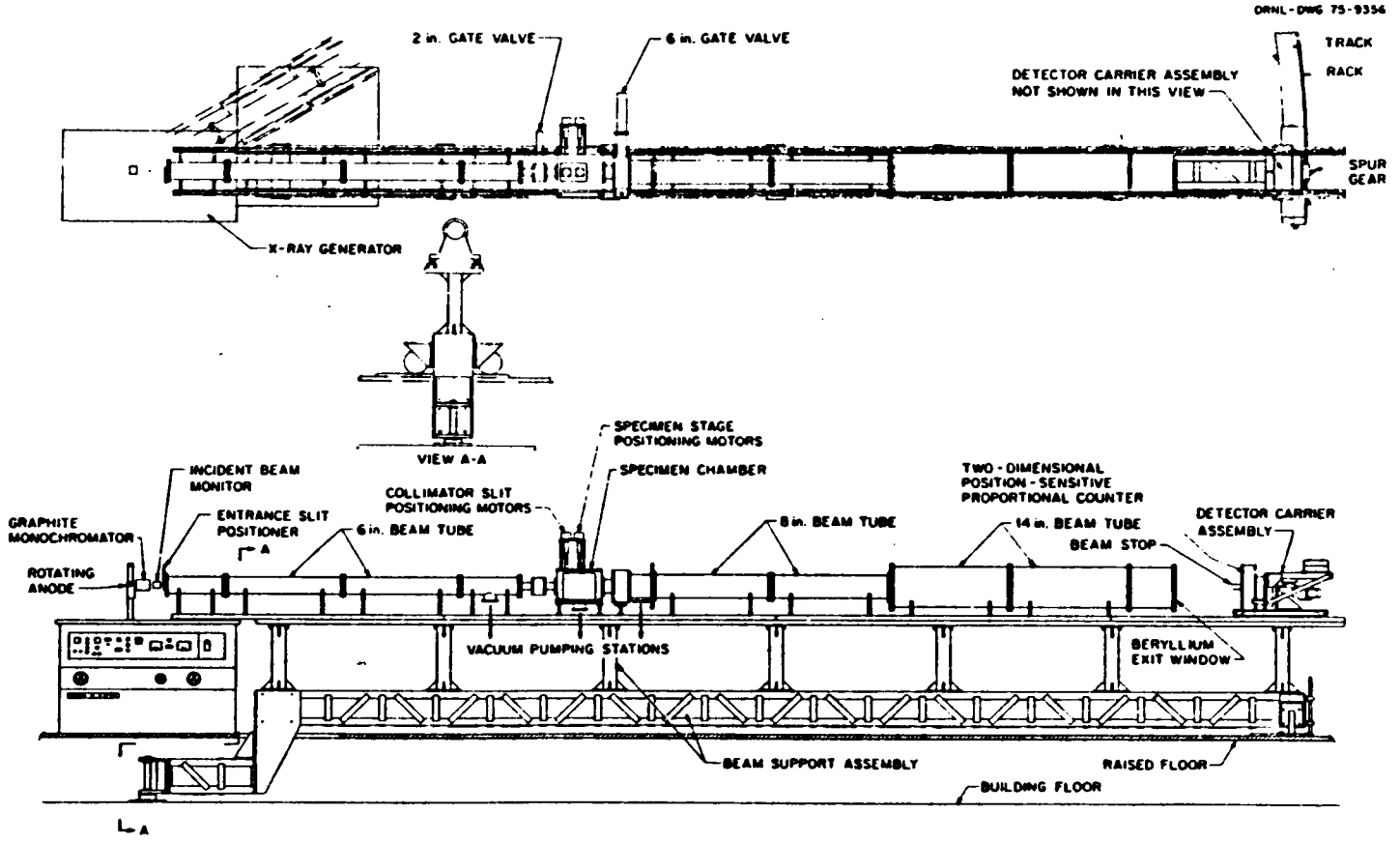

Figure 5-1. A Schematic Diagram of the Small Angle X-Ray Scattering Equipment at the Oak Ridge National Laboratory.

The sample chamber consists of a 30 x 30 x 35 cm chamber containing externally operated x-y positioning motors for the specimen stage. For making multiple runs of solid samples, a sample wheel with twelve sample holes may be used. The samples on the wheel are moved into the x-ray beam by a stepping motor which is in turn manipulated by computer software. Also in the sample chamber is a carbon-filled polyethylene specimen which can be moved into the incident beam by the use of a motor equipped with an eccentric cam. The glassy carbon is used to determine the transmission coefficient of the sample.

The detector, which monitors scattered intensity, is a two-dimensional position-sensitive proportional counter. The detector consists of a grid of meshed resistance wires. The grid is divided into 64 x 64 channels each of the size 0.324 x 0.324 cm. The intensity measured by the detector is position encoded and stored in the computer memory. Therefore, a 64 x 64 matrix of scattered intensity in two dimensions exists for each sample. The sample to detector distance can be varied from one to five meters, thus allowing the angular range and resolution to be controlled.

5.8.2 SAXS correction runs. Due partly to the reflection off the second pinhole collimator and partly to other slit scattering, a background intensity is present in the scattering pattern. The background pattern appears as a cross around the beamstop. To correct for this background scattering, a run is carried out either with nothing in the beam or with an empty sample cell if the sample is a liquid or powder.

The dark current correction refers to radiation from the environment, i.e. cosmic radiation and electronic noise, that is registered by the detector. The dark current run is normally performed with both gate valves A and B on the SAXS equipment closed. This prevents x-rays from the generator to reach the detector. Both background and dark current runs are measured for a long time (over 1000 seconds) to achieve better counting statistics.

A detector sensitivity run is performed to correct for the possible nonuniform detecting efficiency of the detector. To do this, a radioactive isotope Fe-55 is placed in the sample chamber with gate valve A closed. For a better assessment of sensitivity, a run time of several hours is required.

After these correction runs have been made, they are subtracted from each sample run using the computer program BKC.

5.8.3 Absolute intensity measurement. In order to make quantitative calculations, such as the number of scattering centers and void volume fraction, the absolute intensity is required. The absolute intensity is defined as the ratio of the scattered intensity to that of the primary beam. The intensity of the primary beam is defined as the rate of photon bombardment per cross sectional area of the sample in a given time. Two of the most common methods of calculating the absolute intensity are by means of filters or by reference to a standard sample.

For radiation from a copper-target tube, calibrated nickel filters were used as attenuators. The nickel foils are placed in the x-ray beam in the sample chamber. The beamstop is removed and the detector is used to measure the intensity. This is done for several thicknesses of the nickel foil. The transmitted intensity is corrected for the dark current and the dead time of the detector by the equation

$$I_t = \frac{I_{obs} - I_{dc}}{1 - [(I_{obs} - I_{dc})\tau]} \qquad (5\text{-}5)$$

where I_t is the true transmitted intensity, I_{obs} is the measured intensity, I_{dc} is the dark current intensity, and τ is the dead time associated with the detection system (7×10^{-6} sec.). The transmitted intensity is plotted versus nickel thickness on a semi-logarithmic scale. The intensity value extrapolated at zero nickel thickness is the absolute intensity of the primary beam. Now the equation

$$I_t = I_o[\exp(-\mu t)] \qquad (5\text{-}6)$$

can be used to confirm the value for the intensity of the primary beam. I_o is the incident beam intensity, μ is the linear absorption coefficient of nickel and t is the thickness of nickel foil.

Once the absolute intensity has been determined, the scattering from a standard sample is used to calculate the absolute intensity at any time by a comparative measurement. Lupolen, a stable heat treated polyethylene, is used as a standard sample. The SAXS pattern

for Lupolen is an isotropic halo whose quantitative features vary only with the primary beam power. To measure the absolute intensity by this method, the radial average around the beamstop of the Lupolen scattering pattern is analyzed by recording the intensity at a specified angle (2θ = 0.0103 rad) where the scattered intensity is linear. By taking the ratio of the Lupolen intensity at two different times, and multiplying by the absolute intensity obtained by the direct method, the absolute intensity can be calculated. This method works best only when small variations of absolute intensity are present.

5.8.4 Collection and reduction of SAXS data. Before the actual sample run is made, the transmission coefficient of the sample must be measured. The transmission coefficient is a function of the sample thickness, absorption coefficient and mass density. The transmission coefficient may be calculated by the equation

$$T_m = \frac{I_{csam} - 0.70\, I_{sam}}{I_c} \qquad (5\text{-}7)$$

where T_m is the transmission coefficient of the sample, I_{csam} is the scattered intensity with the glassy carbon and the sample in the beam, I_{sam} is the scattered intensity of the sample alone, and I_c is the scattered intensity of the glassy carbon. The factor 0.70 is the transmission coefficient of the glassy carbon itself.

Now the actual sample run can be made. The owner's ID, the transmission coefficient of the sample, the sample thickness, the title of the sample run, and the run time are entered into the header

record for the sample run. After the run time has been completed, the information is saved and a sequence number is assigned to the sample run.

To analyze the sample run, the computer program FILE is executed. This program is designed to fetch and store two-dimensional data from disk storage to working memory. At this point, the SAXS correction runs discussed in section 5.8.2 are subtracted from the sample run using the program BKC. Two-dimensional contour plots of the corrected sample run are generated by the computer using the program CON. These contour plots are useful for qualitative comparison of the data with respect to the variables of interest.

A subroutine of the CON program, CEN, will establish the center of the contour plot and store that position in the header record. To help quantify the data, the two-dimensional data can be reduced to one-dimensional form by using the subroutines RAD and AVE. For isotropic scattering patterns, RAD is used to perform a radial average around the beamstop. AVE will calculate averaged intensity slices of specified azimuthal angles. Since the contour patterns obtained from the reinforcing fibers used in the research are highly anisotropic, AVE was used to plot the intensity versus scattering angle for $\emptyset$ = 0 and 90 degrees.

The program VUE uses the one-dimensional data to make various plots. The Guinier plot, ln I versus h^2, was made and a linear fit was made to the slope at small values of h^2. From this procedure,

an average dimension of the scattering centers in each major axis may be obtained.

The program INVAR was used to perform the invariant analysis for the background corrected anisotropic scattering data. This program uses the absolute intensity measurement to calculate the total integrated intensity and the mean square electron density fluctuation. From this information the void volume fraction in the material can be determined.

CHAPTER 6

EXPERIMENTAL RESULTS AND DISCUSSION

6.1 SAXS Analysis of Kevlar® 49 Fibers

The Kevlar® 49 fibers were aligned on a sample holder and placed in the x-ray beam of the SAXS equipment with the fiber axis perpendicular to the beam. The two-dimensional isointensity contour plots of the scattered intensity were obtained with the shortest sample to detector distance (1.126 m) and with the longest sample to detector distance (5.126 m). Figure 6-1 and Figure 6-2 show the contour plots from the short and long geometries, respectively. The scattering pattern is anisotropic with intense scattering in the equatorial direction. Figure 6-3 compares the variation of intensity with scattering angle in the equatorial and meridional directions of the combined scattering data on the absolute intensity scale. The intense SAXS intensity from the Kevlar® 49 fibers suggests that the electron density difference between the two phases is large. This is the case when there is a system of microvoids present in the solid material.

From the SAXS contour patterns of Kevlar® 49 fibers, the voids appear to have an ellipsoidal shape with a preferred orientation of the long axis parallel to the fiber axis. The Guinier plots from an equatorial and meridional slice of the combined scattering data are shown in Figure 6-4. The mean void size detected by SAXS was

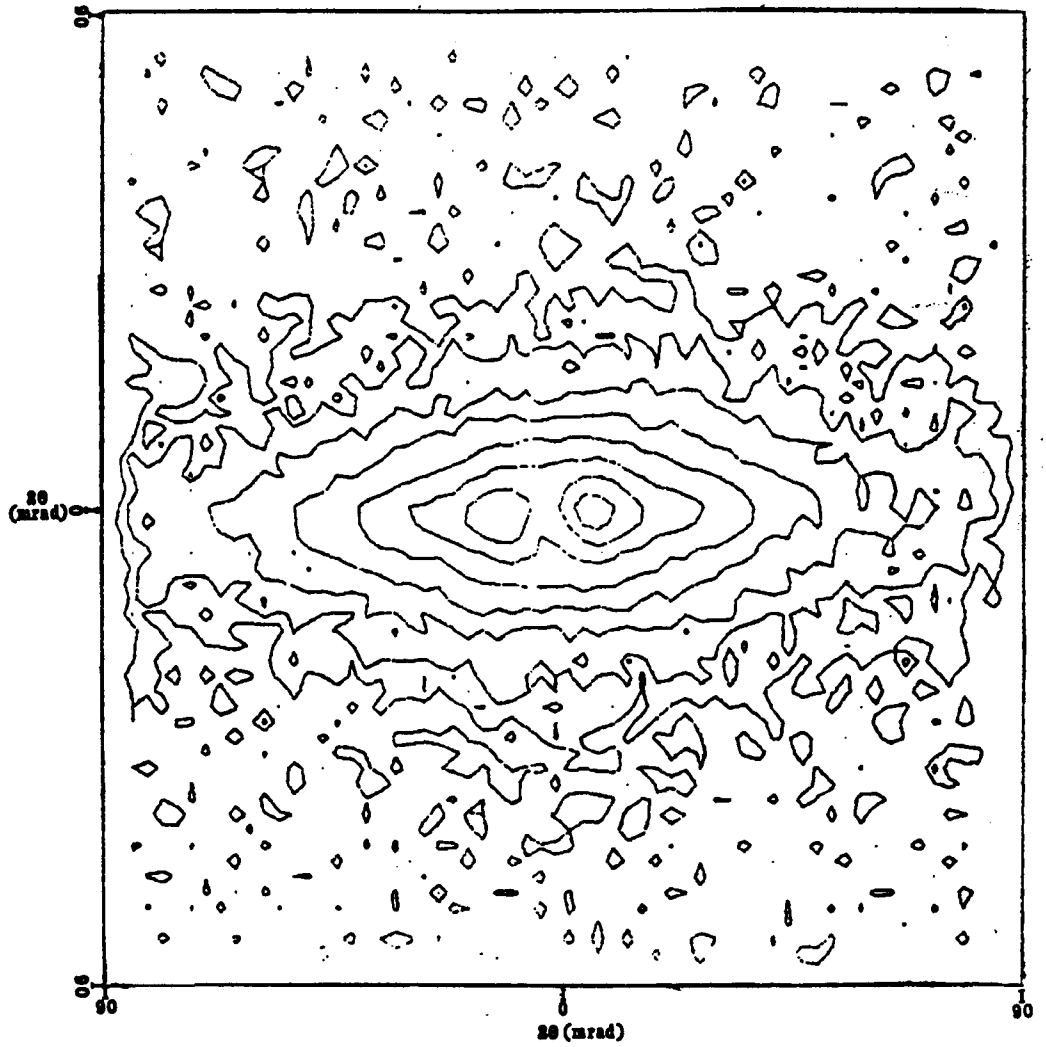

Figure 6-1. Two-Dimensional Isointensity Contour Plot of Kevlar® 49 Fibers from the Short Geometry.

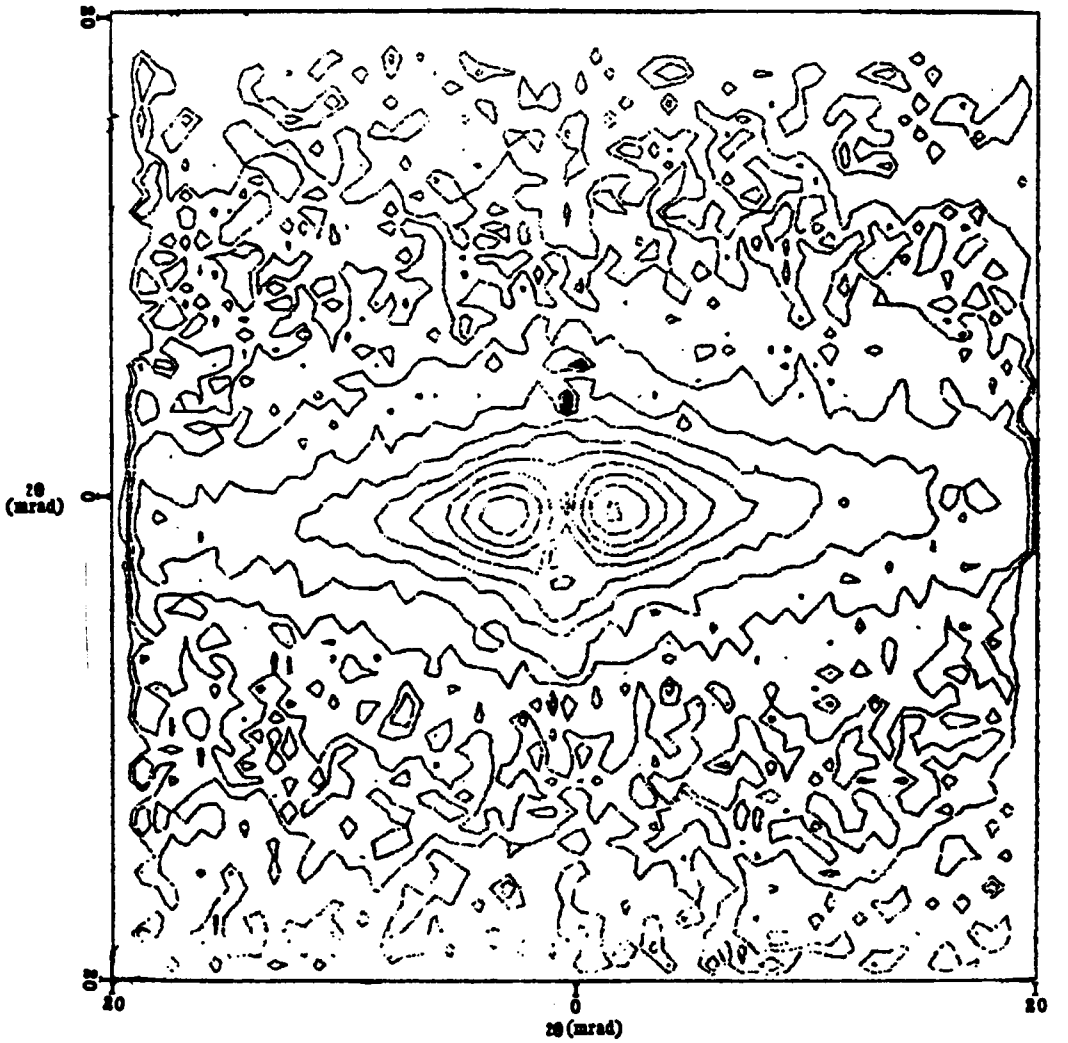

Figure 6-2. Two-Dimensional Isointensity Contour Plot of Kevlar® 49 Fibers from the Long Geometry.

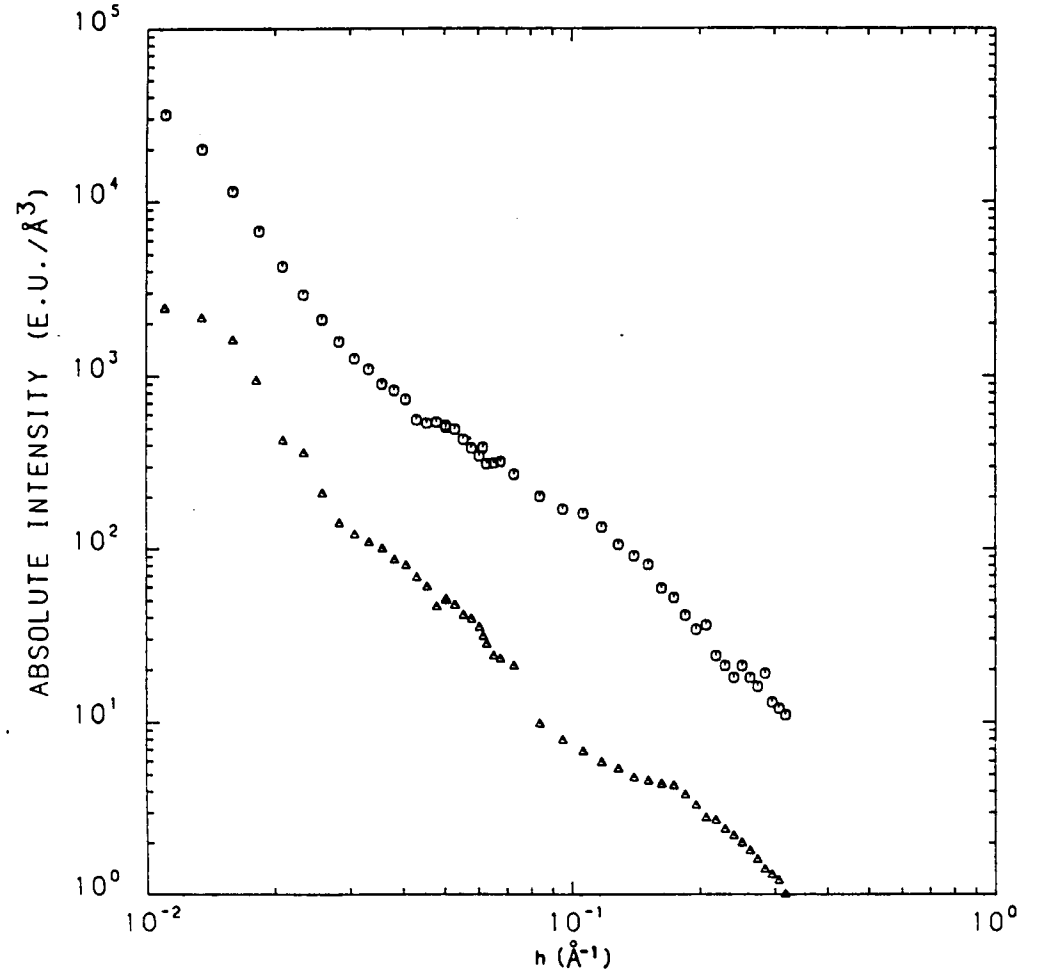

Figure 6-3. Absolute Scattering Intensity Variation with Scattering Vector for Kevlar® 49 Fiber. o Equatorial, Δ Meridional Slice.

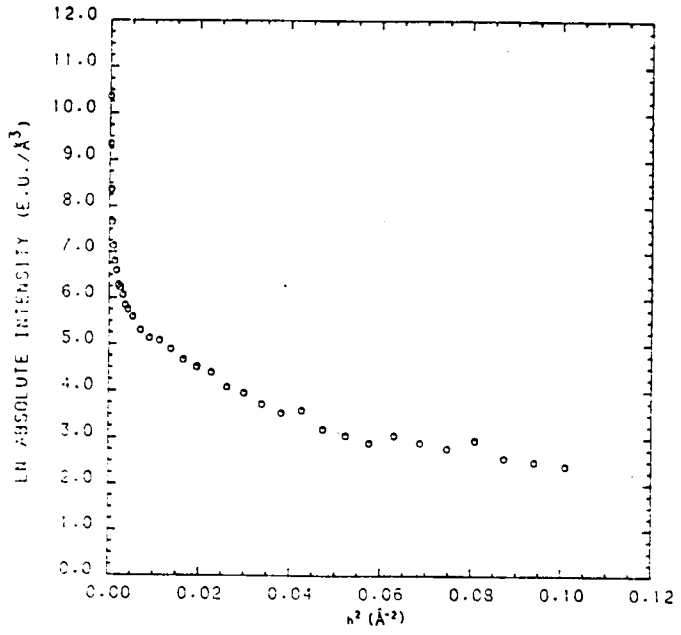

(a)

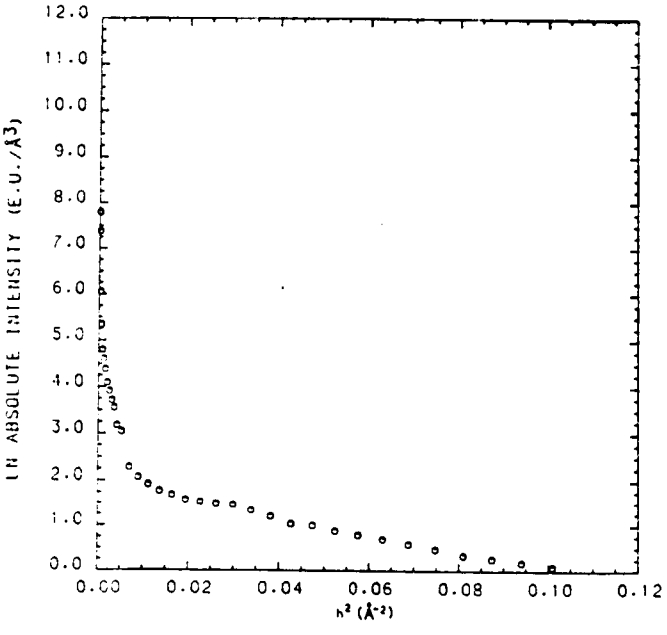

(b)

Figure 6-4. Guinier Plots of the Combined Scattering Data for Kevlar® 49 Fiber. (a) Equatorial Slice; (b) Meridional Slice.

calculated using the Guinier approximation in the low angle region. The void width was determined to be 35 nm and the void length was 40 nm. The Guinier plot was not linear over the entire scattering region. This indicated that there was a distribution of void sizes. Since the slope of the Guinier plot is proportional to the square of the radius, the contribution of the larger microvoids towards the x-ray scattering profile would be greater, thus the calculated radius would tend to be larger than the arithmetic mean. Using the method of Jellinek et al. (83), the scattering data was analyzed and the dimensions of the void distribution are presented in Table 6-1.

Table 6-1. Microvoid Size Distribution in Kevlar® 49 Fibers

Width (nm)	Volume (%)	Length (nm)	Volume (%)
7.4	1.7	6.5	0.8
22.0	8.3	20.0	7.5
40.0	90.0	49.0	91.7

6.1.1 Microvoid accessibility to diffusing liquids. To determine the accessibility of the microvoid system to a diffusing liquid, the Kevlar® 49 fibers were soaked in glycerin under vacuum, then

the SAXS pattern was obtained. Glycerin was chosen as the diffusing liquid because it is a relatively low viscosity liquid with an electron density near that of the Kevlar® 49 fibers. Figure 6-5 shows the SAXS contour pattern for the glycerin soaked Kevlar® 49 fiber. The absolute intensity versus the scattering vector is presented in Figure 6-6. The equatorial intensity from the scatterers is significantly reduced in the glycerin soaked fiber, especially in the region around the beamstop associated with the largest voids. This indicates that the glycerin was able to diffuse into the larger microvoids. This is in agreement with the work of Dobb et al. (46) and Lee (82).

6.1.2 Plasma etching of Kevlar® 49 fibers. In order to determine the location of voids throughout the fiber diameter, plasma etching of the fibers was used to remove the skin from the core of the fiber. A series of scanning electron micrographs was made for the Kevlar® 49 fibers before and after being exposed to the plasma for various periods of time. Figure 6-7 shows the SEM micrograph of Kevlar® 49 fibers before plasma etching. After five minutes of plasma etching, Figure 6-8 shows the effect of plasma etching on the surface of the fiber. In Figure 6-9, a few small areas can be seen where parts of the original skin layer still remain after ten minutes of plasma etching.

After fifteen minutes, the plasma has removed most of the skin from the core of the fiber as seen in Figure 6-10. An interesting feature of this micrograph is in the region where the fibers

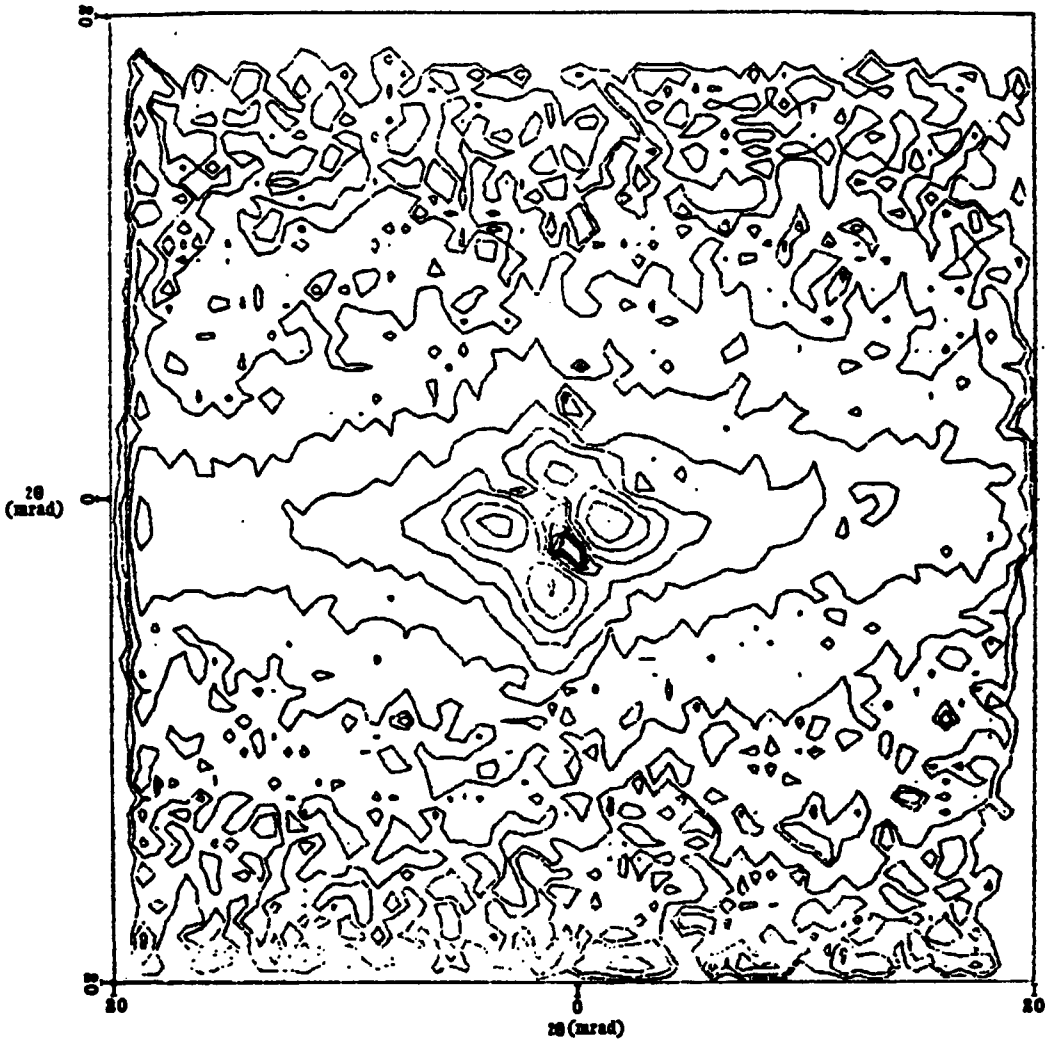

Figure 6-5. Two-Dimensional Isointensity Contour Plot of Glycerin Soaked Kevlar® 49 Fiber from the Long Geometry.

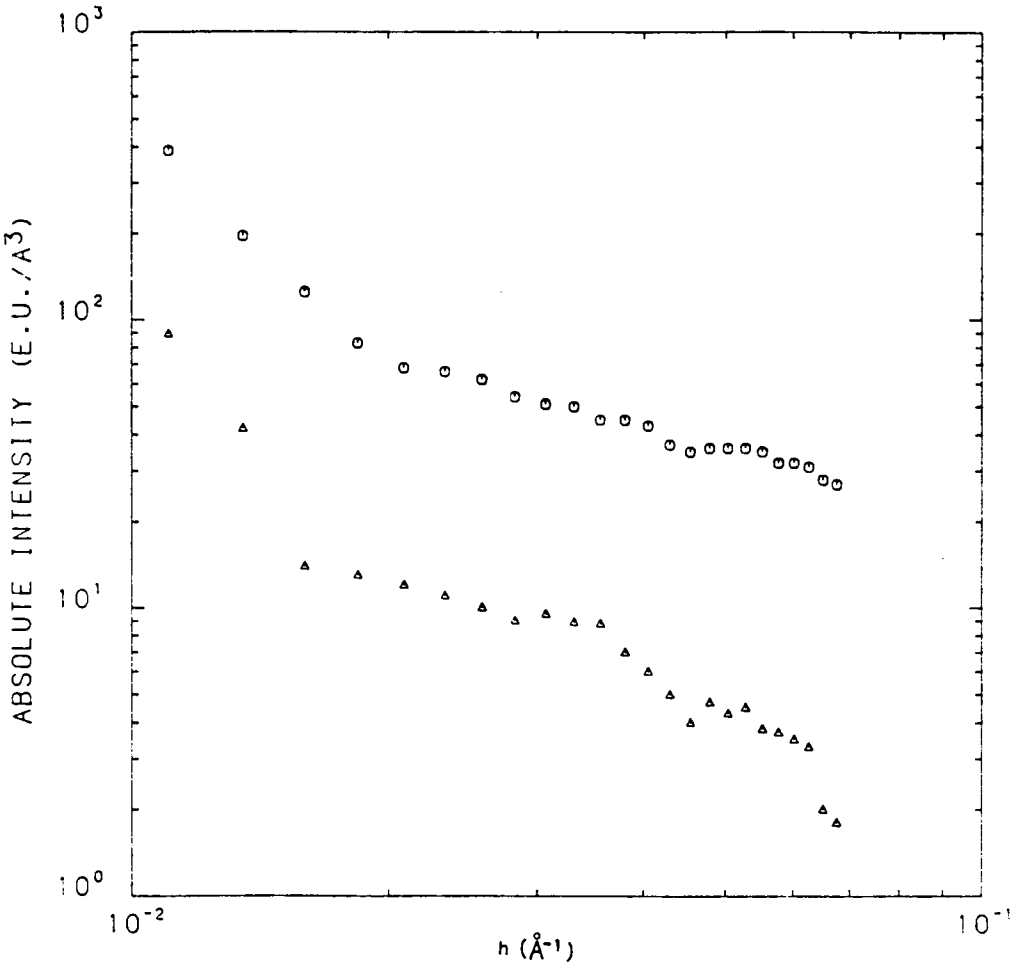

Figure 6-6. Absolute Scattering Intensity Variation with Scattering Vector for Glycerin Soaked Kevlar® 49 Fiber. o Equatorial Slice, Δ Meridional Slice.

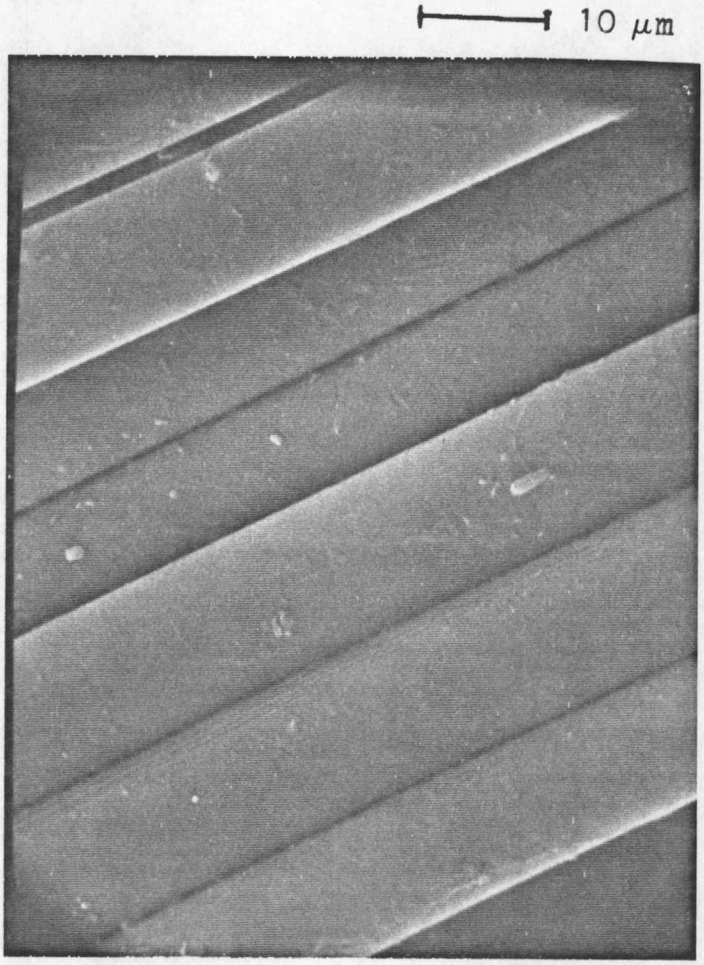

Figure 6-7. SEM Micrograph of Kevlar® 49 Fiber.

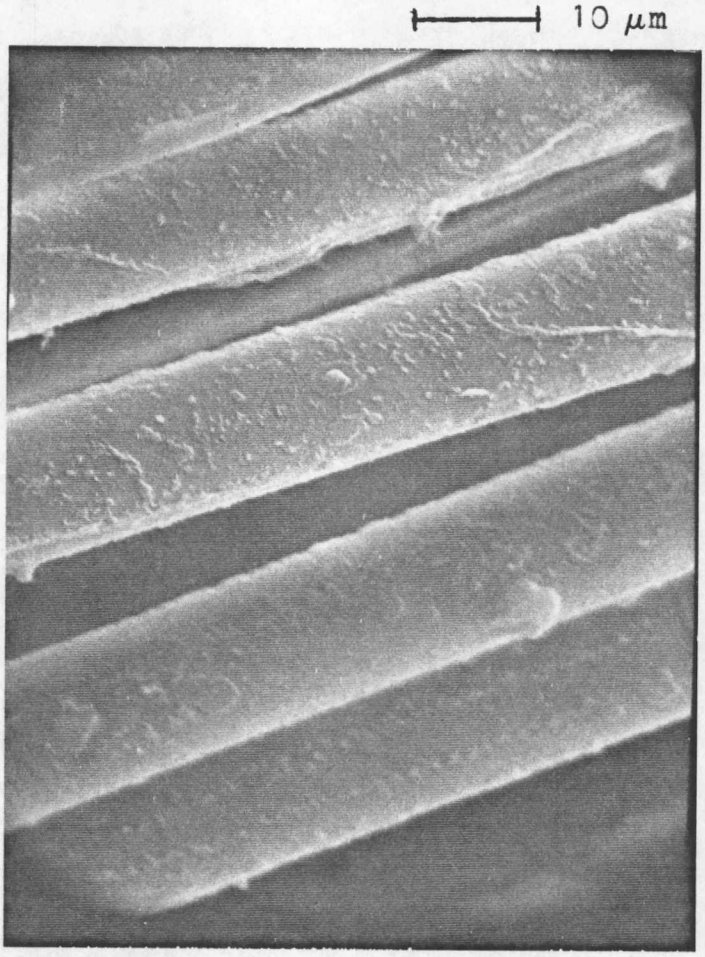

Figure 6-8. SEM Micrograph of Kevlar® 49 Fiber Plasma Etched for 5 Minutes.

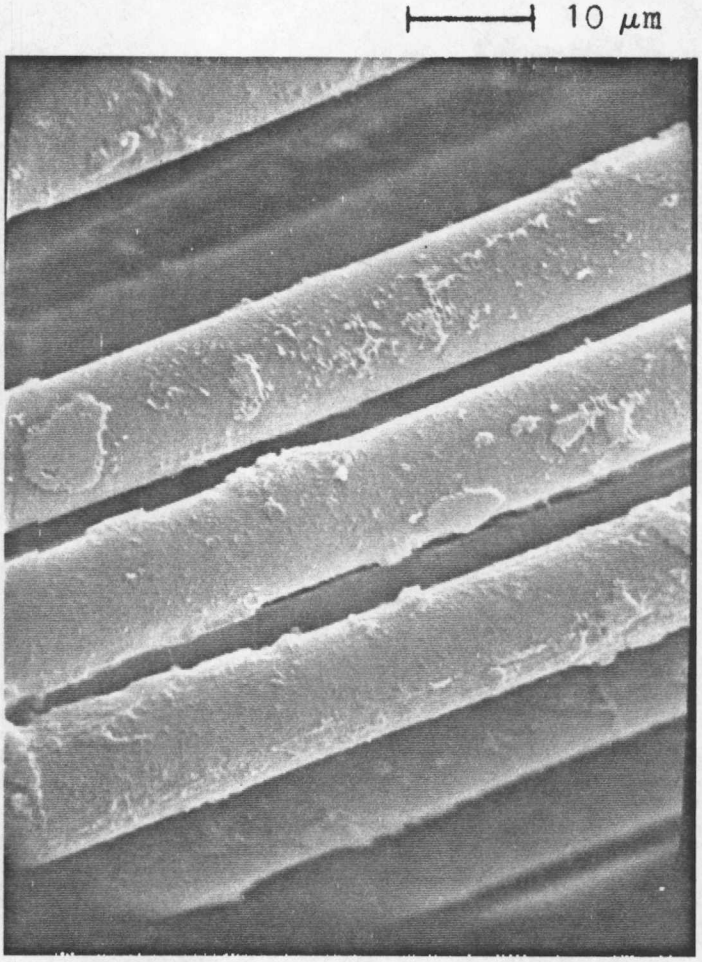

Figure 6-9. SEM Micrograph of Kevlar® 49 Fiber Plasma Etched for 10 Minutes.

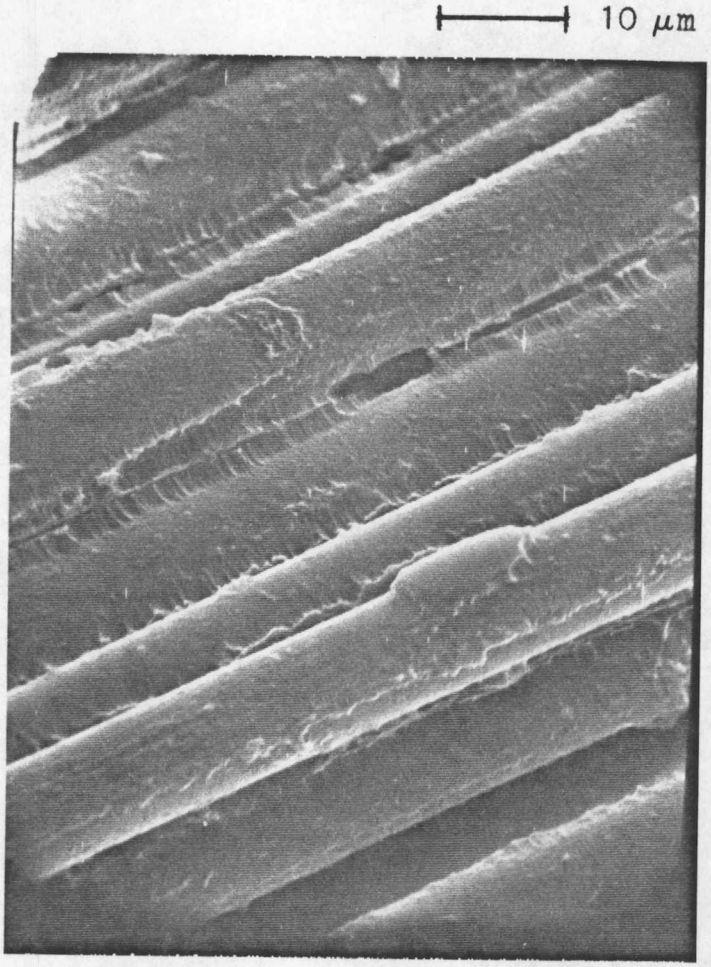

Figure 6-10. SEM Micrograph of Kevlar® 49 Fiber Plasma Etched for 15 Minutes.

are in contact with one another. This area has been somewhat protected from the plasma. There is a distinct morphological difference between the outer surface of the fiber and the core. The skin shows an approximately 500 nm periodic banding along the fiber axis. This supports evidence obtained by Dobb et al. (42) from electron diffraction and electron microscope dark-field image techniques that Kevlar® 49 fibers consist of a radial system of pleated sheets. Dobb recognized the possibility of a skin-core heterogeneity and this micrograph indicates that this is the case.

After twenty minutes, only remnants of the skin layer remain as seen in Figure 6-11. From these SEM micrographs, it was determined that unetched Kevlar® 49 fibers have a diameter in the 11-12 μm range and from the micrographs of the etched fibers the thickness of the skin is 1-2 μm.

Kevlar® 49 fibers were embedded in an epoxy resin. The composite was cut to expose the fiber ends and plasma etched for one hour. The resulting SEM micrograph is shown in Figure 6-12. The skin layer of the fiber protruding out of the epoxy matrix has been etched away. There has been an increased effect of the plasma on the central part of the fiber core in a majority of the fibers in the sample.

6.1.3 SAXS analysis of plasma etched fibers. The SAXS contour plots taken for the plasma etched Kevlar® 49 fibers in the short geometry appear unchanged from the unetched fibers, regardless of

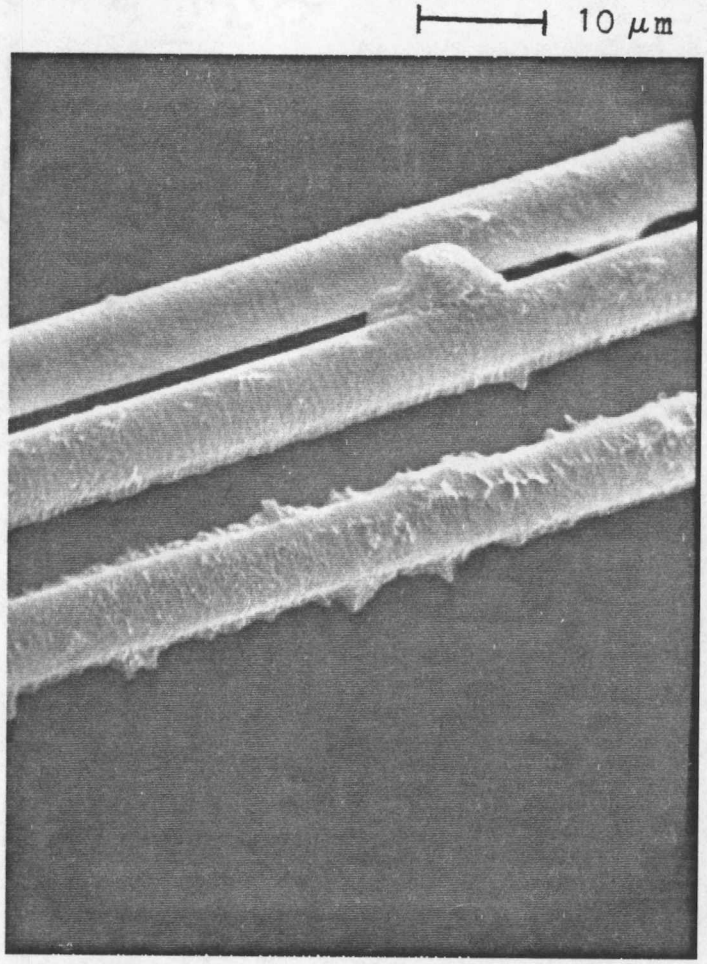

Figure 6-11. SEM Micrograph of Kevlar® 49 Fiber Plasma Etched for 20 Minutes.

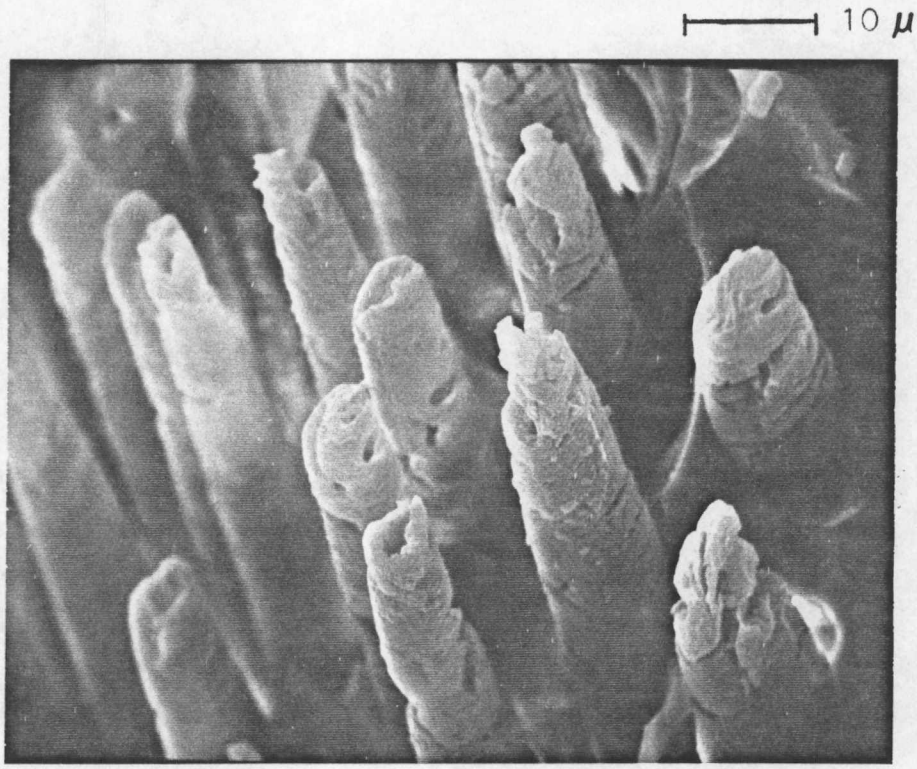

Figure 6-12. SEM Micrograph of Plasma Etched Kevlar® 49 Fiber Ends.

the amount of etching. The contour plots are illustrated in Figure 6-13. In the long geometry, however, there is an observable change in the scattering pattern for all of the etched fiber samples when compared with the unetched sample. These SAXS contour patterns are represented in Figure 6-14. The void dimensions of the etched fibers from the Guinier analysis of both the short and long geometries are given in Table 6-2.

The void dimensions in the short geometry are the same in all cases. In the long geometry, the void width increases and the void length apparently decreases with etch time. The decrease in void length may be explained due to the largest voids scattering near the beamstop. When the void length increases due to plasma etching, the scattering then moves into the beamstop. The volume fraction of voids determined by invariant analysis is plotted versus etch time in Figure 6-15 along with the decrease in fiber diameter observed from the SEM micrographs. The void fraction initially increases after plasma etching, then remains constant until the plasma has etched away most of the skin then another increase in the void volume fraction is observed.

6.1.4 Models of void distribution in Kevlar® 49 fibers. Dobb et al. (46) measured void dimensions in Kevlar® 49 fibers by means of small angle x-ray scattering. Water was used to reduce the intensity of the equatorial scatterers. This was an indication that the pore system was open to the fiber surface. From transmission electron

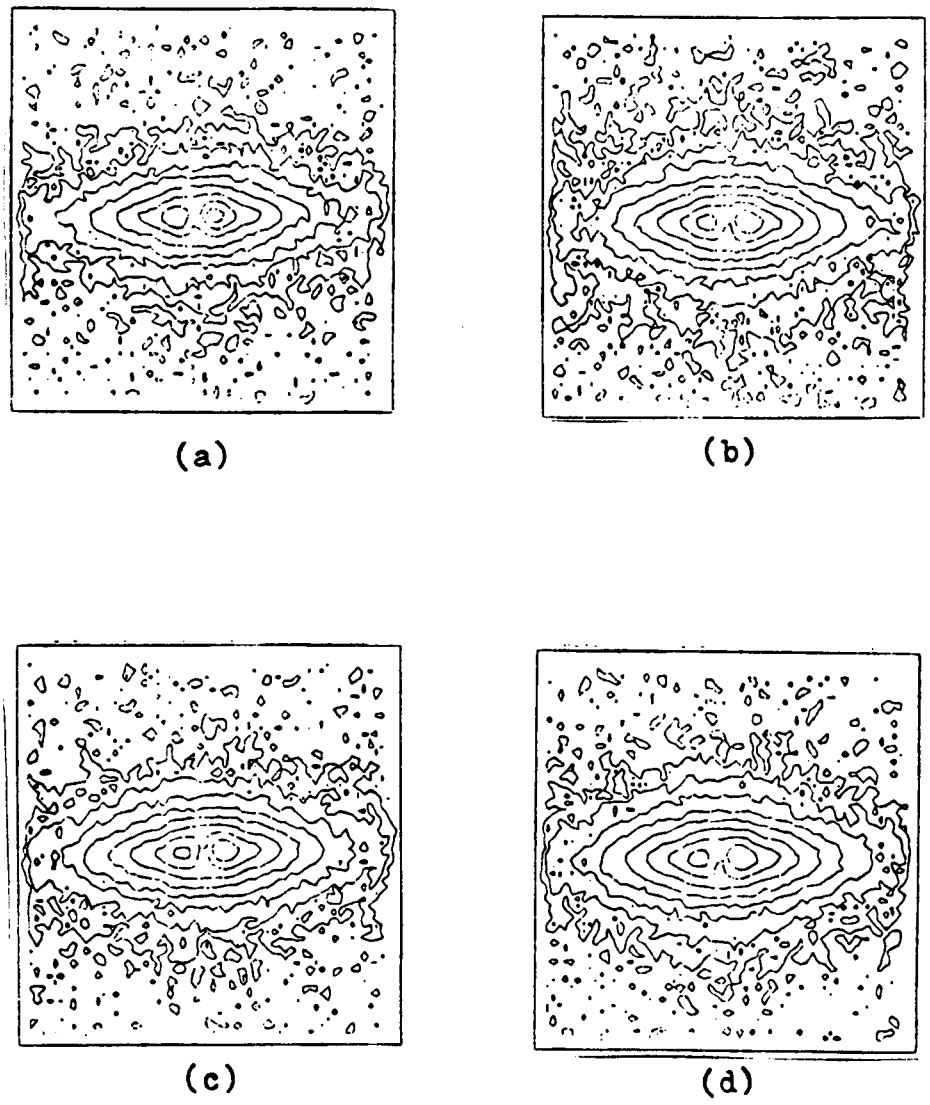

Figure 6-13. SAXS Contour Plots of Kevlar® 49 Fibers in the Short Geometry. (a) Unetched Fiber; (b) Etch Time 5 Min.; (c) Etch Time 10 Min.; (d) Etch Time 15 Min.

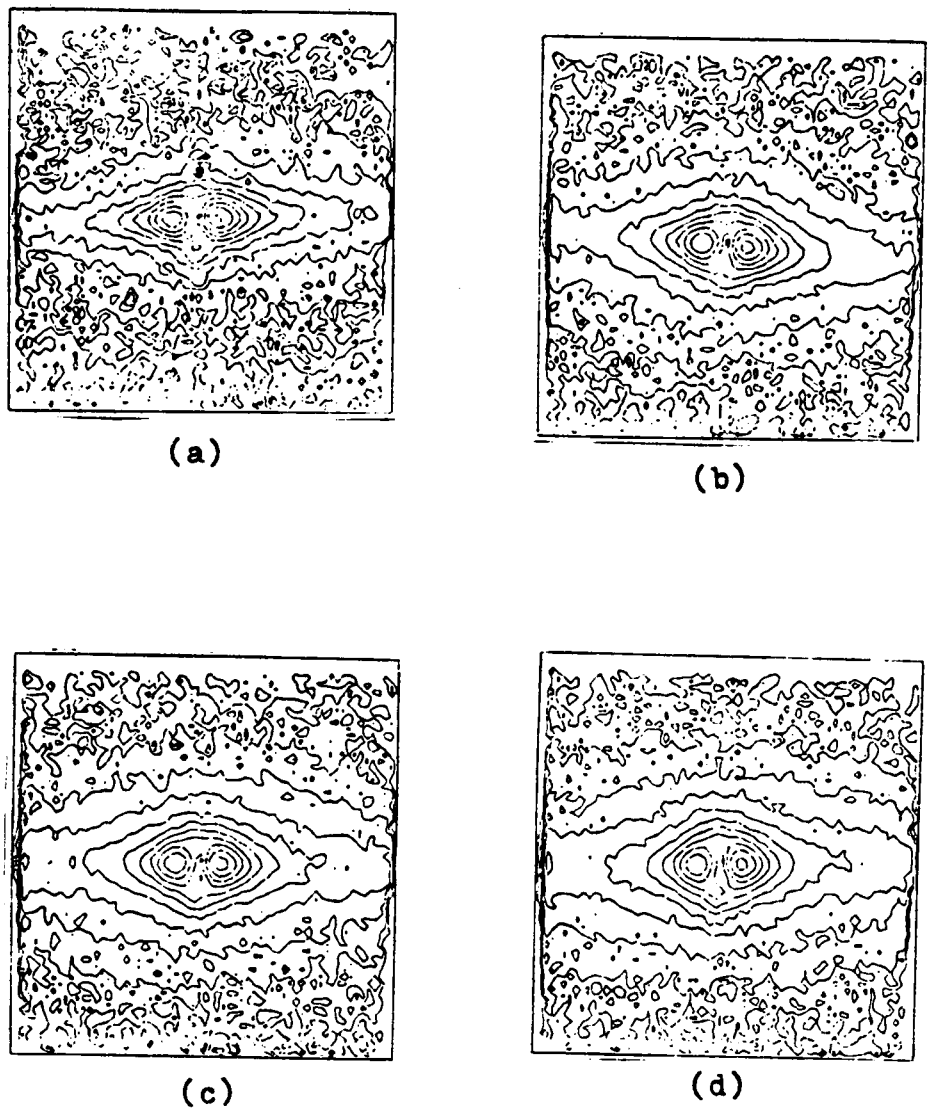

Figure 6-14. SAXS Contour Plots of Kevlar® 49 Fibers in the Long Geometry. (a) Unetched Fiber; (b) Etch Time 5 Min.; (c) Etch Time 10 Min.; (d) Etch Time 15 Min.

Table 6-2. Void Dimensions from Guinier Analysis of Plasma Etched Kevlar® 49 Fibers

Etch Time (min)	Short Geometry Width (nm)	Short Geometry Length (nm)	Long Geometry Width (nm)	Long Geometry Length (nm)
0	5.7	8.6	35	40
5	5.7	8.3	38	37
10	5.8	8.5	39	35
15	5.7	8.8	40	36

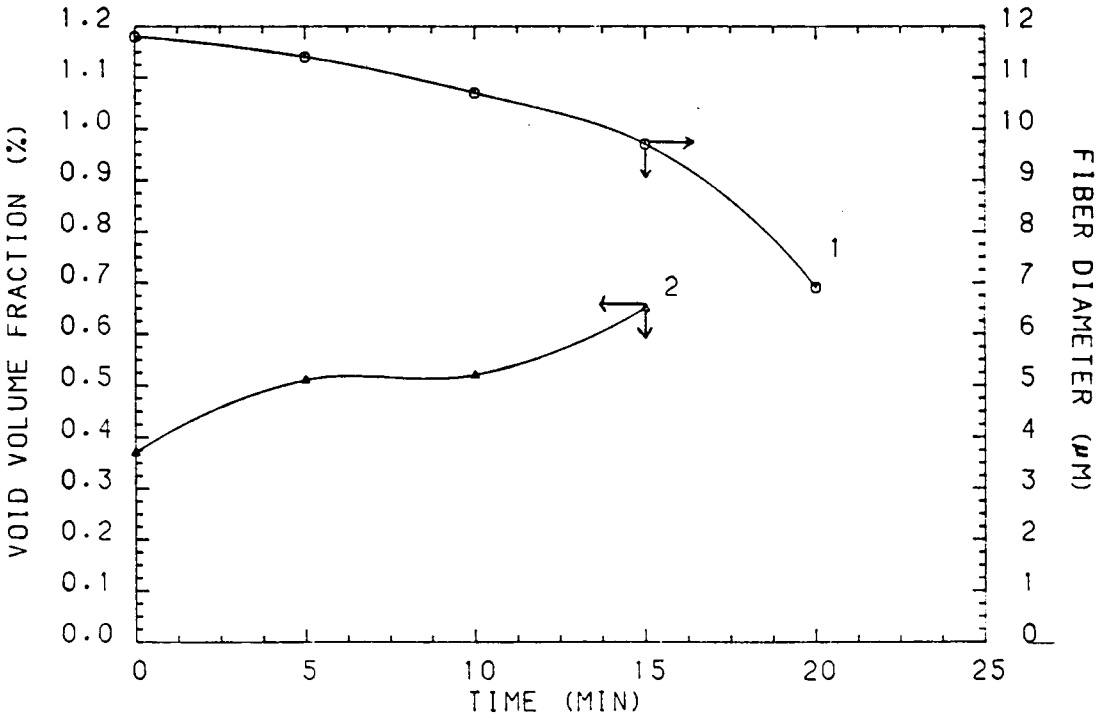

Figure 6-15. (1) Variation in Kevlar® 49 Fiber Diameter as a Result of Plasma Etching; (2) Volume Fraction of Voids Determined by Invariant Analysis Versus Plasma Etch Time.

micrographs of Kevlar® 49 fibers stained with silver sulfide, it was concluded that the voids are located mainly around the periphery of the fibers.

Panar et al. (38) exposed Kevlar® 49 fiber ends to an argon plasma. The core of the fiber was preferentially degraded as a result of this treatment. Another observation was that continuous fibers are not dyeable but damaged fibers and staple are accessible to some extent. Optical micrographs indicated that the dye selectively goes to the core of the fibers either from the fiber ends or through cracks in the skin in damaged fibers. Panar suggested that Dobb observed voids only in the more perfect skin of the fibers and that the majority of the voids are in the fiber core.

From the results of the experiments presented in this chapter, the voids in Kevlar® 49 fibers were found to be accessible to a diffusing liquid, in this case glycerin. From the plasma etching experiment, the small angle x-ray scattering pattern of the largest voids differed from the scattering pattern of the unetched Kevlar® 49 fiber. This is evidence that the largest voids are located in the fiber skin and are directly connected to the fiber surface. The unchanged scattering pattern of the smallest voids, regardless of plasma etch time, indicates that they are isolated in the core of the fiber. The increase in the volume fraction of the voids as the plasma etch time increases suggests that the majority of voids detectable by SAXS are located in the fiber core. Although the core of the Kevlar®

49 fibers was not preferentially degraded as observed by Panar, there was an increased plasma activity on the central part of the core when the fiber end was exposed to the plasma. This supports the argument of a larger number of voids in the core of the fiber because the voids allowed a greater accessibility of the plasma to the core of the fiber.

6.2 SAXS Analysis of Kevlar® 49 Fiber Reinforced Composites

In order to distinguish any scattering from the cured epoxy in the composite sample, the SAXS contour pattern of the cured epoxy was determined. The results shown in Figure 6-16 indicates that the electron density variation in the epoxy is small and no discernible scattering pattern is present. The scattering patterns were all qualitatively the same regardless of the amine content used to cure the epoxy. A representative scattering pattern for a Kevlar® 49 fiber reinforced composite is given in Figure 6-17. The scattering pattern closely resembles the SAXS pattern of the glycerin soaked Kevlar® 49 fibers. Therefore, it is reasonable to believe that the epoxy was capable of entering the larger voids in the Kevlar® 49 fiber.

To determine if voids are created during the failure process, the epoxy and composite samples were fractured in an Instron Tensile Tester. The scattering pattern from the fractured epoxy samples showed a relatively intense isotropic pattern as illustrated in

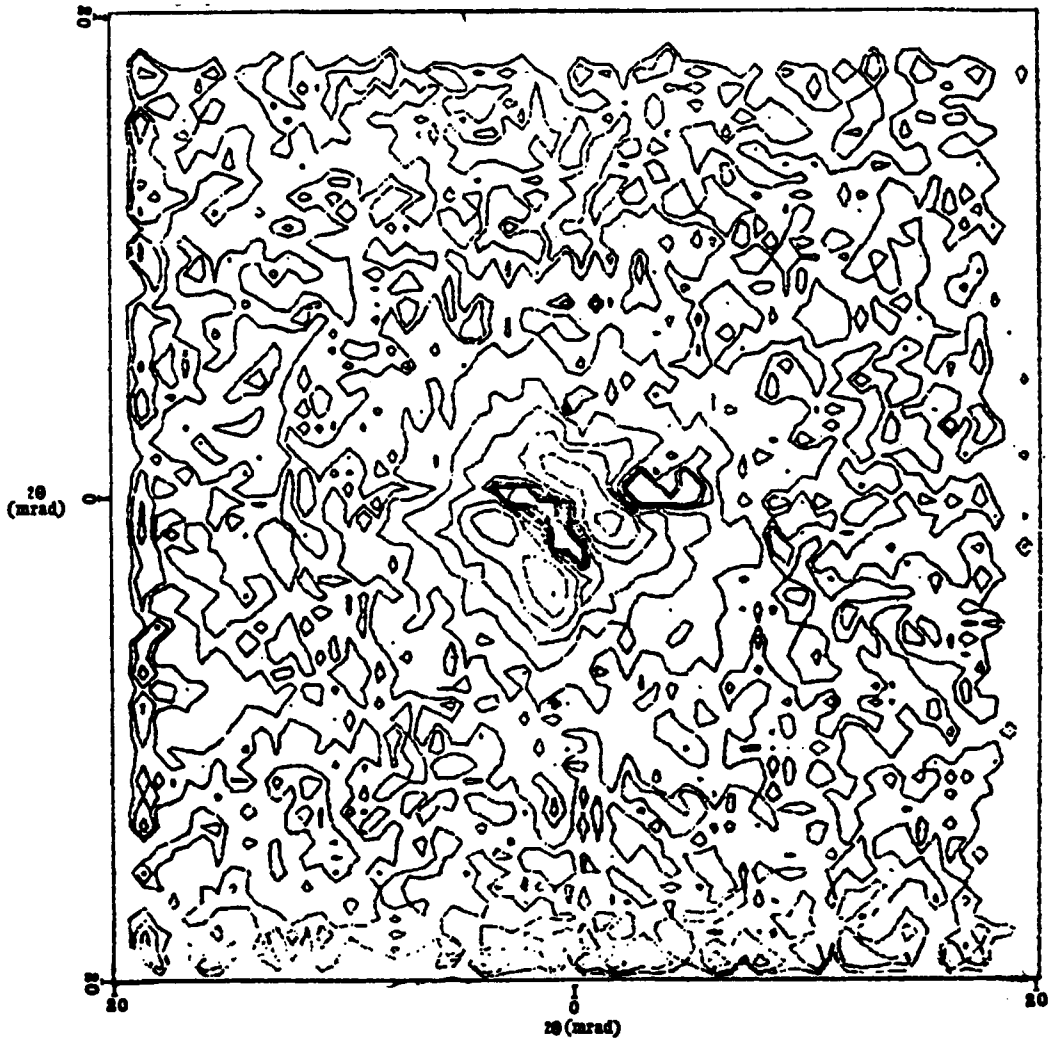

Figure 6-16. Two-Dimensional Isointensity Contour Plot of Cured Epoxy Resin from the Long Geometry. 47 phr Amine Content.

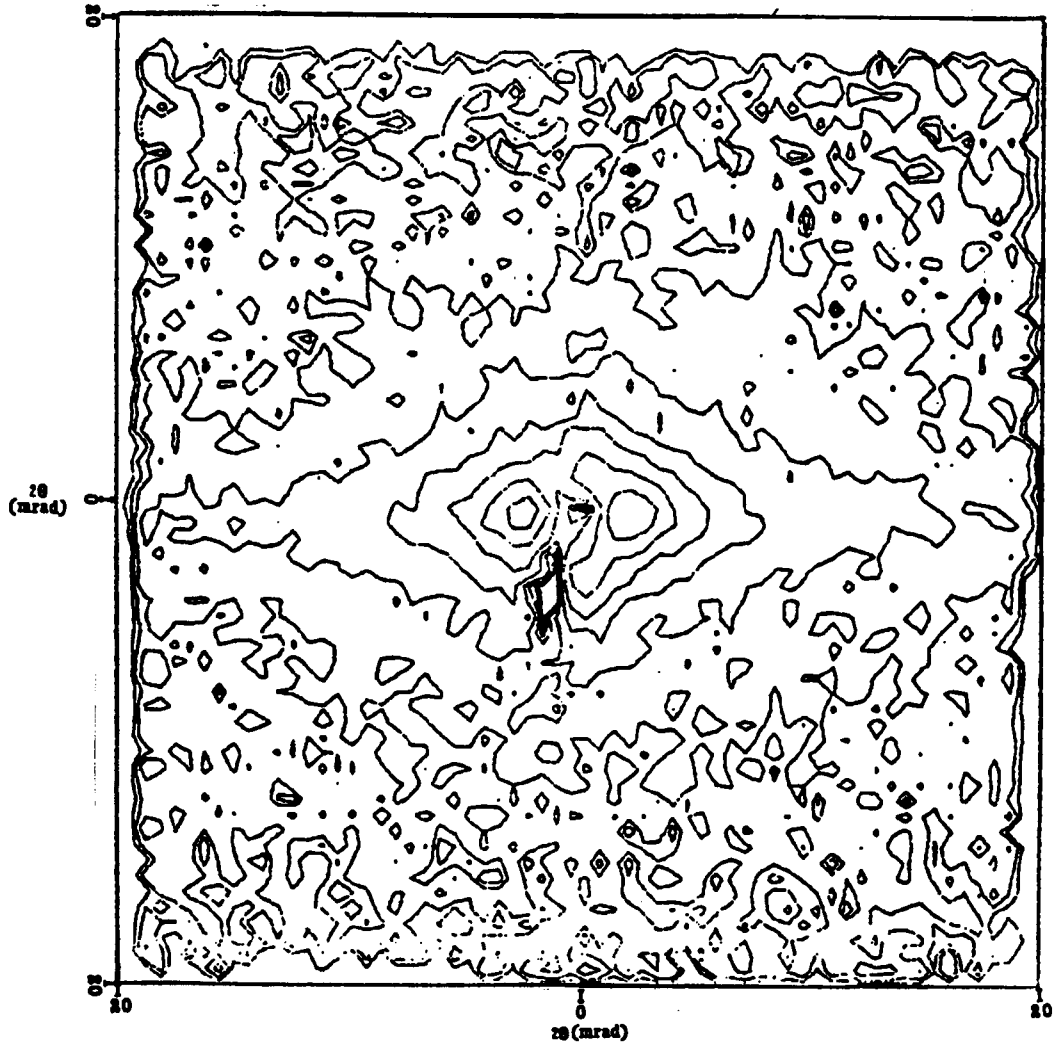

Figure 6-17. Two-Dimensional Isointensity Contour Plot of a Kevlar® 49 Fiber Reinforced Composite from the Long Geometry. 47 phr Amine Content, 14.2% Volume Fraction of Fiber.

Figure 6-18. From this it indicates that some voids are created in the epoxy before fracture occurs. The width of the voids determined from the Guinier analysis was found to be 36 nm. The SAXS pattern from the fractured Kevlar® 49 fiber reinforced epoxy composite is illustrated in Figure 6-19. The anisotropic pattern probably results from a combination of scattering from voids created in the Kevlar® 49 fiber as well as voids created in the epoxy. The voids were determined to have a width of 46 nm and a length of 56 nm. In an attempt to obtain the scattering pattern due to only the fibers in the composite, the scattering pattern from the fractured epoxy sample was subtracted from the scattering pattern of the fractured composite. Since the composites contain a low volume fraction of Kevlar® 49 fibers, about 15%, the voids created in the epoxy matrix of the composite are assumed to be equivalent to the voids created in the unreinforced epoxy. The SAXS pattern of the net scattering from the Kevlar® 49 fibers in the composite is illustrated in Figure 6-20. The resulting scattering pattern resembles the pattern from a bundle of Kevlar® 49 fibers. The dimensions of the voids determined from the Guinier analysis had a width of 44 nm and a length of 66 nm. These dimensions are larger than those determined for the bundle of Kevlar® 49 fibers. This indicates that larger voids were created in the Kevlar® 49 fiber composite as a result of the applied stress either by creation of new voids or by the combination of the smaller voids.

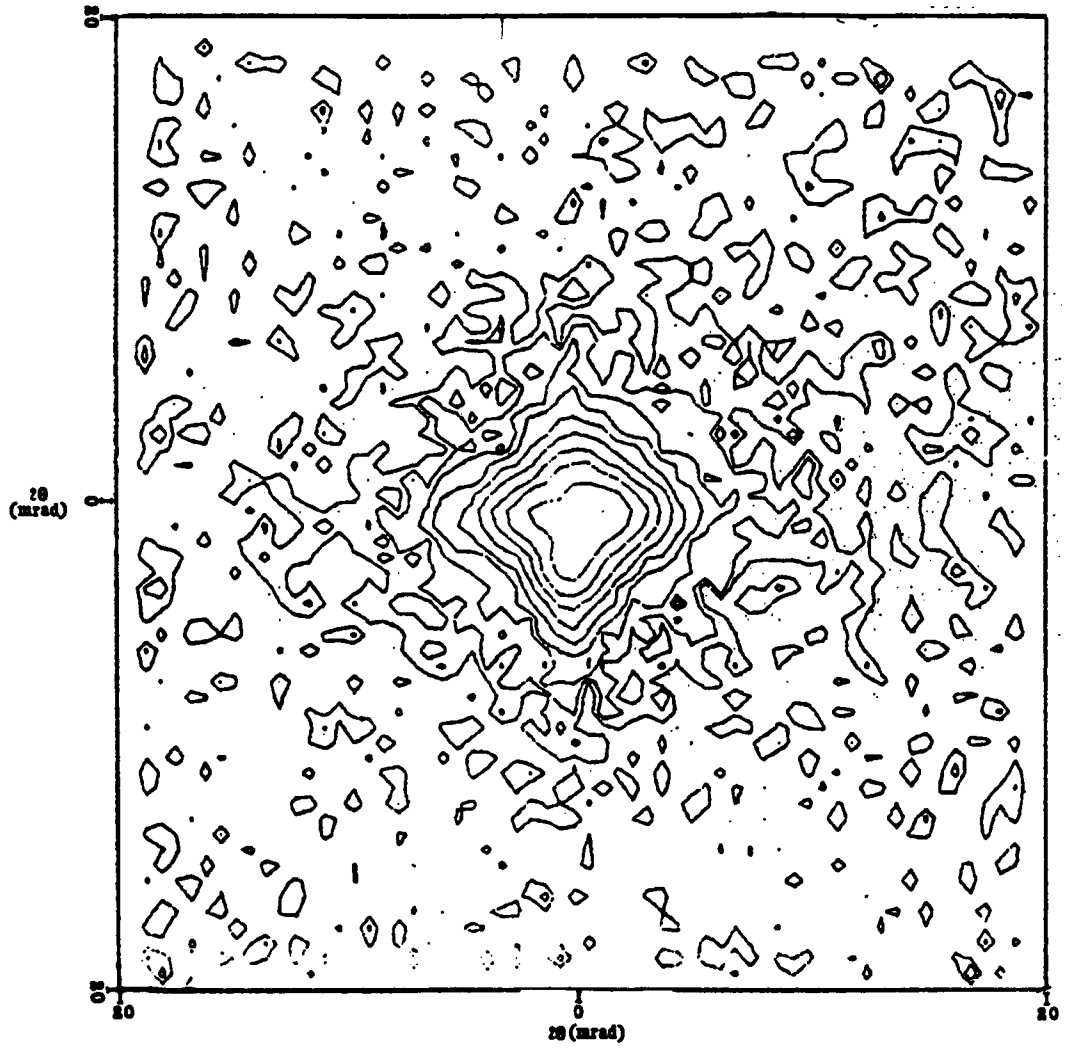

Figure 6-18. Two-Dimensional Isointensity Contour Plot of a Fractured Epoxy Resin from the Long Geometry. 47 phr Amine Content.

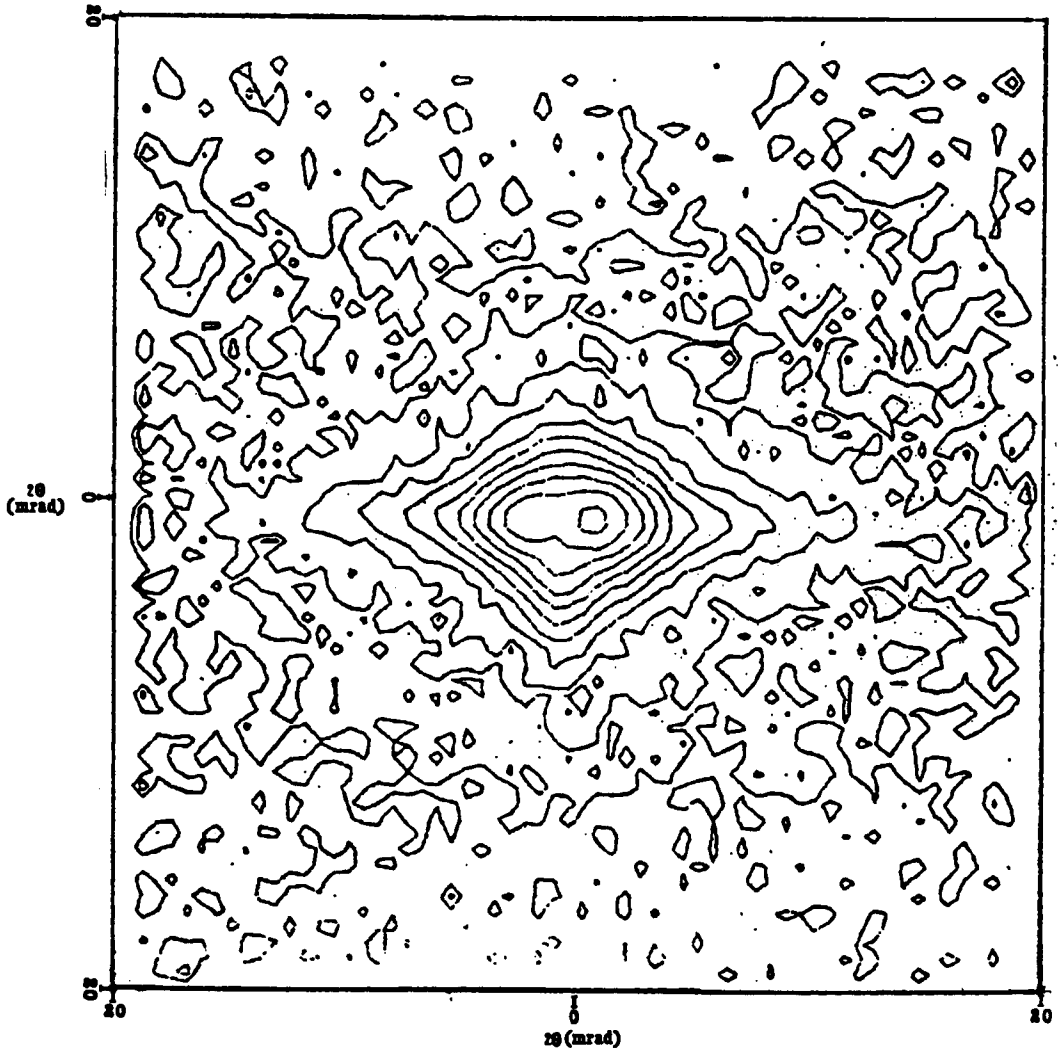

Figure 6-19. Two-Dimensional Isointensity Contour Plot of a Fractured Kevlar® 49 Fiber Reinforced Composite from the Long Geometry. 47 phr Amine Content, 14.2% Volume Fraction of Fiber.

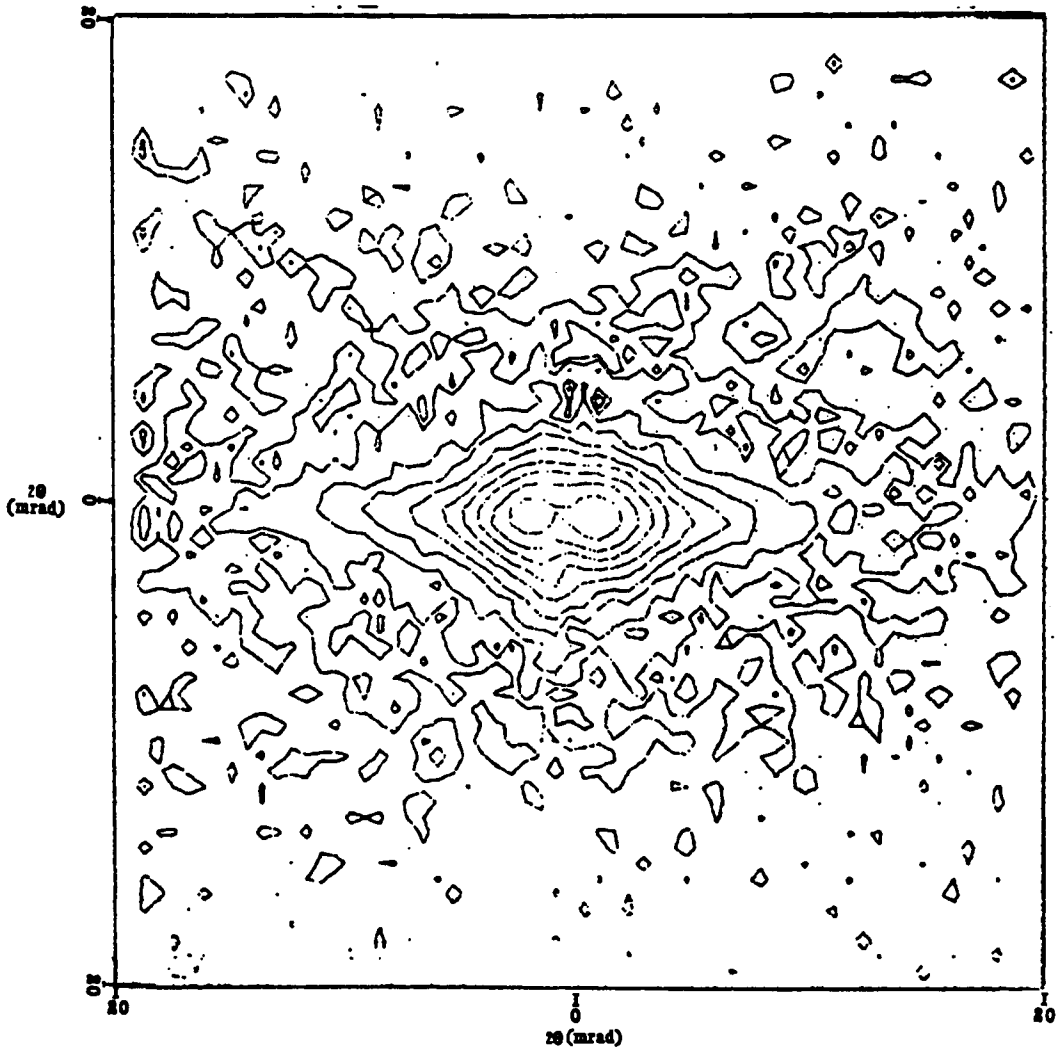

Figure 6-20. Two-Dimensional Isointensity Contour Plot of the Kevlar® 49 Fiber Scattering in the Fractured Composite from the Long Geometry. 47 phr Amine Content, 14.2% Volume Fraction of Fiber.

6.3 Mechanical Properties of Uniaxial Kevlar® 49 Fiber Reinforced Epoxy Composites

This section examines the mechanical response of Kevlar® 49 fiber reinforced epoxy composites when stressed along the fiber axis direction. The amine content used to cure the epoxy was varied in order to obtain several epoxy compositions with varying ultimate strains. Tensile tests were used to study the mechanical beh-vior of these epoxies and their composites at each epoxide-amine ratio. Two volume fractions of fibers were used at each level of amine content.

The epoxy system of Dow D.E.R. 332 cured with Jeffamine T-403 has been studied by Kong et al. (25). The amine contents of 47, 32.5, and 25 parts per hundred resin were chosen to represent extremes in the ultimate strain of the cured epoxy as determined by their work. The volume fractions of Kevlar® 49 fibers used at each level of amine concentration are presented in Table 6-3.

Table 6-3. Volume Fraction of Kevlar® 49 Fibers in Composites

Amine Content (phr)	Low Volume Fraction (%)	High Volume Fraction (%)
47.0	7.0	14.2
32.5	8.2	17.9
25.0	6.9	13.8

For the stoichiometric ratio of 47 phr, the stress-strain curves are illustrated in Figure 6-21 for the epoxy and the composites. The low volume fraction composite failed at a strain of 7.5% and an ultimate stress of 330 MPa. A strain of 10.2% and an ultimate stress of 580 MPa was recorded for the high volume fraction composite. At this stoichiometry, the unreinforced epoxy had an ultimate strain of 12.6% and a yield stress of 65 MPa. The ultimate tensile strength of the composites was slightly below the Rule of Mixtures, probably due to the effect of flaws in the composite.

The stress-strain curves for the epoxy system containing 32.5 phr amine content along with the composites made using this epoxy system are presented in Figure 6-22. An unusual feature is that the failure strain of the composites is higher than the failure strains of either the unreinforced epoxy or the Kevlar® 49 fibers. The epoxy system containing 25 phr amine content has approximately half of the epoxide groups reacted. As a result of the low cross-link density, the epoxy has an ultimate strain around 70% and a low ultimate stress of 14 MPa. The composites made with this amine content were disappointing. The weakness of the epoxy matrix prevented it from carrying the stress transferred from the fiber. As a result the composite failed at a strain below 5% and at a stress level that differed only slightly from that of a dry fiber bundle.

The SEM micrograph of the fracture surface of the composite cured with 47 phr amine content and 14.2% volume fraction of fiber is shown in Figure 6-23. The epoxy resin appears to adhere well

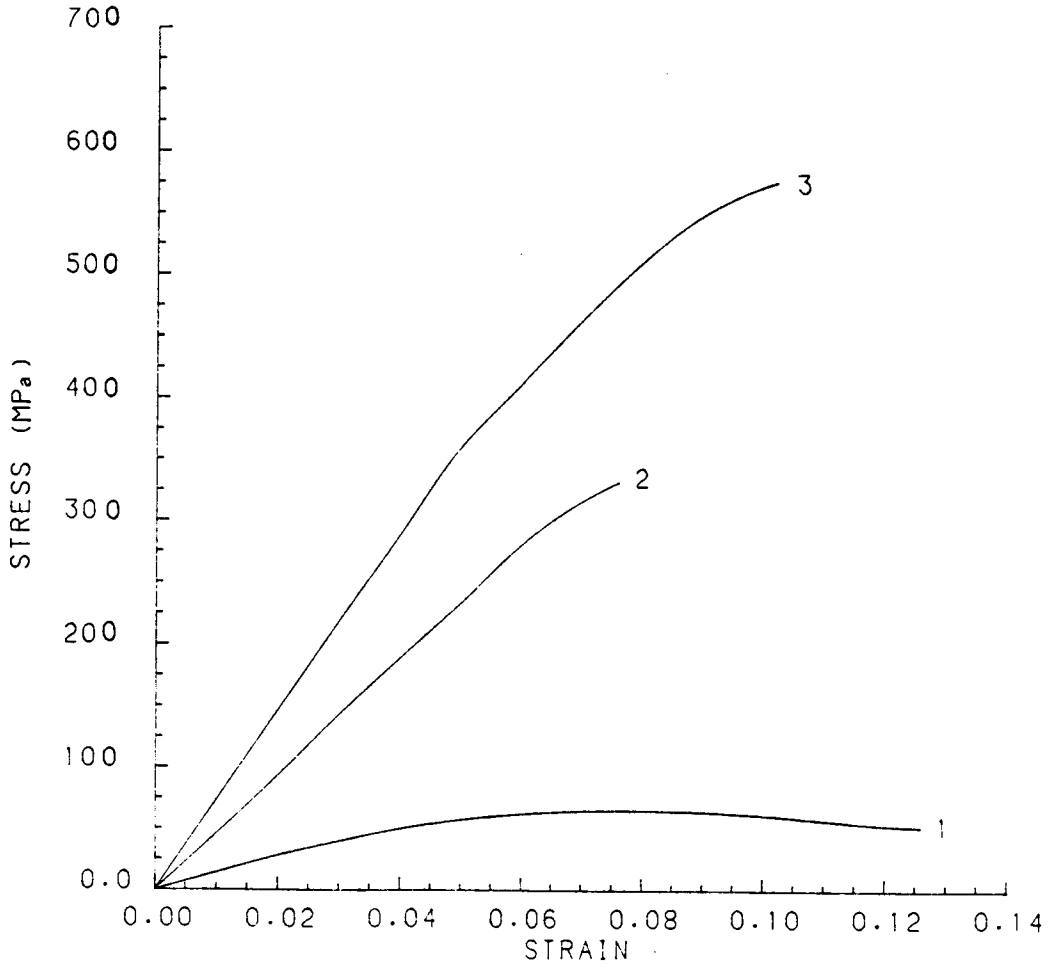

Figure 6-21. Stress-Strain Curve for Epoxy Resin and Composites Containing 47 phr Amine Content. (1) Epoxy Resin; (2) 7.0% Volume Fraction Fiber Composite; (3) 14.2% Volume Fraction Fiber Composite.

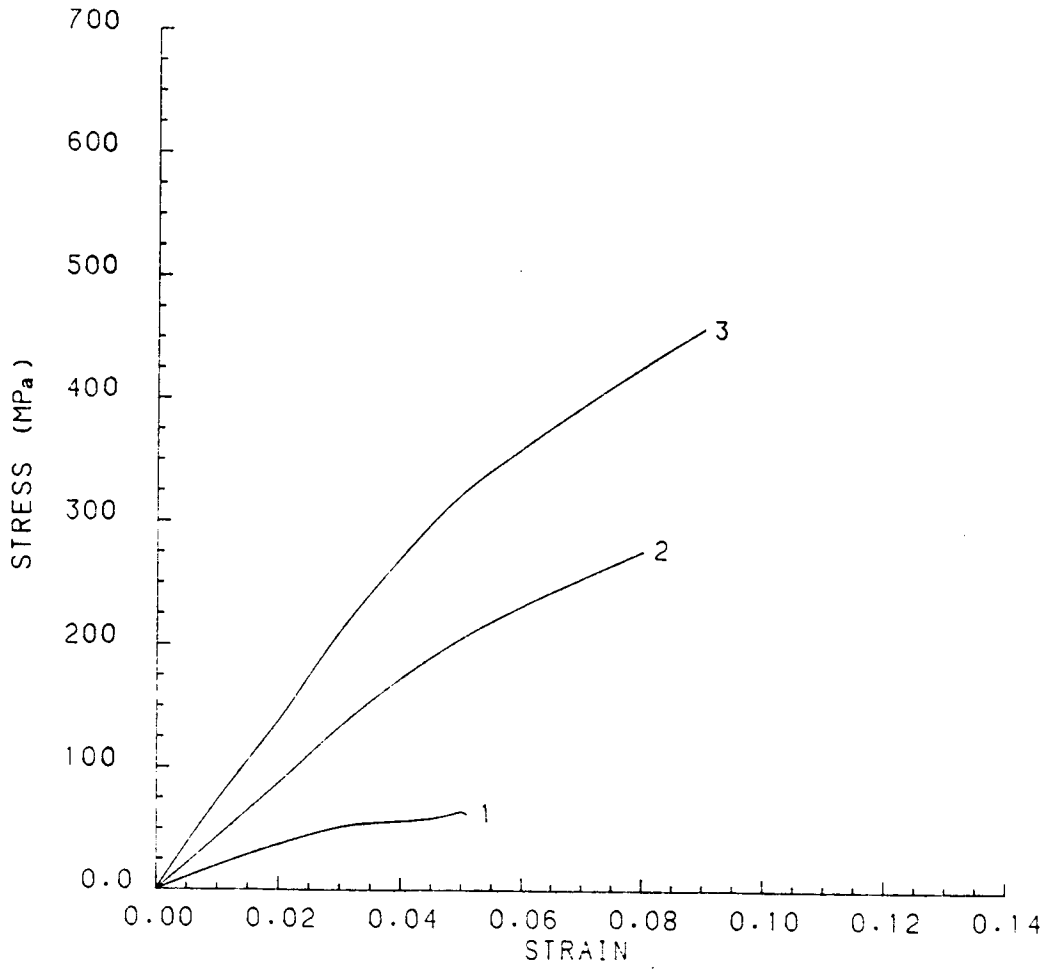

Figure 6-22. Stress-Strain Curve for Epoxy Resin and Composites Containing 32.5 phr Amine Content. (1) Epoxy Resin; (2) 8.2% Volume Fraction Fiber Composite; (3) 17.9% Volume Fraction Fiber Composite.

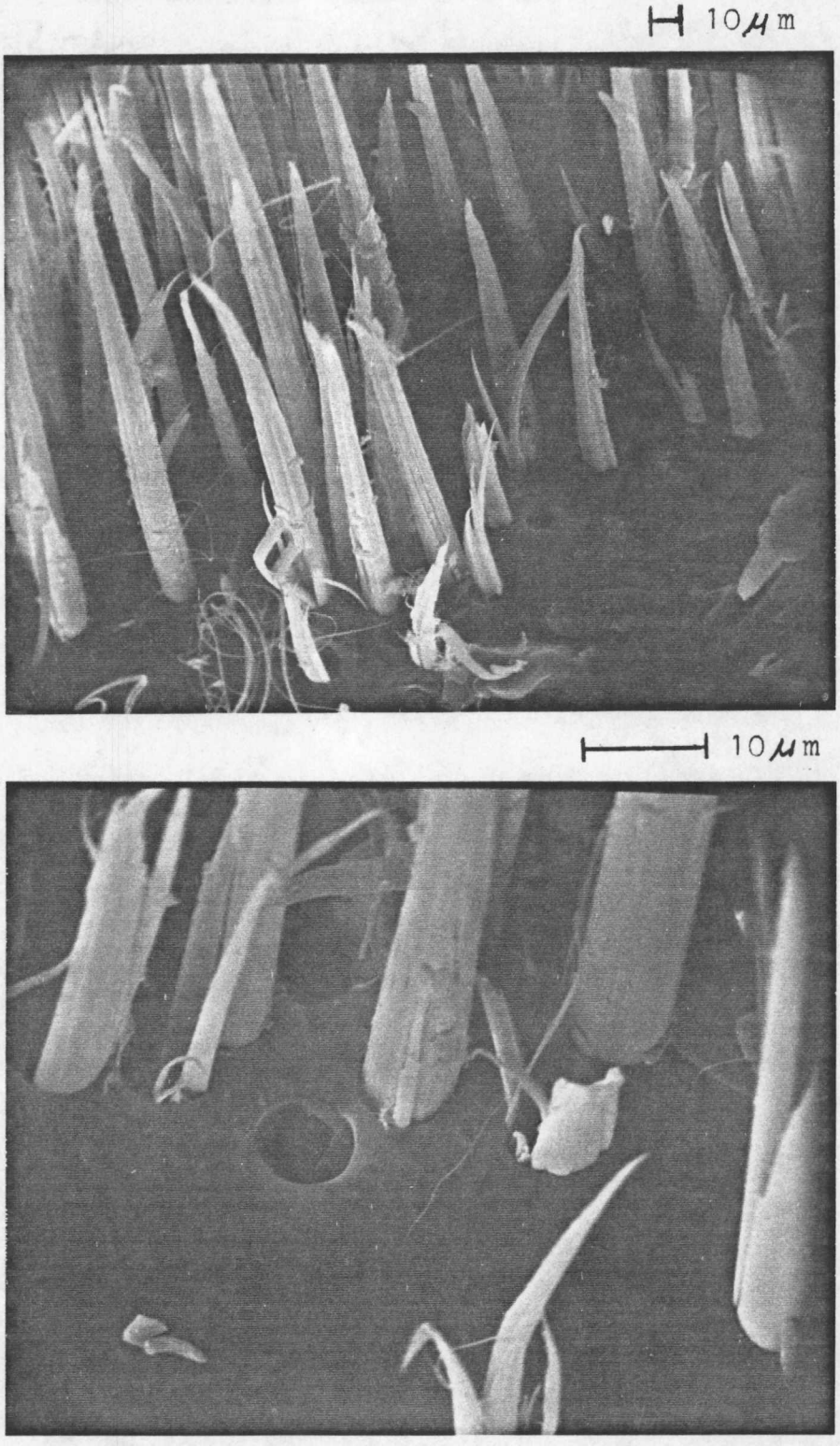

Figure 6-23. SEM Micrograph of the Fracture Surface of a Kevlar® 49 Fiber Reinforced Composite. 47 phr Amine Content, 14.2% Volume Fraction of Fiber.

to the Kevlar® 49 fiber skin as evidenced by fragments of skin remaining in holes where the fiber has pulled out. The outer surface layer of Kevlar® 49 fibers show severe splitting along the longitudinal fiber axis.

Since the Kevlar® 49 fibers have a lower breaking strain than the epoxy resin used in making the composite, the fibers are expected to break first and control the tensile strength of the composite. These composites contain relatively low volume fractions of fibers, therefore the epoxy matrix can absorb the stored elastic energy when the first fibers break and prevent catastrophic failure from occurring. It is assumed that when the fibers break due to a flaw, they break up into lengths above the critical length that can still contribute to the reinforcement of the composite. As the composite approaches the breaking point, the fibers get progressively shorter before the composite fails completely. These are characteristics of a composite made with a brittle fiber with good adhesion to a ductile matrix.

6.4 WAXS Analysis of Graphite Fibers

In order to qualitatively determine the degree of preferred orientation of the graphite crystallites in the three types of graphite fibers used, the wide angle film diffraction patterns were obtained with the fiber axis directed vertical to the x-ray beam and parallel to the beam. These patterns are shown in Figure 6-24 for the pitch-based graphite fiber, VSB-16, in Figure 6-25 for the high modulus PAN-based graphite fiber, HMS, and in Figure 6-26 for the low modulus

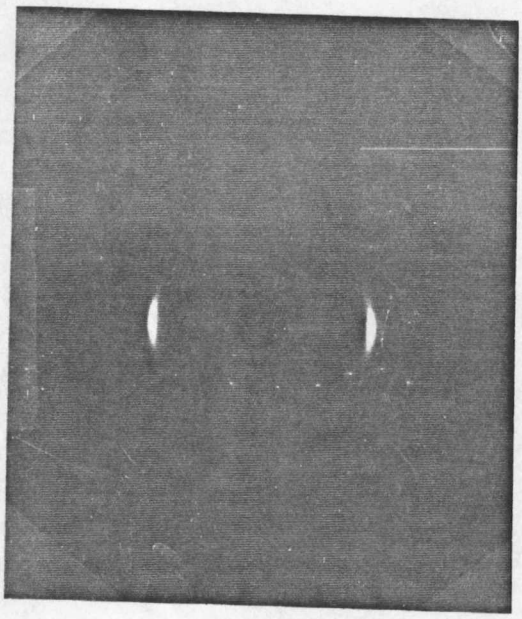

(a)

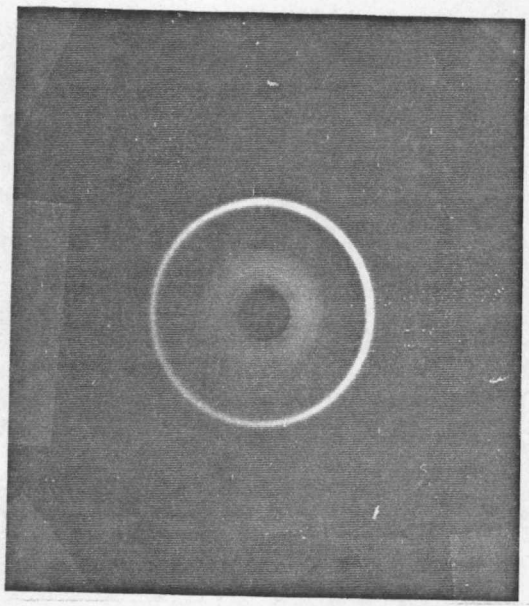

(b)

Figure 6-24. WAXS Film Patterns of Pitch-Based VSB-16. (a) Fiber Axis Vertical to Beam; (b) Fiber Axis Parallel to Beam.

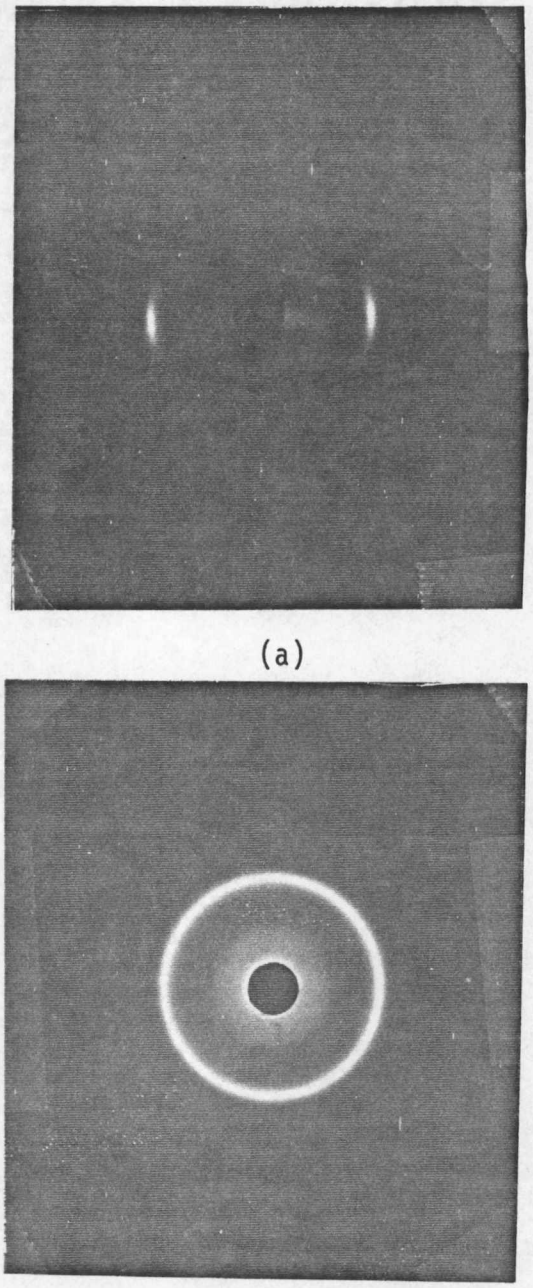

Figure 6-25. WAXS Film Patterns of PAN-Based HMS. (a) Fiber Axis Vertical to Beam; (b) Fiber Axis Parallel to Beam.

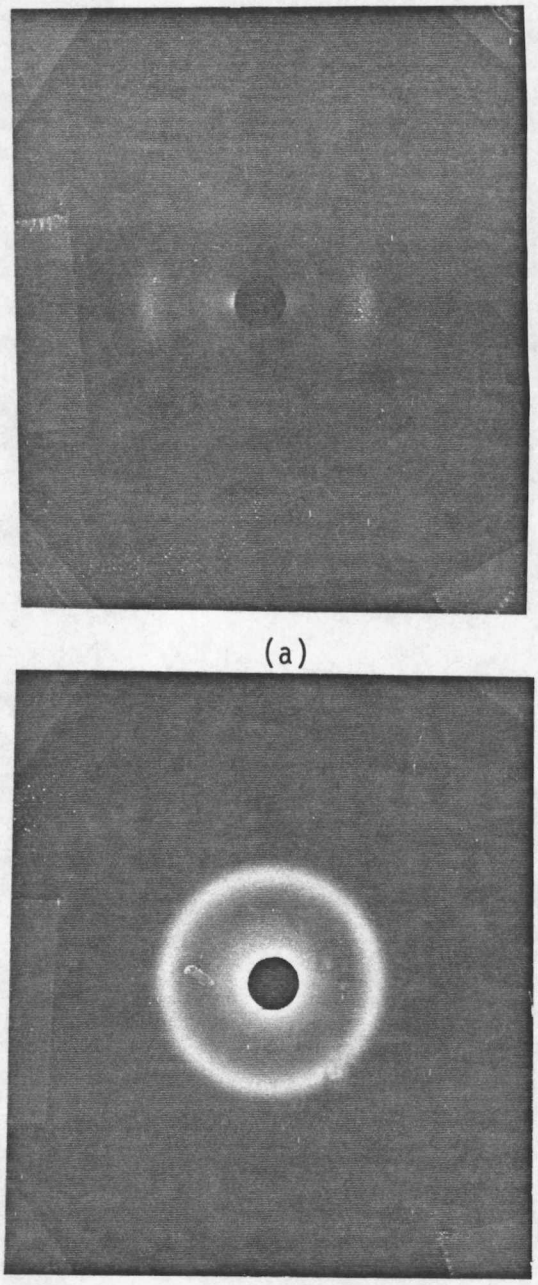

(a)

(b)

Figure 6-26. WAXS Film Patterns of PAN-Based AS4. (a) Fiber Axis Vertical to Beam; (b) Fiber Axis Parallel to Beam.

PAN-based graphite fiber, AS4. From the (002) reflections of these fibers, it was determined that the VSB-16 fiber contained the highest orientation, followed closely by the HMS fiber. The (002) reflection from the AS4 fiber was very diffuse indicating that the orientation was lower than the other fibers.

6.5 SAXS Analysis of Graphite Fibers

The SAXS contour plots of the three graphite fibers from the short SAXS geometry are illustrated in Figure 6-27 through Figure 6-29. For the VSB-16 fiber, the voids appear to have a preferred orientation of the long axis parallel to the fiber axis. The scattering from the AS4 fiber shows a lobed scattering pattern. This indicates that the voids are not oriented along the fiber axis to the degree found from the scattering pattern of the HMS fiber. From these SAXS contour patterns and with the WAXS film patterns, it can be concluded that the voids found in graphite fibers closely follows the orientation of the graphite crystallites in the fiber.

The SAXS contour plots of the fibers in the long geometry with the x-ray beam parallel to the fiber axis are presented in Figure 6-30 through Figure 6-32. From these isotropic scattering patterns, the geometry of the voids transverse to the fiber axis was found to be randomly oriented in all three fibers. The SAXS contour patterns taken in the long geometry with the fiber axis vertical to the beam are shown in Figure 6-33 through Figure 6-35. The

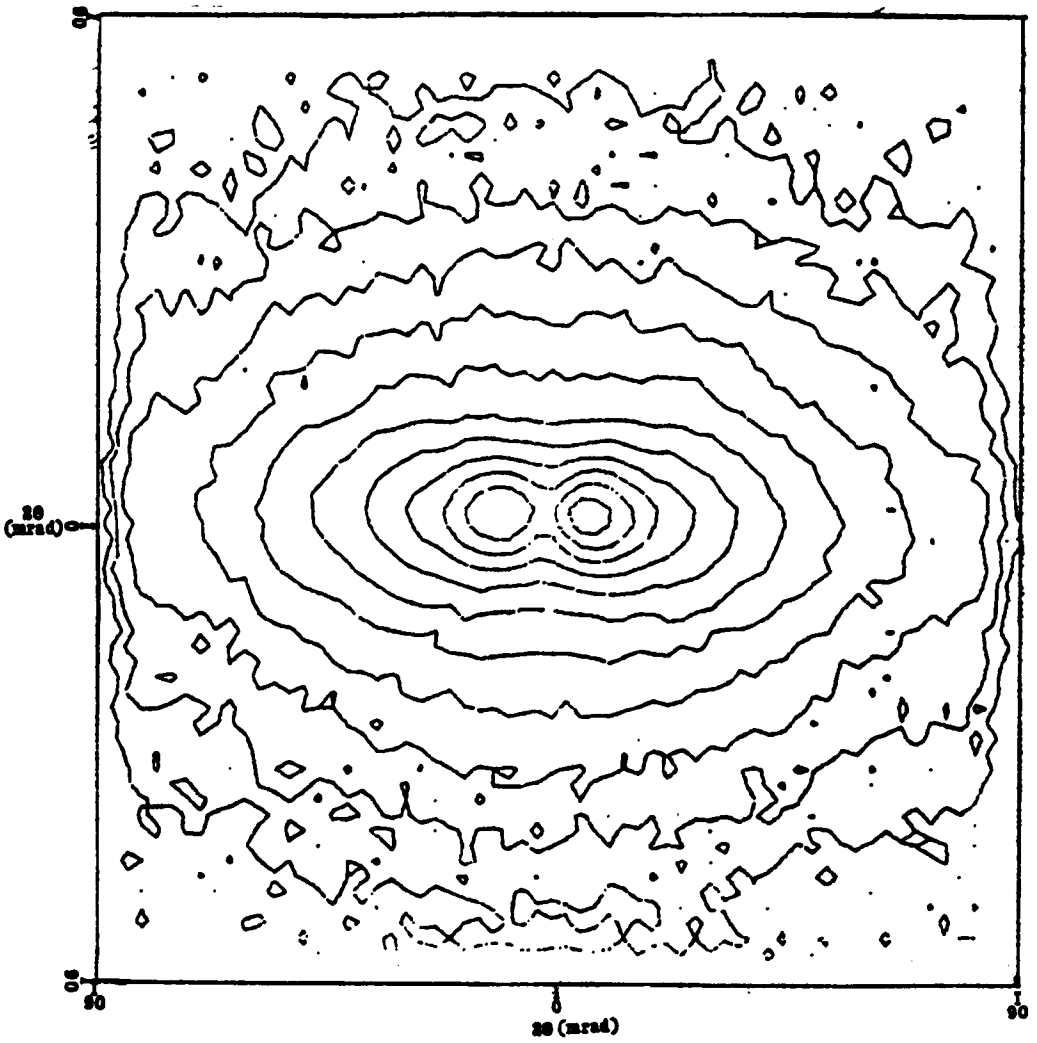

Figure 6-27. SAXS Contour Plot of VSB-16 from the Short Geometry.

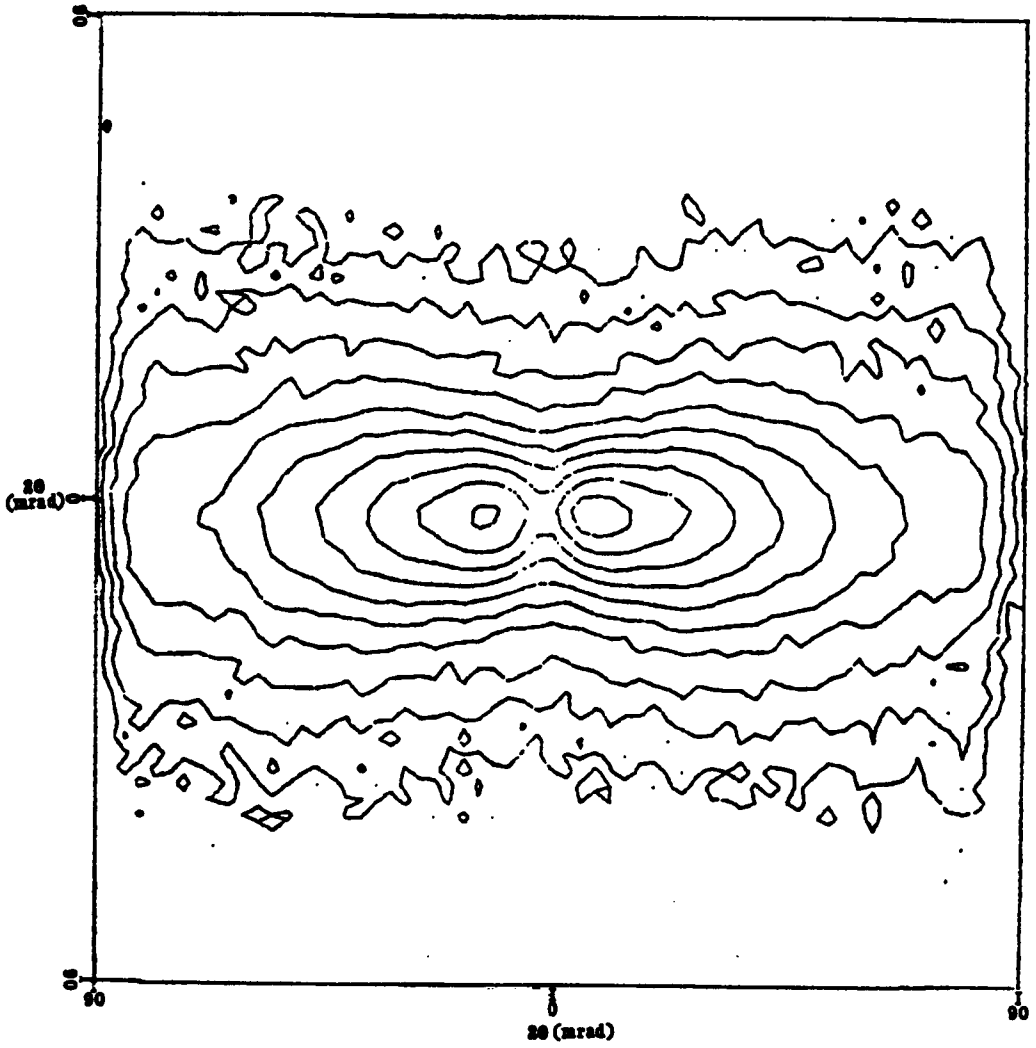

Figure 6-28. SAXS Contour Plot of HMS from the Short Geometry.

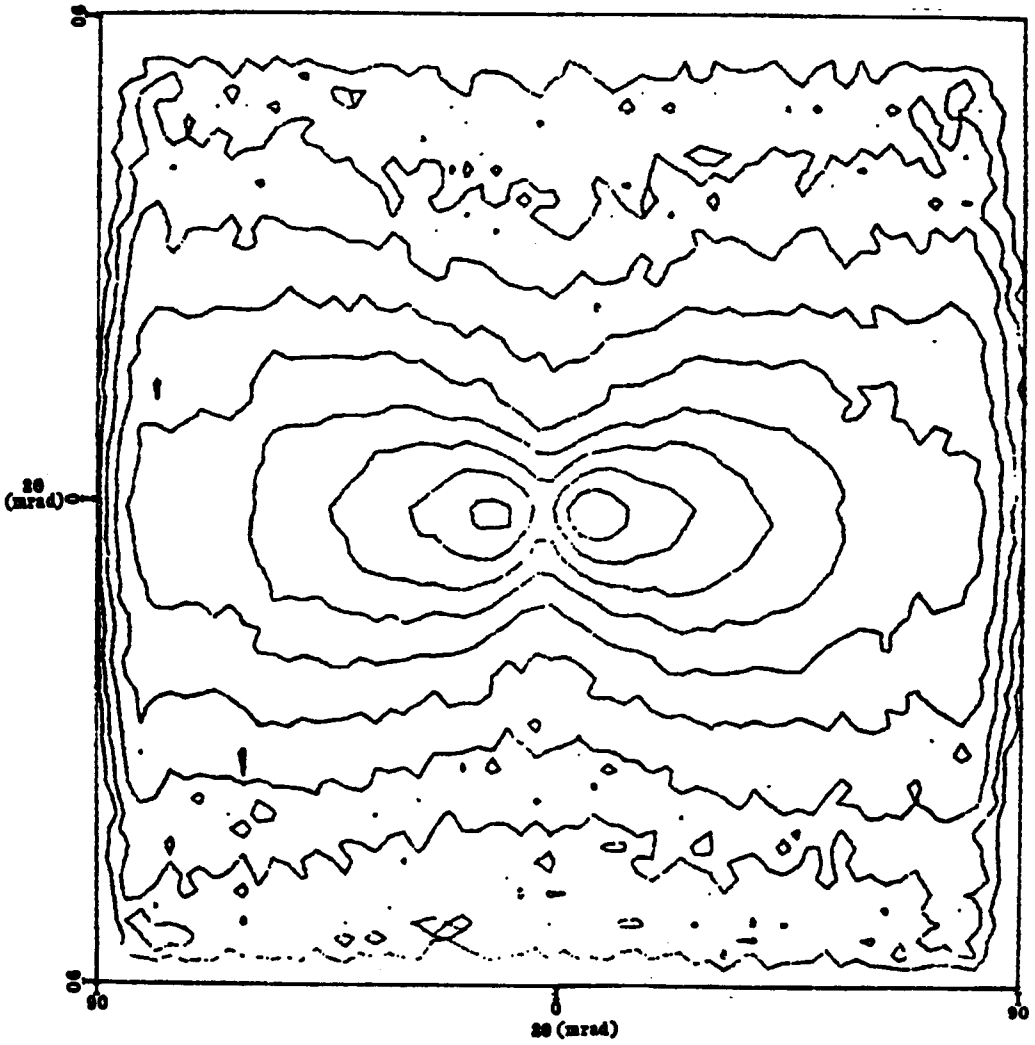

Figure 6-29. SAXS Contour Plot of AS4 from the Short Geometry.

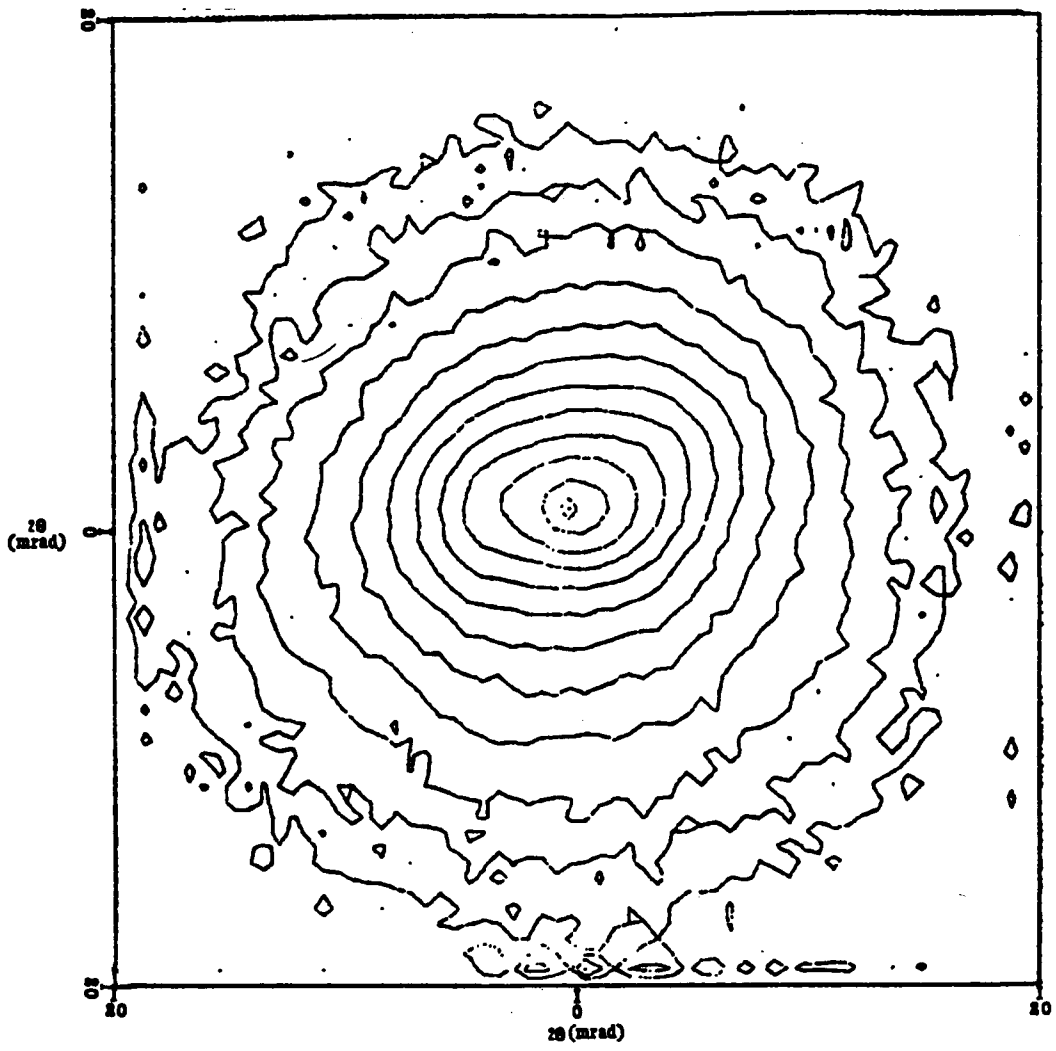

Figure 6-30. SAXS Contour Plot of VSB-16 Cross Section from the Long Geometry.

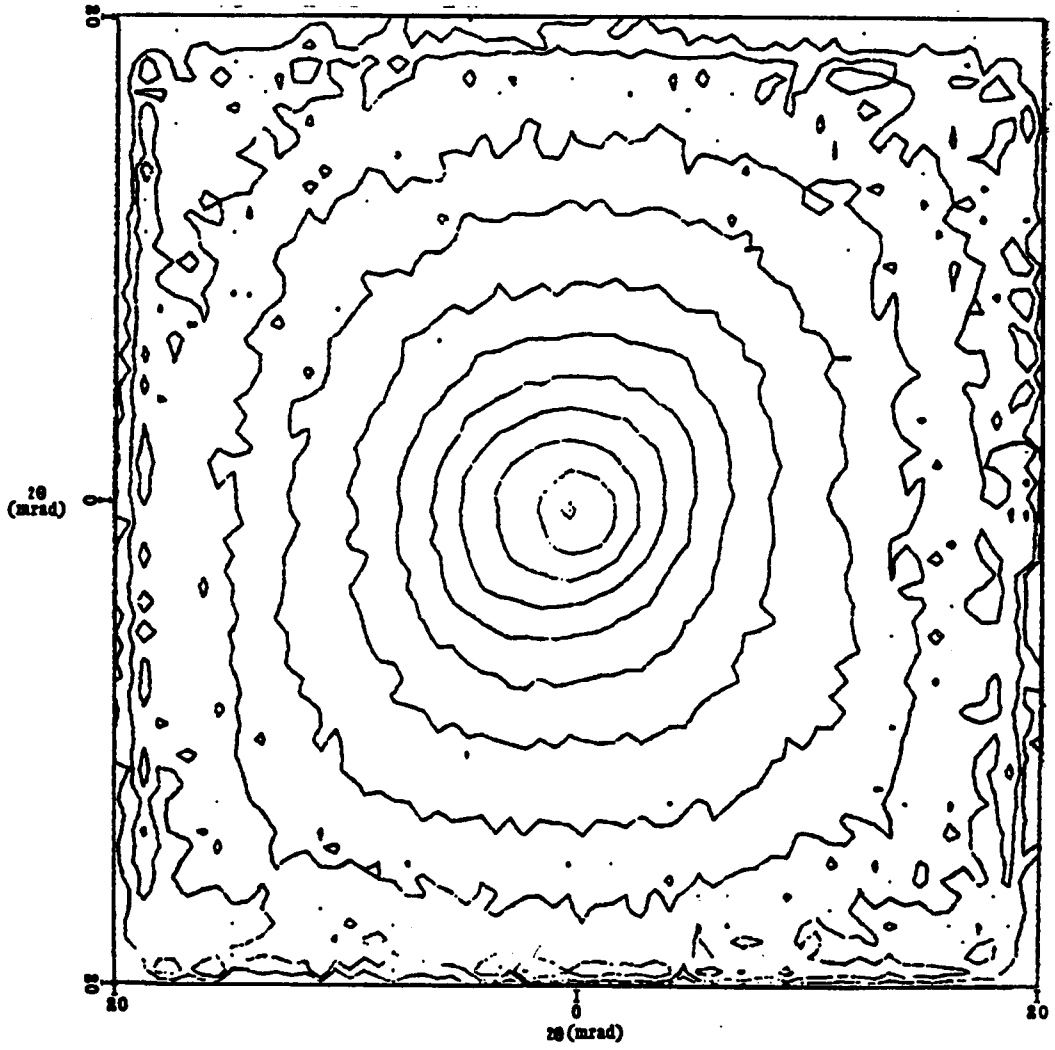

Figure 6-31. SAXS Contour Plot of HMS Cross Section from the Long Geometry.

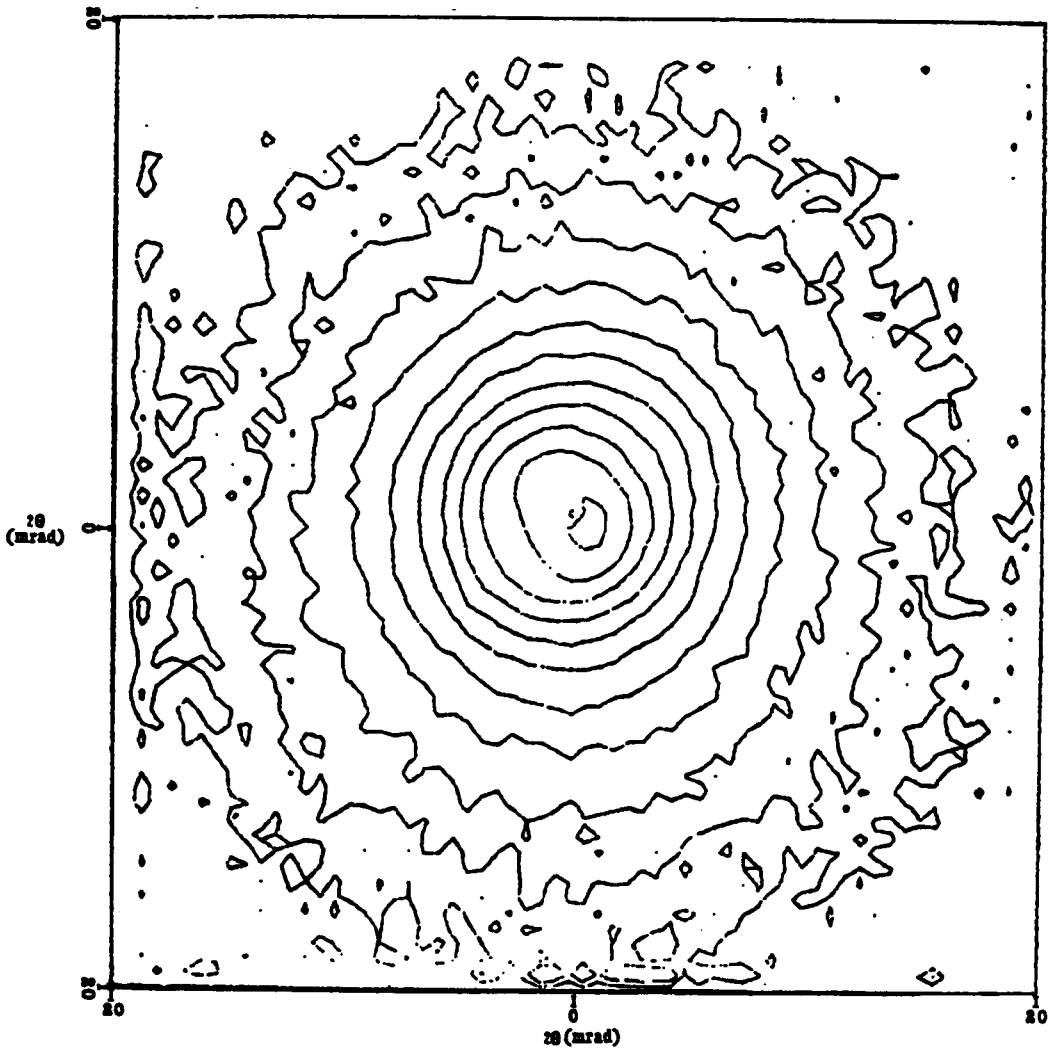

Figure 6-32. SAXS Contour Plot of AS4 Cross Section from the Long Geometry.

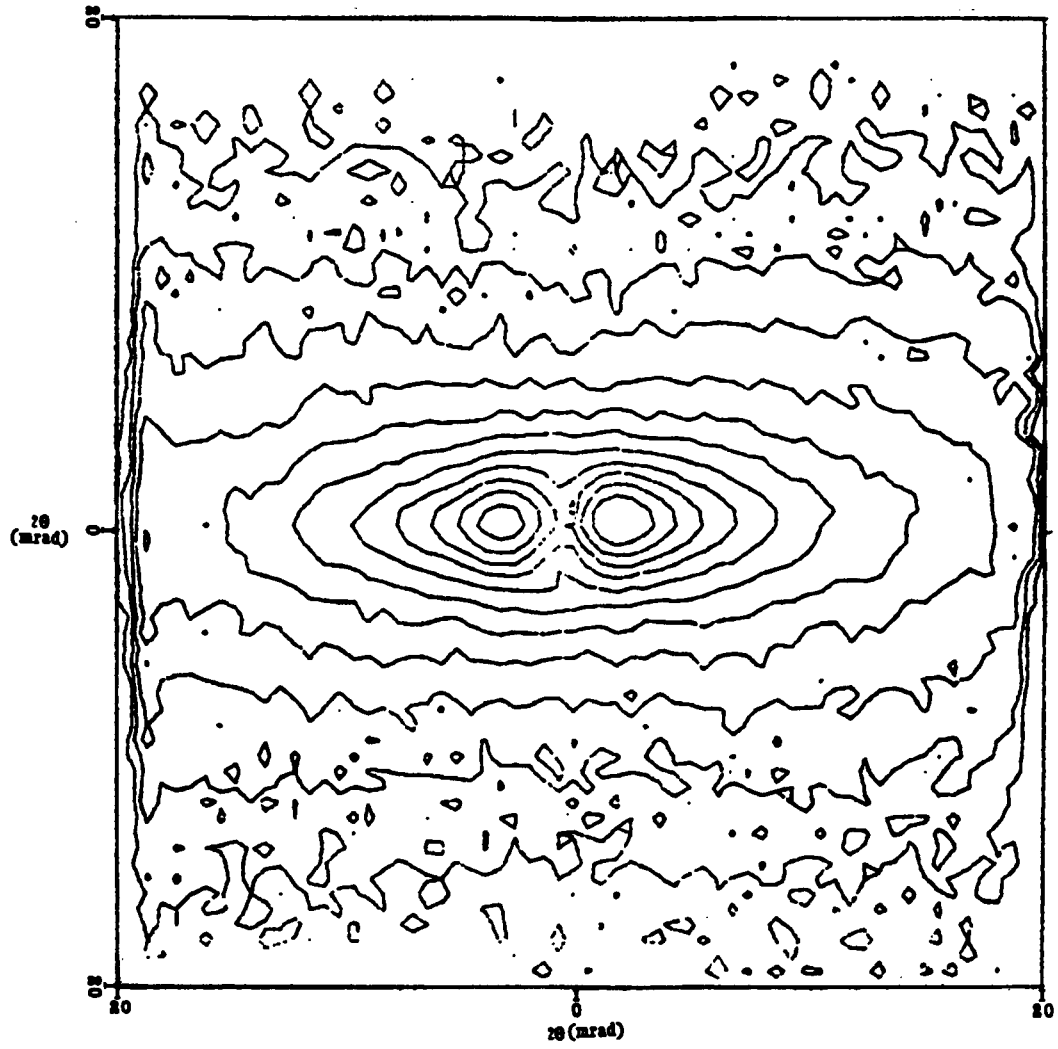

Figure 6-33. SAXS Contour Plot of VSB-16 from the Long Geometry.

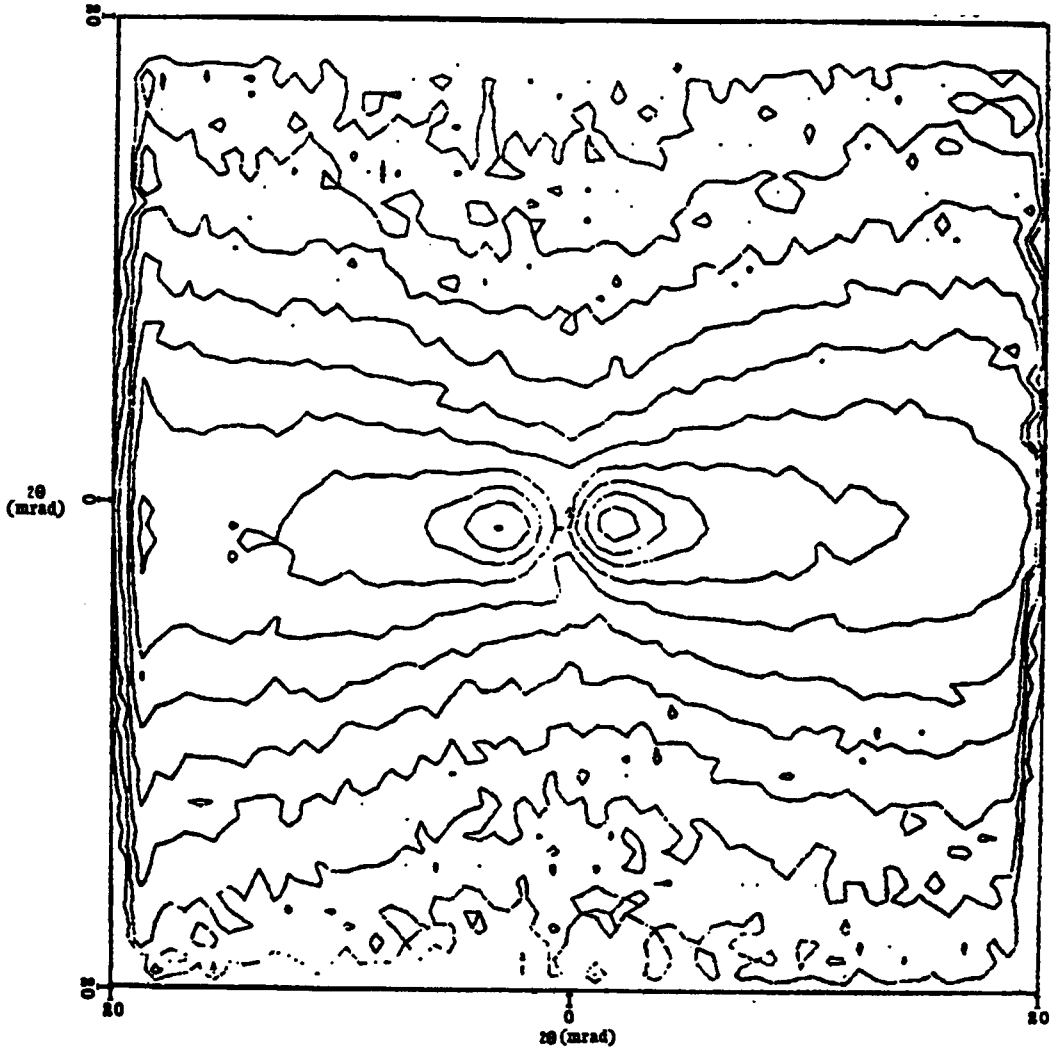

Figure 6-34. SAXS Contour Plot of HMS from the Long Geometry.

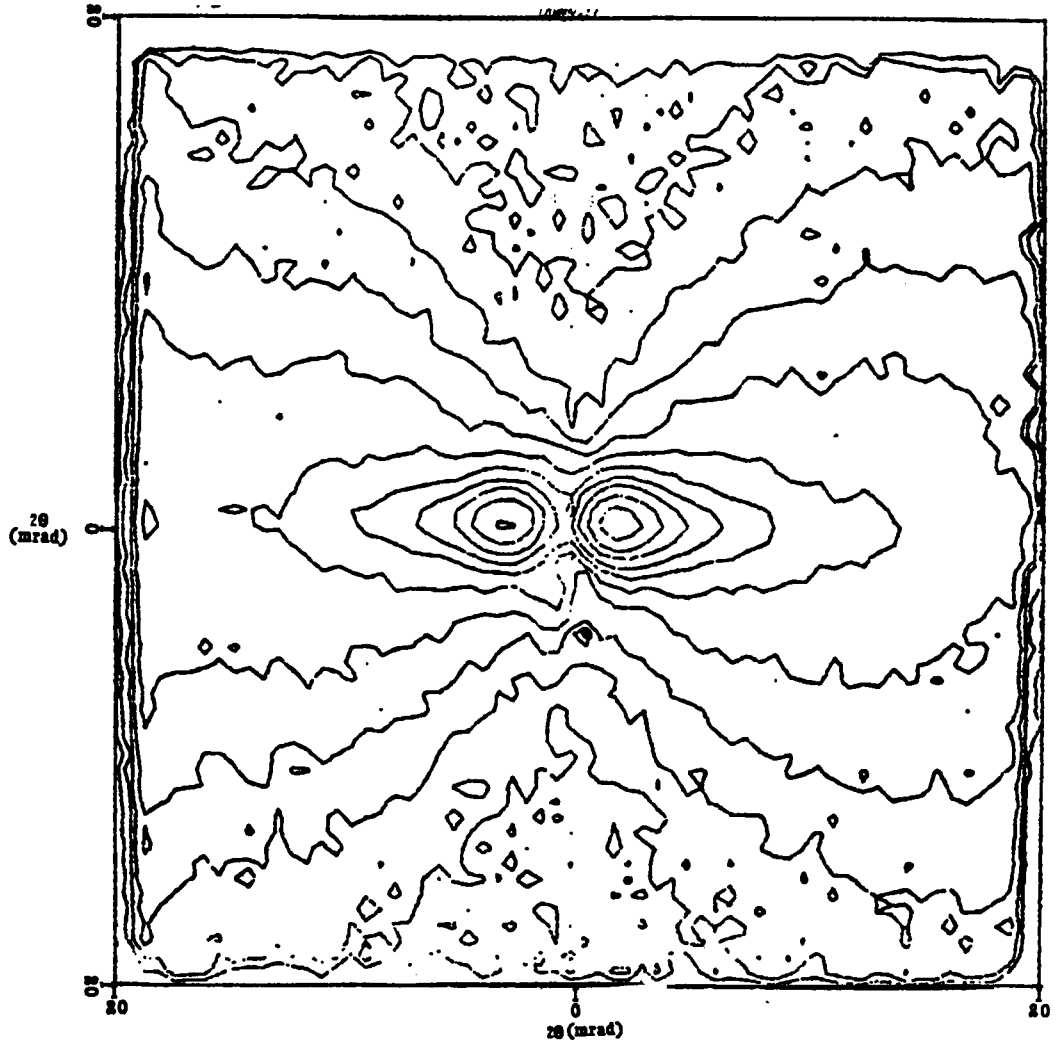

Figure 6-35. SAXS Contour Plot of AS4 from the Long Geometry.

geometry of the voids in VSB-16 was determined to be ellipsoidal, while the HMS and AS4 voids were cylindrical. The Guinier plots from an equatorial and meridional slice of the combined scattering data from the long and short geometries are shown in Figure 6-36 through 6-38 for each of the graphite fibers. The void size distribution found in these fibers is given in Table 6-4. From the invariant analysis, the void volume fraction in VSB-16 was calculated to be 3.5%, in HMS the void volume fraction was 8.8%, and in AS4 it was 5.8%.

6.6 SAXS Analysis of Glycerin Soaked Graphite Fibers

In order to determine if the microvoids in these graphite fibers were capable of allowing a liquid to diffuse into the voids and thereby changing the scattering pattern, the fibers were soaked in glycerin and the SAXS contour patterns were obtained in the same manner as that of the Kevlar® 49 fiber. The resulting SAXS contour patterns are illustrated in Figure 6-39 through Figure 6-41. The VSB-16 contour pattern of the glycerin soaked fiber shows no qualitative change from the dry fiber. The HMS and AS4 contour patterns show a distinctive intensity decrease in the scattering pattern near the beamstop.

Perret and Ruland (58) have performed a similar experiment with glycerin soaked PAN-based graphite fibers. They observed a decrease in the intensity perpendicular to the fiber axis when the intensity versus scattering angle was plotted on a log-log scale.

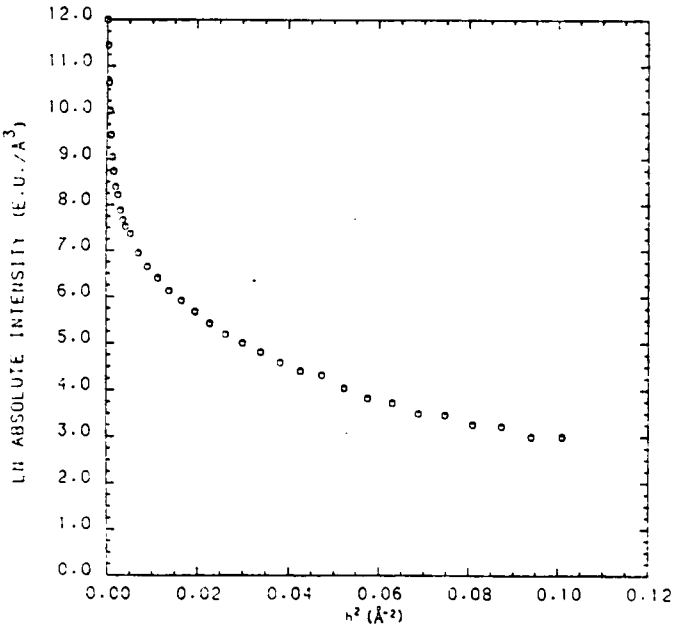

(a)

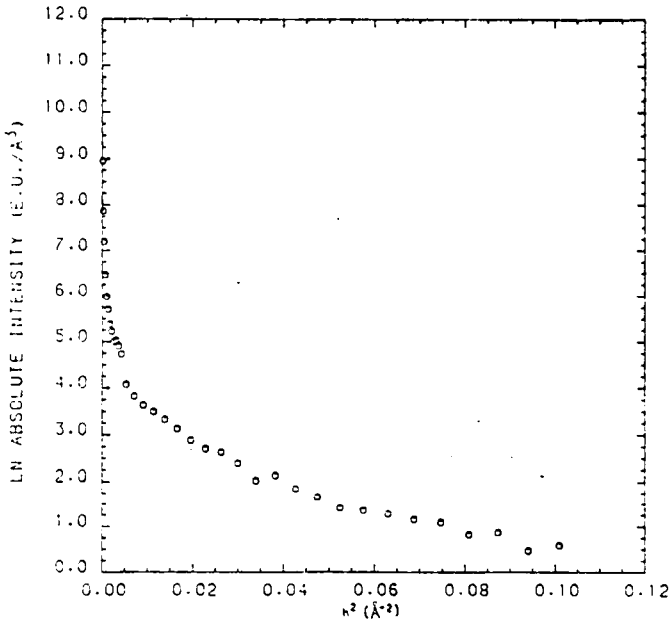

(b)

Figure 6-36. Guinier Plots of the Combined Scattering Data for VSB-16. (a) Equatorial Slice; (b) Meridional Slice.

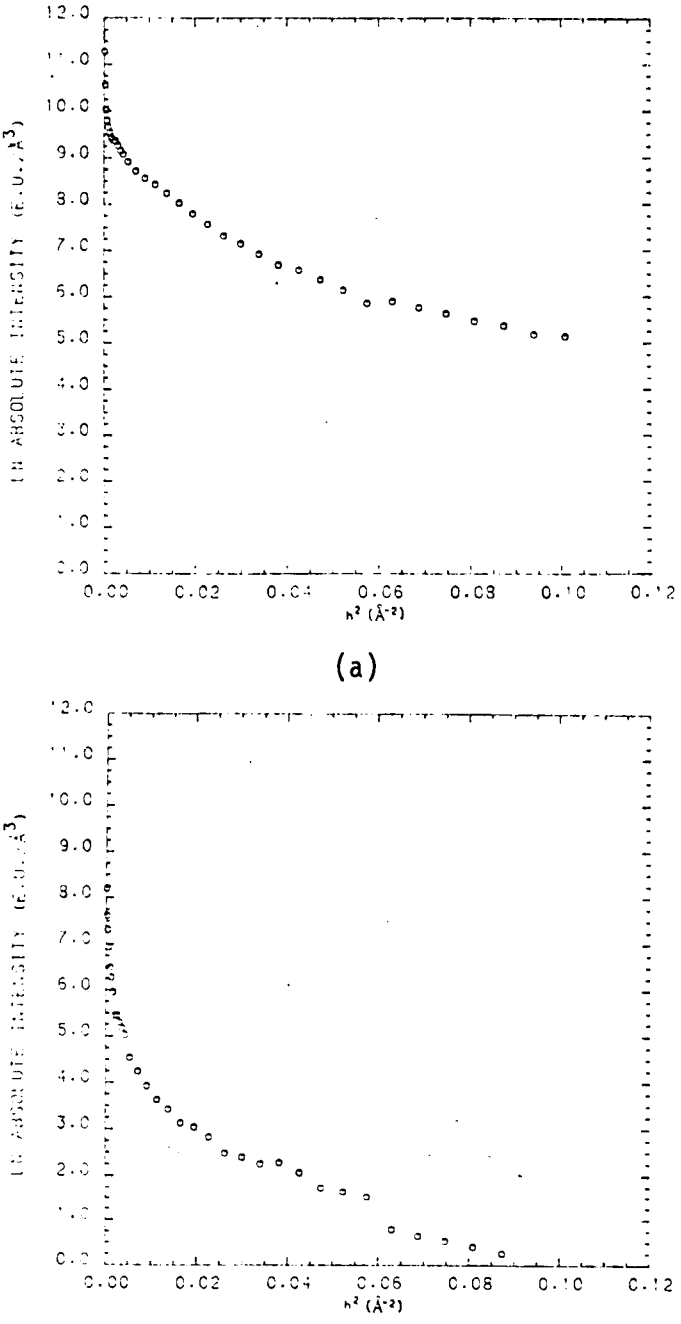

Figure 6-37. Guinier Plots of the Combined Scattering Data for HMS. (a) Equatorial Slice; (b) Meridional Slice.

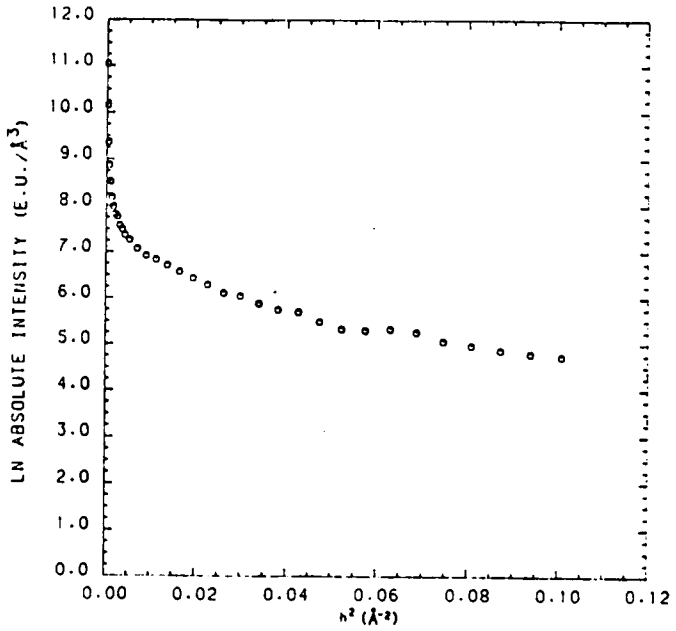

(a)

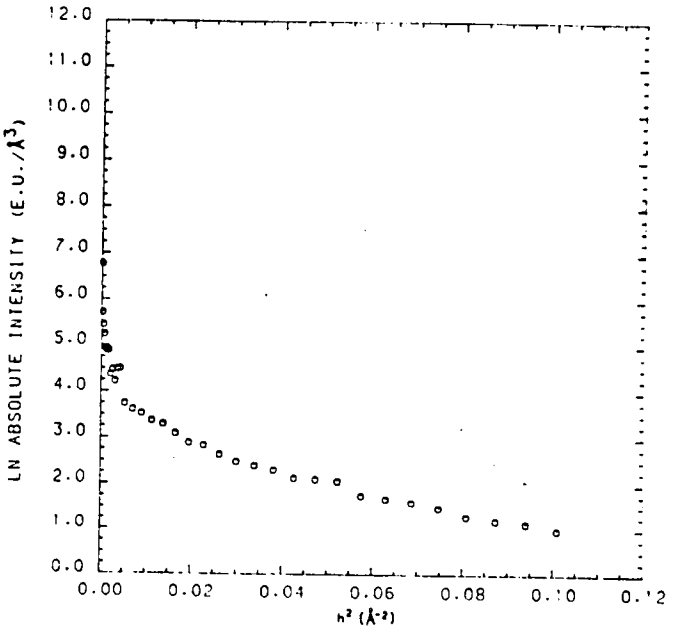

(b)

Figure 6-38. Guinier Plots of the Combined Scattering Data for AS4. (a) Equatorial Slice; (b) Meridional Slice.

Table 6-4. Void Size Distribution in Graphite Fibers

Fiber Type	Width (nm)	Volume (%)	Length (nm)	Volume (%)
	9.5	1.9	9.3	1.5
VSB-16	24.0	17.7	31.4	22.8
	46.0	80.4	55.2	75.7
	6.8	10.5	6.2	7.5
HMS	38.0	89.5	17.0	41.4
			33.0	51.1
	6.3	2.2	2.2	3.4
AS4	22.0	16.4	11.3	5.2
	42.0	81.4	30.0	91.4

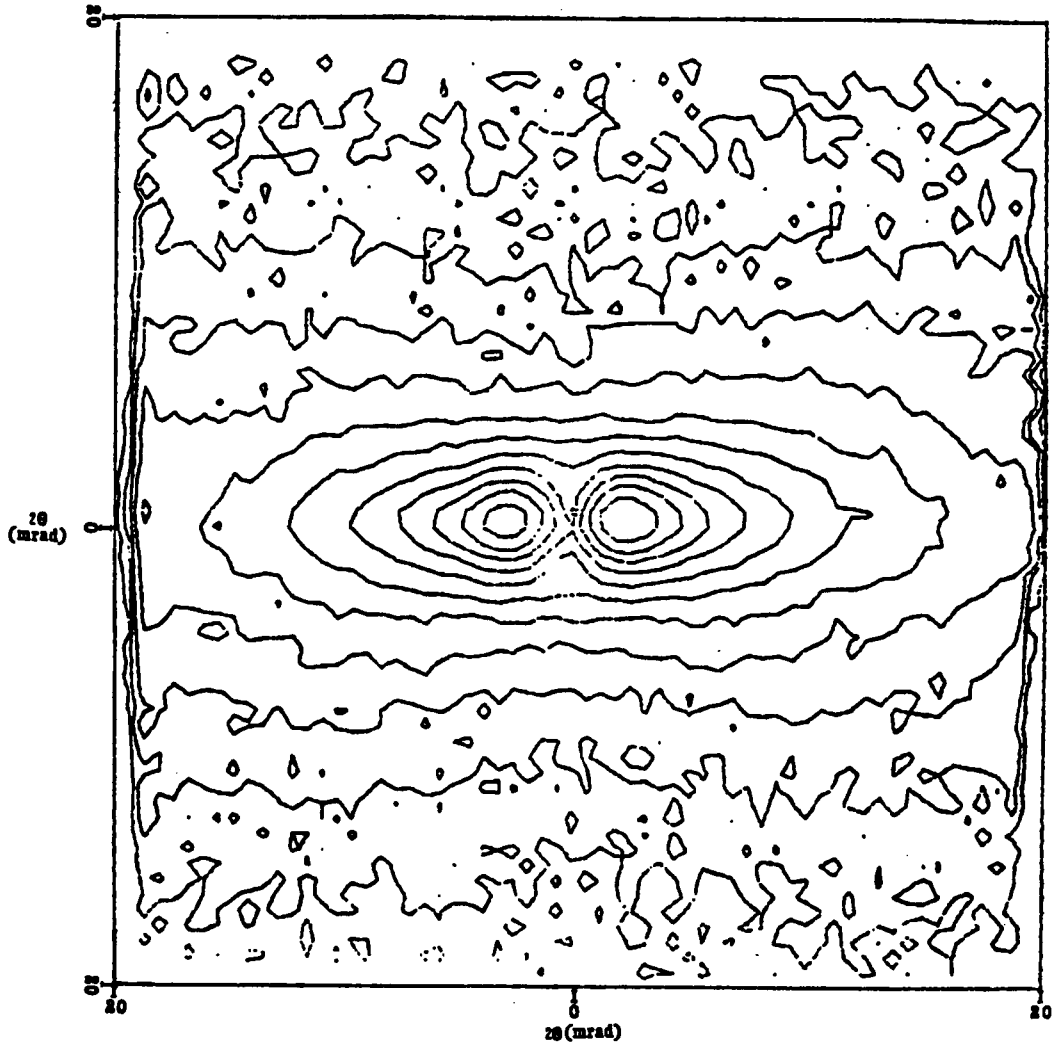

Figure 6-39. SAXS Contour Plot of VSB-16 Soaked in Glycerin from the Long Geometry.

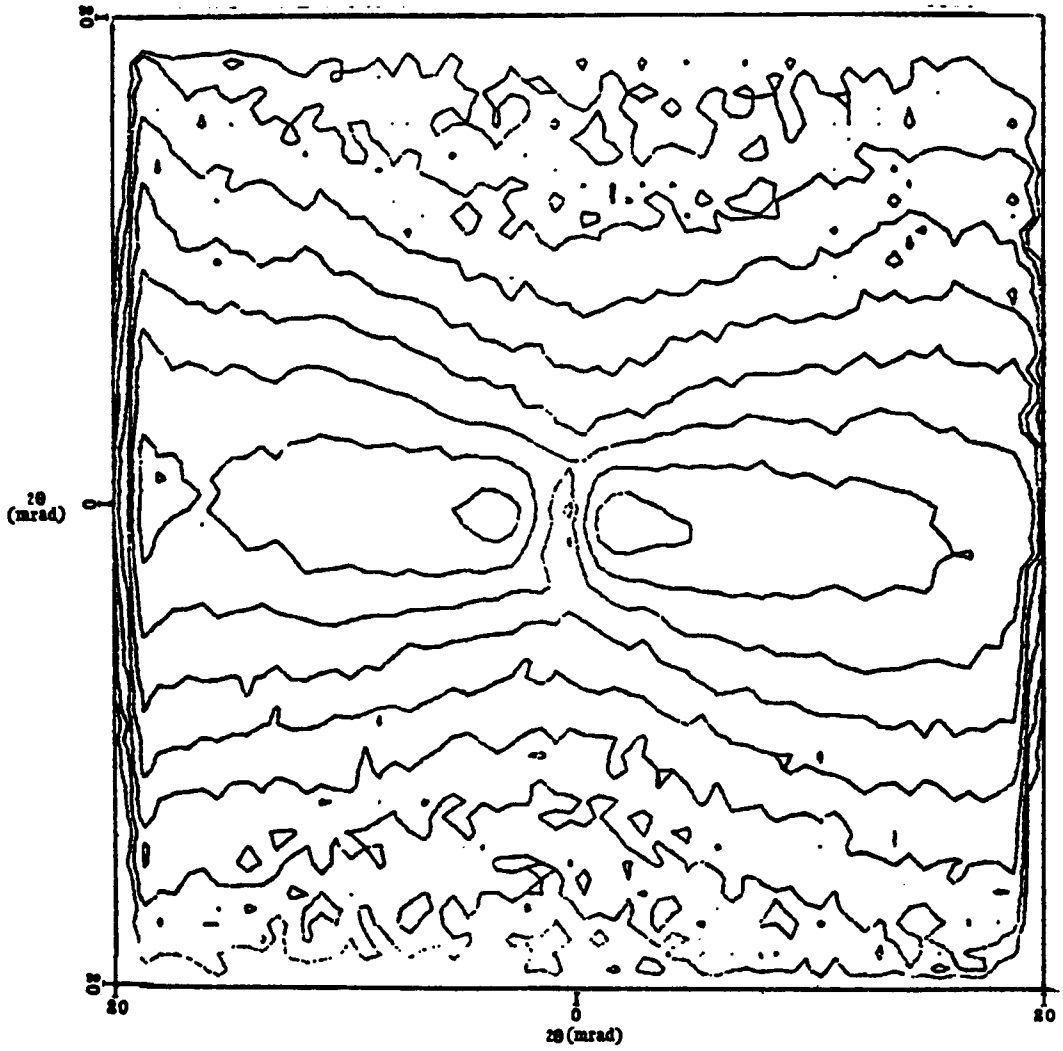

Figure 6-40. SAXS Contour Plot of HMS Soaked in Glycerin from the Long Geometry.

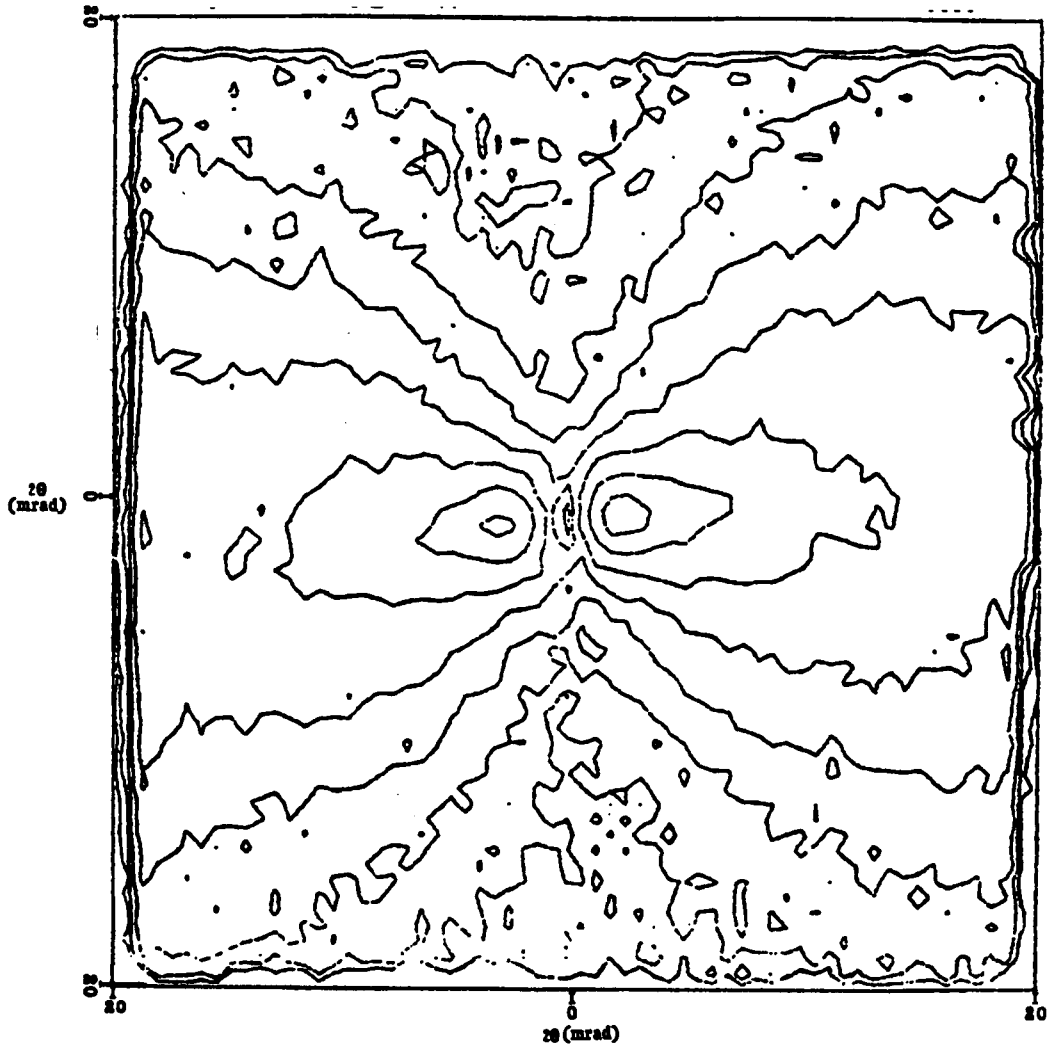

Figure 6-41. SAXS Contour Plot of AS4 Soaked in Glycerin from the Long Geometry.

They attributed the decrease in intensity to the glycerin eliminating multiple scattering from the filament contours.

To determine if their interpretation is correct and if it is applicable to pitch-based graphite fibers as well, the plots of the absolute intensity versus scattering angle were made for the dry and glycerin soaked graphite fibers. The log-log plots are presented in Figure 6-42 through 6-44. The plot for the pitch-based VSB-16 fibers showed that the glycerin did not reduce the intensity in the equatorial or meridional direction. The plots for the PAN-based HMS and AS4 showed a decrease in intensity in the equatorial direction, but not in the meridional direction. The decrease in intensity was smaller than the decrease calculated in the case where the voids were filled by the glycerin. The SEM micrographs of the three types of graphite fibers are shown in Figure 6-45 through 6-47. The fiber surface of the pitch-based VSB-16 is clearly rougher than the surface of either of the PAN-based fibers. This leads to the conclusion that the glycerin reduced the electron density difference between the fibers and the environment and as a result the intensity was reduced in the equatorial direction due to the elimination of x-ray reflected from the fiber surface of the PAN-based graphite fibers.

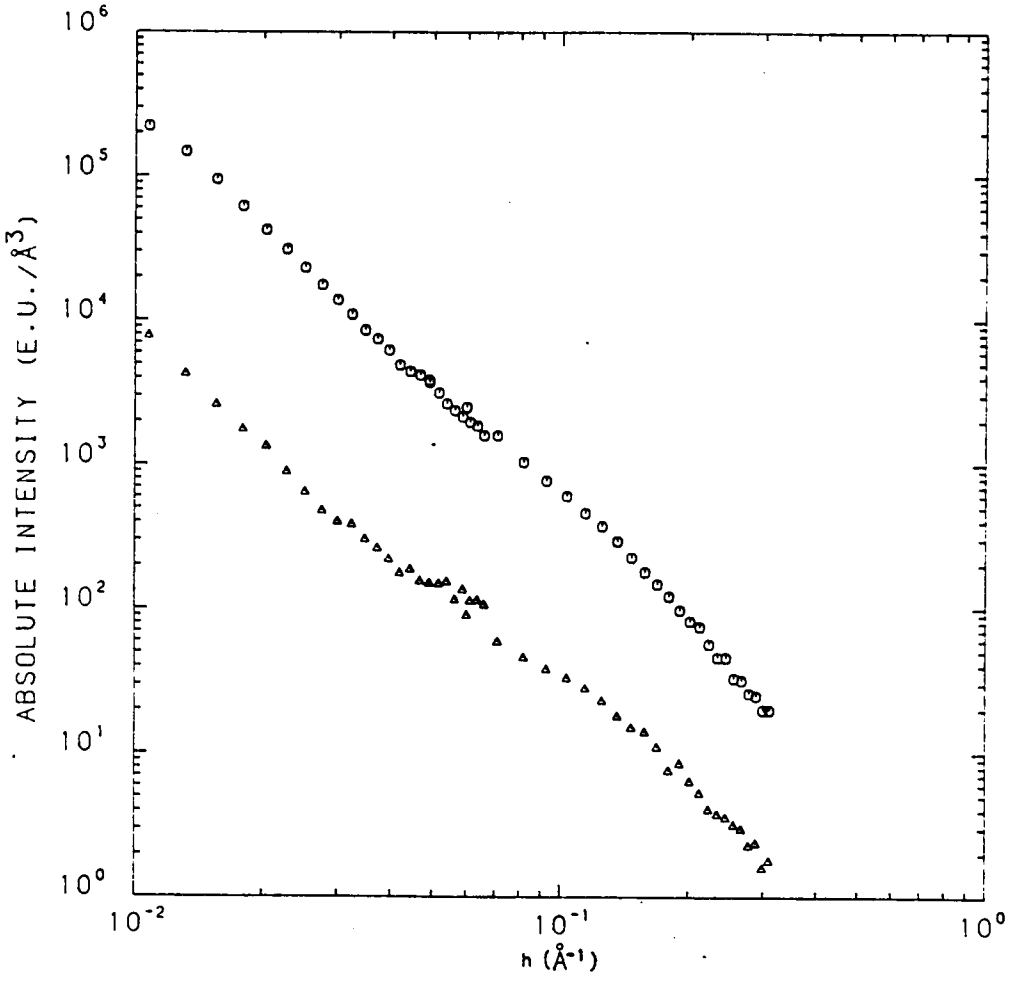

Figure 6-42. Absolute Scattering Intensity Variation with Scattering Angle for VSB-16. o Equatorial Slice; Δ Meridional Slice.

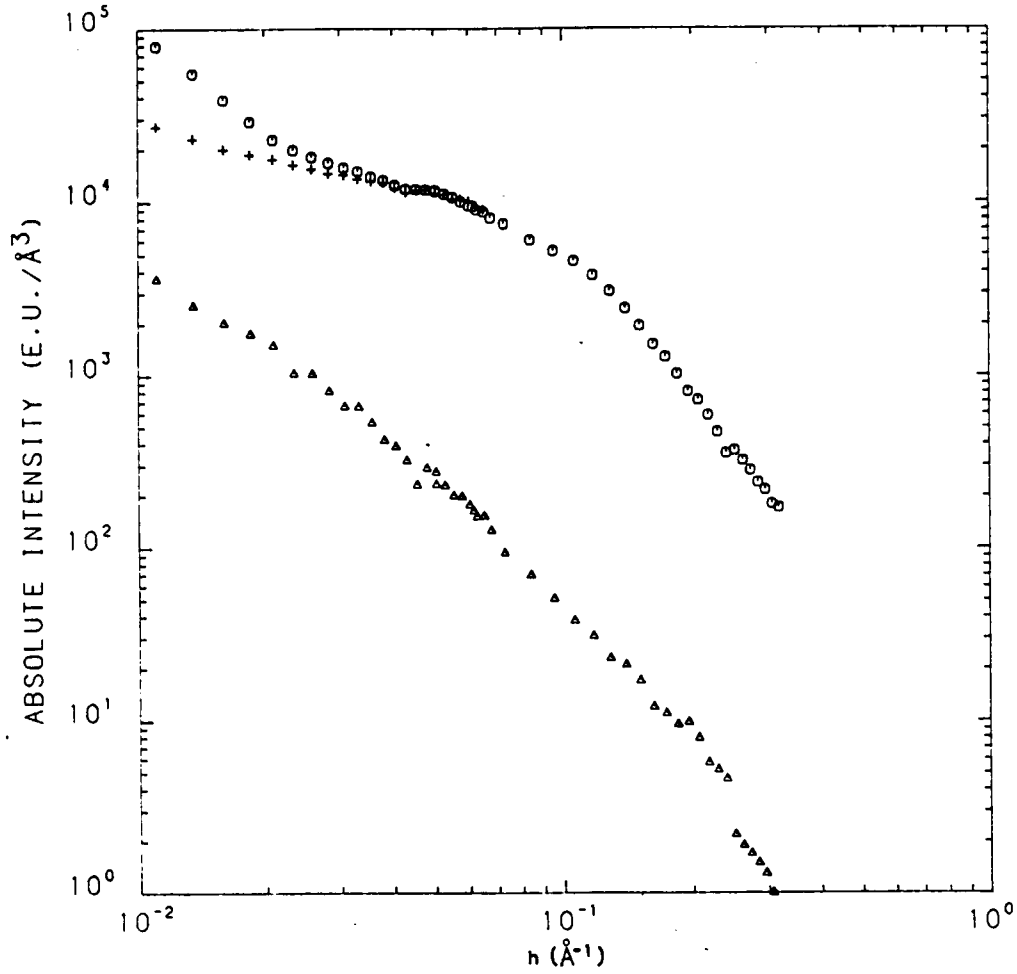

Figure 6-43. Absolute Scattering Intensity Variation with Scattering Angle for HMS. o Equatorial Slice; Δ Meridional Slice; + Glycerin Soaked Equatorial Slice.

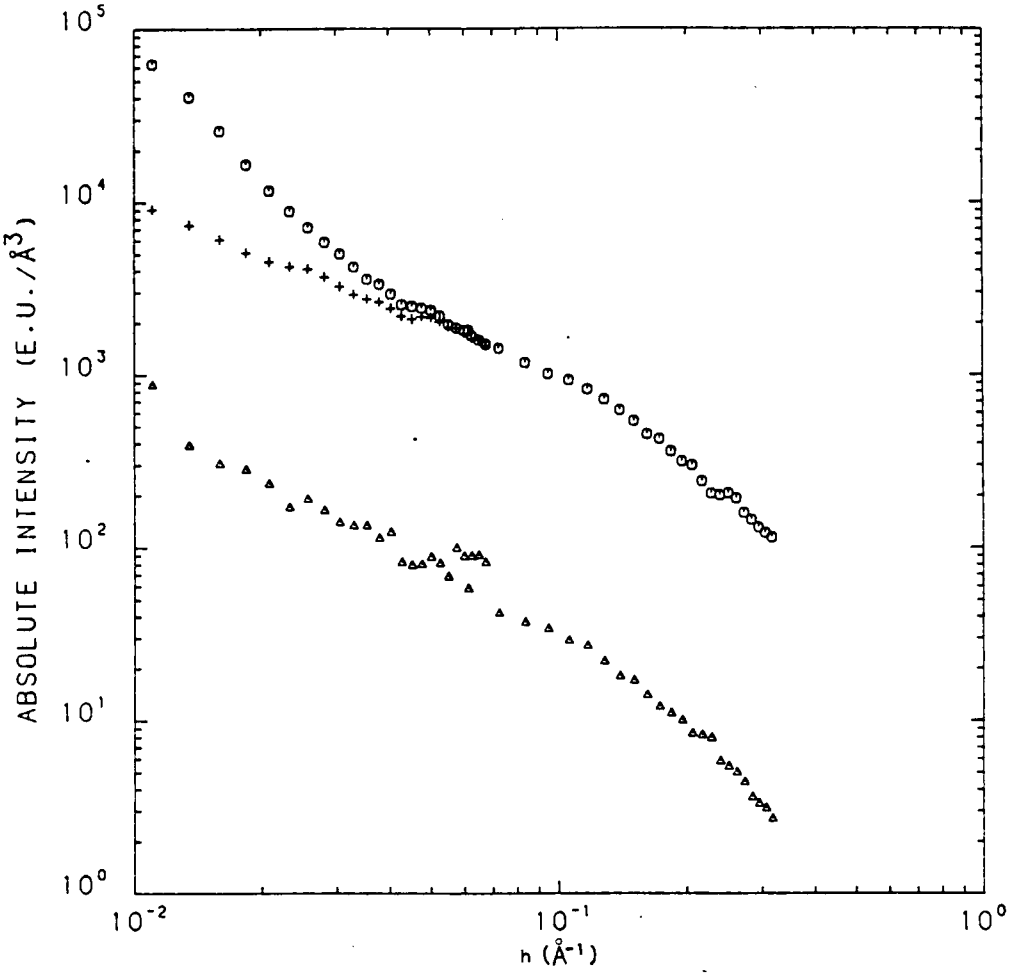

Figure 6-44. Absolute Scattering Intensity Variation with Scattering Angle for AS4. o Equatorial Slice; Δ Meridional Slice; + Glycerin Soaked Equatorial Slice.

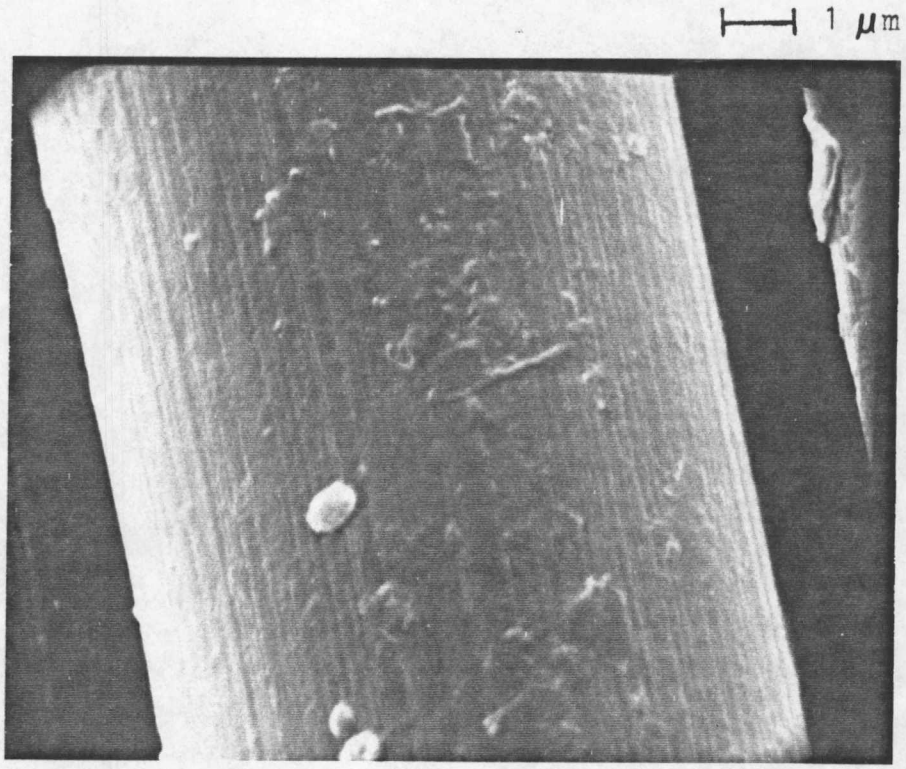

Figure 6-45. SEM Micrograph of the Fiber Surface of VSB-16.

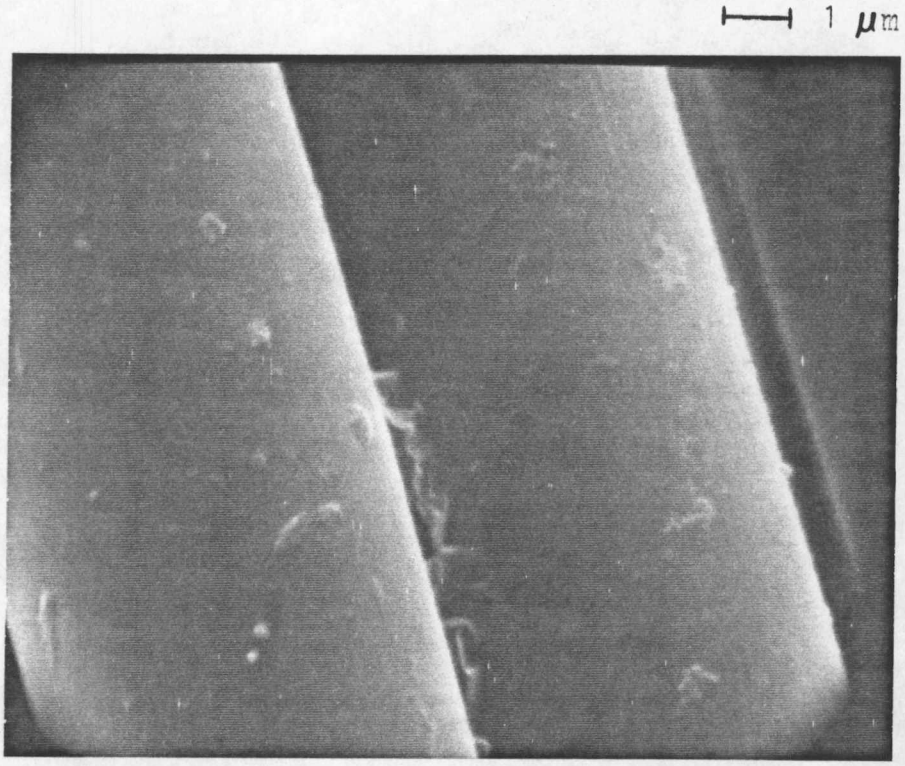

Figure 6-46. SEM Micrograph of the Fiber Surface of HMS.

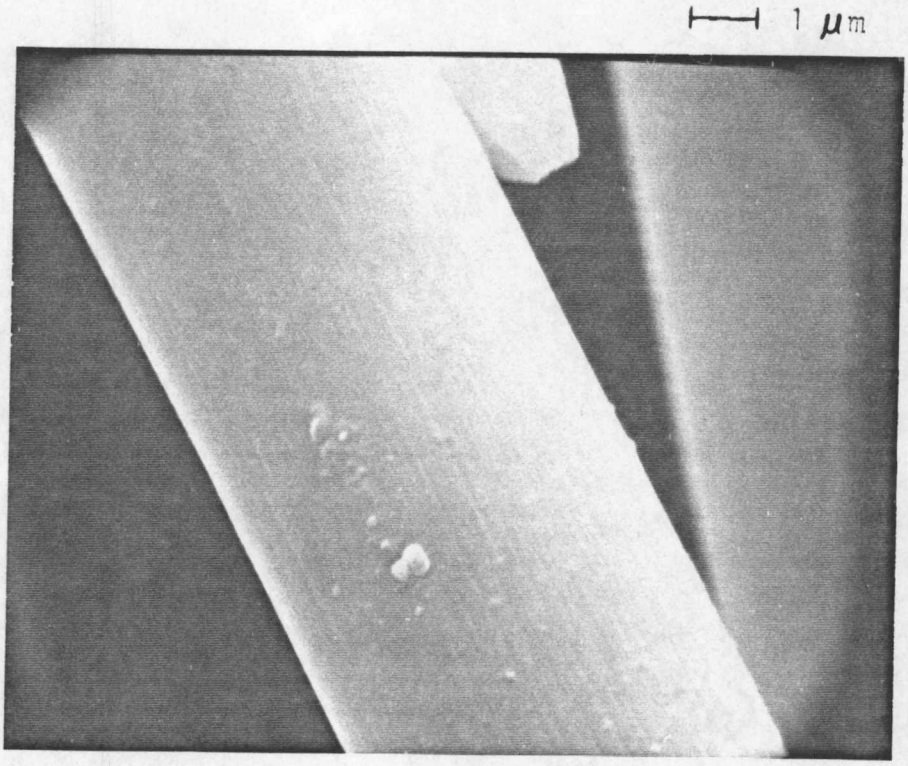

Figure 6-47. SEM Micrograph of the Fiber Surface of AS4.

CHAPTER 7

CONCLUSIONS

Kevlar® 49 fibers contain a system of microvoids with a preferred orientation of the long axis parallel to the fiber axis. There is a distribution of void sizes detected by SAXS. The largest voids in the Kevlar® 49 fiber are capable of being filled with a diffusing liquid. Plasma etching revealed that the skin has a periodic banding associated with a radial system of pleated sheets. The thickness of the skin was determined to be on the order of 1 to 2 μm. The largest voids were determined to be located in the skin and connected to the fiber surface. The smaller voids are isolated in the fiber core and the volume fraction of voids is larger in the core.

SAXS contour plots of fractured epoxy resins cured with Jeffamine T-403 showed that voids were created in the material during the application of stress. Kevlar® 49 fibers reinforced composites has a contour plot that resulted from a combination of voids in the epoxy as well as voids created in the fiber. The Kevlar® 49 fibers showed good adhesion to the epoxy resin. The composites were able to withstand high strains due to the good adhesion of the Kevlar® 49 fibers in the ductile epoxy matrix.

The graphite fibers contained voids that were oriented in relation to the (002) graphite planes. The graphite fibers had a closed pore system with a distribution of void sizes. Glycerin was

able to reduce the equatorial intensity in the PAN-based fibers. This scattering was determined to be possibly due to reflection from the fiber surface.

REFERENCES

REFERENCES

1. A. H. Compton, Phys. Rev. 21 715 (1923); 22, 409 (1923).
2. A. Guinier and G. Fournet, Small-Angle Scattering of X-rays, Wiley, New York (1955).
3. O. Glatter and O. Kratky (Editors), Small Angle X-ray Scattering, Academic Press, New York (1982).
4. W. L. Bragg, Proc. Cambridge Phil. Soc., 17, 43 (1913).
5. L. E. Alexander, X-ray Diffraction Methods in Polymer Science, Wiley, New York (1969).
6. M. Kakudo and N. Kasai, X-ray Diffraction by Polymers, American Elsevier, New York (1972).
7. H. Brumberger, Small Angle X-ray Scattering, Academic Press, New York (1967).
8. A. Guinier, Compt. Rend., 204, 1115 (1937).
9. A. Guinier, Ann. Phys. (Paris), 12, 161 (1939).
10. A. Guinier, J. Chim. physique, 40, 133 (1943).
11. G. Porod, Forschr. Hochpolym. Forsch., 2, 363 (1961).
12. P. Debye, Am. Physik, 46, 809 (1915).
13. P. Debye and A. Bueche, J. Appl. Phys., 20, 518 (1949).
14. P. Debye, H. Anderson, and H. Brumberger, J. Appl. Phys., 28, 679 (1957).
15. G. Porod, Kolloid-Z., 124, 83 (1951).
16. G. Porod, Kolloid-Z., 125, 51 (1952).
17. L. Kahovec, G. Porod, and H. Ruck, Kolloid-Z., 133, 16 (1953).
18. P. Schlack, German Patent 676,117 (1939).
19. P. Castan, British Patent 518,057 (1938).
20. P. Castan, British Patent 579,698 (1943).

21. S. O. Greenlee, U.S. Patent 2,503,726 (1943).

22. W. G. Potter, Epoxide Resins, Iliffe Books, London (1970).

23. I. Skeist, Epoxy Resins, Reinhold, New York (1958).

24. H. Lee and K. Neville, Epoxy Resins, McGraw-Hill, New York (1957).

25. F. Kong, D. M. Hoffman, and R. J. Morgan, Lawrence Livermore Laboratory Preprint UCRL-86778 (1981).

26. P. J. Flory, Principles of Polymer Chemistry, Cornell U.P., Ithaca, N.Y. (1953).

27. E. H. Erath and R. A. Spur, J. Polym. Sci., 35, 391 (1959).

28. E. H. Erath and M. Robinson, J. Polym. Sci., C, Polym. Symp. No. 3 (1963).

29. J. L. Racich and J. A. Koutsky, J. Appl. Polym. Sci., 20, 2111 (1976).

30. J. S. Mijovic and J. A. Koutsky, J. Appl. Polym. Sci., 23, 1037 (1979).

31. R. J. Morgan and J. E. O'Neal, J. Mater. Sci., 12, 1966 (1977).

32. R. J. Morgan and J. E. O'Neal, Polym. Plast. Technol. Eng., 10, 49 (1978).

33. R. J. Morgan, J. E. O'Neal, and D. B. Miller, J. Mater. Sci., 14, 109 (1979).

34. R. J. Matyi, D. R. Uhlmann, and J. A. Koutsky, J. Polym. Sci., Polym. Phys. Ed., 18, 1053 (1980).

35. L. Penn, H. A. Newey, and T. T. Chiao, J. Mater. Sci., 11, 190 (1976).

36. H. Blades, U.S. Patent 3,767,756 (1973).

37. M. G. Northold, Eur. Polym. J., 10, 799 (1974).

38. M. Panar, P. Avakian, R. C. Blume, K. H. Gardner, T. O. Gierke, and H. H. Yang, J. Polym. Sci.: Polym. Phys. Ed., 21, 1955 (1983).

39. M. G. Dobb, A. M. Hindeleh, D. J. Johnson, and B. P. Saville, Nature, 253, 189 (1975).

40. J. W. Ballou, Polymer Preprints 17 (1), 75 (1976).

41. M. G. Dobb, D. J. Johnson, A. Majeed, and B. P. Saville, Polymer, 20, 1284 (1979).

42. M. G. Dobb, D. J. Johnson, and B. P. Saville, J. Polym. Sci.: Polym. Phys. Ed., 15, 2201 (1977).

43. M. G. Dobb, D. J. Johnson, and B. P. Saville, J. Polym. Sci.: Polym. Symp., 58, 237 (1977).

44. R. J. Morgan, C. O. Pruneda, and W. J. Steele, J. Polym. Sci.: Polym. Phys. Ed., 21, 1757 (1983).

45. H. K. Herglotz, J., Colloid Interface Sci., 75, 105 (1980).

46. M. G. Dobb, D. J. Johnson, A. Majeed, and B. P. Saville, Polymer, 20, 1284 (1979).

47. R. E. Franklin, Proc. Roy. Soc. (London), 209A, 196 (1951).

48. C. L. Mantell, Carbon and Graphite Handbook, Interscience, New York (1968).

49. J. Delmonte, Technology of Carbon and Graphite Fiber Composites, Reinhold, New York (1981).

50. J. D. Bernel, Proc. Roy. Soc. (London), 106A, 749 (1924).

51. A. Shindo, Osaka Koygo Gijutsu Shikensho Hohoku, 317, 52 (1961).

52. H. M. Ezekiel, Carbon, 6, 237 (1968).

53. R. Perret and W. Ruland, J. Appl. Cryst., 1, 257 (1968).

54. P. Kwizera, M. S. Dresselhaus, D. R. Uhlmann, J. S. Perkins, and C. R. Desper, Carbon, 20, 387 (1982).

55. L. T. Drzal, J. A. Mescher, and D. L. Hall, Carbon, 17, 375 (1979).

56. W. Johnson and W. Watt, Nature (London), 215, 384 (1967).

57. D. V. Badami, J. C. Joiner, and G. A. Jones, 5th Int. Conf. Carbon Graphite, London (1978).

58. R. Perret and W. Ruland, J. Appl. Cryst. 2, 209 (1969).

59. L. Singer, U.S. Patent 4,005,183 (1977).

60. I. Tomizuka, T. Kurita, Y. Tanaka, and O. Watanabe, Yogyo Kyokai-Shi, 79, 217 (1971).

61. D. J. Johnson, I. Tomizuka, and O. Watanabe, Carbon, 13, 529 (1975).

62. I. L. Kalnin, Fracture of Composite Materials, G. C. Sih and V. P. Tamuza, Editors, Sijthoff & Noordhoff, Alphen aan den Rijn, The Netherlands (1979).

63. M. R. Piggott, Load Bearing Fibre Composites Pergamon Press, New York (1980).

64. B. W. Rosen, Mechanics of Composite Materials, Z. Hashin and C. T. Herakovich, Editors, Pergamon Press, New York (1983).

65. S. L. Phoenix and E. M. Wu, Mechanics of Composite Materials, Z. Hashin and C. T. Herakovich, Editors, Pergamon Press, New York (1983).

66. E. P. Plueddeman, Editor, Composite Materials Vol. 6 Interfaces in Polymer Matrix, Academic Press, New York (1974).

67. W. A. Zisman, Adhesion and Cohesion, Elsevier Press, New York (1962).

68. R. M. Jones, Mechanics of Composite Materials, McGraw-Hill, New York (1975).

69. C. C. Chamis and G. P. Sendeckyj, J. Comp. Mat., 2, 332 (1968).

70. B. W. Rosen, Composites, 4, 16 (1973).

71. J. Dimmock and M. Abrahams, Composites, 1, 87 (1969).

72. A. G. H. Dietz, Fiber Glass Reinforced Plastics, R. H. Sonneborn, Editor, Reinhold, New York (1954).

73. G. A. Cooper, Rev. Phys. in Tech., 2, 49 (1971).

74. A. Kelly, Proc. Roy. Soc., A282, 63 (1964).

75. A. Keely and W. R. Tyson, J. Mech. Phys. Solids, 13, 329 (1965).

76. G. A. Cooper and J. M. Sillwood, J. Mat. Science, 7, 235 (1969).

77. J. Aveston and A. Kelly, J. Mat. Science, 8, 352 (1973).

78. V. K. Tewary, Mechanics of Fibre Composites, John Wiley, New York (1978).

79. R. P. Sheldon, Composite Polymeric Materials, Applied Science, New York (1982).

80. Z. Hashin and C. T. Herakovich, Editors, Mechanics of Composite Materials, Pergamon Press, New York (1983).

81. B. Chapman, Glow Discharge Processes, John Wiley and Sons, New York (1980).

82. J. S. Lee, Masters Thesis in Polymer Engineering, The University of Tennessee, Knoxville (1984).

83. M. H. Jellinek, E. Solomon, and I. Fankuchen, Ind. Eng., Anal. Ed., 18, 172 (1946).

VITA

Gregory G. Rice was born on April 23, 1956, in Florence, Alabama. He graduated from the University of Alabama in August 1978 with the Bachelor of Science degree, majoring in chemistry and minoring in biology. Upon graduation, he was employed as a polymer chemist with Reichhold Chemicals, Inc. in Jacksonville, Florida. In 1980, he was employed as a project engineer with Clow Corporation in Pell City, Alabama. He entered The University of Tennessee, Knoxville in 1982 to obtain the Masters Degree in polymer engineering.